5-1996

A Study of the Gradient Drift Instability in the High-Latitude Ionosphere Using the Utah State University Time Dependent Ionospheric Model

Mahesh Subramanium

A STUDY OF THE GRADIENT DRIFT INSTABILITY IN THE HIGH-LATITUDE IONSOPHERE USING THE UTAH STATE UNIVERSITY TIME DEPENDENT IONOSPHERIC MODEL

by

Mahesh Subramanium

A thesis submitted in partial fulfillment
of the requirements for the degree

of

MASTER OF SCIENCE

in

Physics

Approved:

UTAH STATE UNIVERSITY
Logan, Utah

1996

ABSTRACT

A Study of the Gradient Drift Instability in the High-Latitude Ionosphere Using the Utah State University Time Dependent Ionospheric Model

by

Mahesh Subramanium, Master of Science

Utah State University, 1996

Major Professor: Dr. Jan J. Sojka
Department: Physics

Research over the years has established that the Gradient Drift Instability process causes small-scale irregularities, mostly along the edges of the high-latitude polar cap patches. Studying these irregularities will help in the development of a Global Scale Ionospheric model, which is a central part of a global space weather forecast system. Much theoretical work has been done with varying degrees of complexity to study this instability in the high latitude patches.

In this work we have used the Utah State University Time Dependent Ionospheric Model to model the high-latitude patches, calculate the growth rate of the instability, and perform a macro-scale study of the phenomenon. This is the first time that real ionospheric values have been used to calculate the growth rate and to provide two-dimensional maps identifying Gradient Drift Instability-caused irregularity regions in the

polar cap. Our research shows that regions of intense instability occur along the edges of the tongue of ionization and its throat regions with strong growth rates along the borders of the cusp region.

(118 pages)

ACKNOWLEDGMENTS

My sincere thanks to Dr. Jan J. Sojka for his excellent guidance, teaching, and patience. Thanks to Dr. Lie Zhu and Dr. Abdullah Barakat for a number of helpful discussions.

Thanks to Don Thompson for letting me use his plotting routines, and to Mike Bowline for providing the data sets.

And finally, thanks to Dr. Jim Wheeler for his teaching and help in my journey through the wonderful world of physics. Physics was more fun looking through his eyes.

Mahesh Subramanium

CONTENTS

Page

ABSTRACT....ii

ACKNOWLEDGMENTS....iv

CONTENTS....v

LIST OF TABLES....vii

LIST OF FIGURES....viii

SYMBOLS AND CONSTANTS....xii

CHAPTER

1. INTRODUCTION....1

2. BACKGROUND....4

2.1. Plasma Instabilities and their Classification....4
2.2. Instabilities in the Upper Atmosphere and the Ionosphere....7

2.2.1. The Upper Atmosphere and the Ionosphere....7
2.2.2. High-Latitude F Region Irregularities and Instabilities....8

2.3. High-Latitude F Region Plasma Structures....9

2.3.1. Polar Cap Patches....10
2.3.2. Boundary (and Subauroral) Blobs....18
2.3.3. Sun-Aligned Arcs, Auroral Blobs, and Localized Depletions....20

3. GRADIENT DRIFT INSTABILITY....22

3.1. Signatures of the Gradient Drift Instability in the Polar Cap Patches....22
3.2. Physics of the Gradient Drift Instability....25

3.2.1. Case 1a....25
3.2.2. Case 1b....27
3.2.3. Case 2a....27
3.2.4. Case 2b....29

3.3. Theoretical Framework of the Gradient Drift Instability.....31

3.3.1. The Fluid Equations.....33
3.3.2. Electromagnetic Equations.....34
3.3.3. Procedure for Deriving the Growth Rate.....35

4. IONOSPHERIC DATA SET, GRADIENT DRIFT INSTABILITY ASSUMPTIONS, AND GROWTH EXPRESSIONS.....38

4.1. Time Dependent Ionospheric Model.....38
4.2. The Data Set.....38
4.3. Growth Rates.....41

4.3.1. Basic Assumptions.....47
4.3.2. Some Growth Rate Expressions and Their Assumptions.....48
4.3.3. Method Followed in Calculating the Growth Rate.....54

5. RESULTS AND DISCUSSION.....59

5.1. Results from Data Set 1.....59
5.2. Results from Data Set 2.....66

5.2.1. Case A.....70
5.2.2. Case B.....76
5.2.3. Case C.....78
5.2.4. Case D.....81
5.2.5. Case E.....81

6. SUMMARY AND CONCLUSION.....84

6.1. Summary.....84
6.2. Conclusion.....85
6.3. Suggestions for Further Research.....86

REFERENCES.....88

APPENDIX.....91

LIST OF TABLES

Table Page

1. Grid positions, scale lengths, and growth time for case A.....74
2. Grid positions, scale lengths, and growth time for case B.....77
3. Grid positions, scale lengths, and growth time for case C.....80
4. Grid positions, scale lengths, and growth time for case D.....82
5. Ion-neutral resonant collision frequencies.....98
6. Value of the constant C_{in} for various ion-neutral pairs (in multiple of 10^{10})...101
7. Electron-neutral collision frequencies.....104

LIST OF FIGURES

Figure Page

1. Sequence of contour maps of f_0F_2 values tracing the development of a polar cap patch [*Hill*, 1963].....12

2. Total electron content variations associated with polar cap patches (lower trace) [*Weber et al., 1986*].....13

3. Peak plasma densities measured in the winter polar cap (dots in the center panel) [*Buchau et al.*, 1985].....14

4. Orientation of the IMF components in the GSE coordinate system.....15

5. Magnetic field line connections between the IMF and the geomagnetic field for southward IMF ($B_z < 0$) and northward IMF ($B_z > 0$) [*Potemra*, 1983].....16

6. Series of N_mF_2 snapshots from TDIM simulation [*Sojka et al.*, 1993].....17

7. Plasma density contours measured during radar elevation scans in the magnetic meridian showing a boundary blob and an auroral blob [*Rino et al.*, 1983].....19

8. Model results of a patch distorting into a boundary blob [*Robinson et al.*, 1985].....20

9. Temporal variation of scintillation intensity index (S_4) [*Basu et al.*.....23

10. Electric field and electron density fluctuations and electron density profile measured by Aureol 3 spacecraft [*Cerisier and Berthelier.*, 1985].....24

11. Electron density fluctuations measured by Aureol 3 spacecraft [*Cerisier and Berthelier.*, 1985].....24

12. Schematic showing the development of the GDI or the $\vec{E} \times \vec{B}$ instability for the case 1a.....27

13. Schematic showing the development of the GDI or the $\bar{E} \times \bar{B}$ instability for the case 1b.....28

14. Schematic showing the development of the GDI or the $\bar{E} \times \bar{B}$ instability for the case 2a.....29

15. Schematic showing the development of the GDI or the $\bar{E} \times \bar{B}$ instability for the case 2b.....30

16. Cartoon showing the occurrence of the various instability cases in the patch.....30

17. Isodensity contour plots from model results showing the evolution of the $\bar{E} \times \bar{B}$ instability [*Keskinen and Ossakow*, 1982].....32

18. *Heppner-Maynard* 'A' convection pattern used in the TDIM simulation, *Heppner-Maynard* 'DE' convection pattern [*Sojka et al.*, 1993].....39

19. The rectangular box shows the patch simulation regions -- the region of interest.....41

20. Gray scale plot of the electron density generated by the TDIM model at different altitudes.....42

21. *Heppner-Maynard* convection pattern superimposed on the electron density gradient pattern.....43

22. The altitude profile of (a) the density of the electrons and (b)-(d) the various ions generated by the TDIM.....44

23. The altitude profile of the density of (a) the electrons and (b)-(d) the various neutrals generated by the TDIM.....45

24. The altitude profile of (a) the density of the electrons and the temperature profiles of the (b) electrons, (c) ions, and (d) neutrals generated by the TDIM.....46

25. Ratio of the electron collision frequency to gyro frequency at different altitude slices.....50

26. Altitude profiles of the ratios; (a) electron collision to gyro frequency, ion collision to gyro frequency, (c) ion-neutral to ion-electron

collision frequency and, (d) electron-ion to electron-neutral collision frequency....51

27. Geometry used in developing growth rate equation (12)....53

28. Grid system showing the three density points....56

29. Density gradient vectors superimposed on the electron density pattern for data set 1....60

30. Convection (wider arrow heads) and density gradient vectors for data set 1....62

31. Gray-scale plot of the density gradient scale length in kilometers for various cutoffs....63

32. Growth time in seconds for the scale lengths of Figure 31....65

33. B_y variations used by the USU TDIM model to generate data set 2....67

34. *Heppner-Maynard* "A" convection pattern....68

35. *Heppner-Maynard* "DE" convection pattern....69

36. *Heppner-Maynard* "BC" convection pattern....70

37. Electron density snapshots for (a) 2115 UT, (b) 2120 UT, (c) 2125 UT, and (d) 2130 UT....71

38. Electron density snapshots for (a) 2135 UT, (b) 2140 UT, (c) 2145 UT, and (d) 2130 UT....72

39. Electron density snapshots for (a) 2155 UT and (b) 2200 UT....73

40. (a) Log plot of the growth time and (b) convection of the flux tube discussed in case A....74

41. (a) Log plot of the growth time and (b) convection of the flux tube discussed in case B....77

42. (a) Log plot of the growth time and (b) convection of the flux tube discussed in case B2....79

43. (a) Log plot of the growth time and (b) convection of the flux tube discussed in case C.....80

44. (a) Log plot of the growth time and (b) convection of the flux tube discussed in case D.....82

45. Convection of the flux tube discussed in case E.....83

46. Altitude profile of the gyro radius of charged particles.....94

47. Altitude profile of the gyro frequency of charged particles.....95

48. Altitude profile of (a) the average electron-ion collision frequency and (b)-(d) electron with the individual ions.....99

49. Altitude profile of (a) the average ion-electron collision frequency and (b)-(d) individual ions with the electron.....100

50. Altitude profile of (a) the average ion-neutral collision frequency and (b)-(d) individual ions with all the neutrals.....102

51. Altitude profile of (a) the average electron-neutral collision frequency and (b)-(d) electrons with the individual neutrals.....103

52. Altitude profiles of the ratios: (a) electron collision to gyro frequency, ion collision to gyro frequency, (c) ion-neutral to ion-electron collision frequency, and (d) electron-ion to electron-neutral collision frequency.....105

SYMBOLS AND CONSTANTS

Symbol	*Interpretation*
α, β	Used as a subscript refer to the species i.e., ions, electrons or neutrals.
i, e, n	Used as subscripts refer to ions, electrons and neutrals respectively.
$\perp$	Used as a subscript indicates that the parameter is the component perpendicular to the magnetic field.
$\parallel$	Used as a subscript indicates that the parameter is the component parallel to the magnetic field.
x_0	The equilibrium or the initial unperturbed value of some parameter x.
c	Speed of light (2.9979×10^{10} cm / s).
e	Electric charge (4.8032×10^{-10} statcoulomb).
K	Boltzman constant (1.3807×10^{-16} erg / K).
$\bar{g}$	Acceleration due to gravity (980.7 cm / s^2).
A_α	Mass number of the species α.
γ_α	Ratio of specific heat capacities of the species α.
c_s	Speed of sound.
m_α	Mass of the species α.
t	Time.
p_α	Pressure of the species α.
n_α	Number density of the species α.

T_α	Temperature of the species α.
$\bar{u}_\alpha$	Velocity of the species α.
$\bar{E}$	Electric field.
$\bar{B}$	Magnetic field.
$\bar{j}$	Current density.
$\bar{k}$	Wave vector.
Ω_α	Gyro frequency of the species α.
$\upsilon_{\alpha\beta}$	Collision frequency of species α with respect to species β.
υ_α	Average collision frequency of the species α.
r_α	Gyro radius of the species α.
D	Diffusion coefficient.
γ	Growth rate.

CHAPTER 1

INTRODUCTION

A number of observations over the years have established that the high-latitude ionosphere extending from the auroral zone to the polar cap is rich in plasma density fluctuations or irregularities with scale sizes ranging from a few meters to hundreds of kilometers. These polar cap features affect communication systems in the polar regions, and understanding their source, evolution, and other related processes will enable us to explain such effects. Among the large-scale structures, polar cap patches are the largest scale structures, five times denser than the background plasma. Many smaller structures occur along the edges and throughout the patches. Experiments have shown that high-density gradients along the edges of the patches are preferred regions for the occurrence of an important class of small-scale irregularity, which disrupts trans-ionospheric radio communications. It has been found that the Gradient Drift Instability (GDI) is the cause of the structuring at the edges of the patches. Investigating the GDI and its growth rate is the purpose of this thesis.

Much theoretical work has been done on the GDI and many researchers have developed different growth rate expressions applicable to different physical domains and with various degrees of complexity. These expressions have been analyzed with approximate numbers to give an estimate of the growth rates. Some modeling studies have also been done. However, the real ionospheric values have not been used to analyze the expressions. The Utah State University Time Dependent Ionospheric Model (USU TDIM) has been successfully used to model the tongue of ionization (TOI), which leads

to patches. What I have done is use the parameters output by the TDIM, in simulating a TOI, in the different growth rate expressions and hence have obtained a real estimate of the scale sizes of the density gradients and the growth rates over the polar ionosphere, for its different stages as it progresses in time. This has not been done before. My research will contribute in optimizing and furthering the role of ionospheric models in elucidating the patch phenomenon and the irregularities along its edges. Also it will provide the high-latitude research community with maps of GDI-caused irregularity regions in the polar cap.

As we venture more into space, the space environment and its effects on us are as important as weather on our daily life. "Space weather" affects communications, Global Positioning Surveys (GPS), navigational systems, over-the-horizon radar, etc. For example, the small-scale irregularities along the edges of the polar cap patches can jeopardize communications over the polar cap. Closer to home, space weather can induce charges on power grids, telecommunication cables, etc., throwing them off line. Though nothing can be done to prevent space weather, if we could have a forecasting system for space weather just like our meteorological weather, we could gain enough time to prepare for the weather and minimize the damage. The high-latitude space physics community is now working towards the development of such a space weather forecast system. An important part of a good space weather forecast system is a Global Ionosphere Model (GIM) that would be able to predict the diurnal state of the ionosphere (referred to as climatology) based on inputs from real-time monitoring of the space weather parameters.

My research will be useful to the developers of such a model for space weather forecasting.

The thesis begins with a background study in Chapter II. The plasma instabilities and their classification, the morphology, and the dynamics of the high-latitude plasma structures are discussed. Polar cap patches are treated in some detail. In Chapter III we study the physics of the GDI, its starting equations, and the methodology for deriving the growth rate of plasma instabilities. In Chapter IV we discuss the USU TDIM patch simulation data set that will be used in calculating the growth rates along with some growth rate expressions and the assumptions that were made in deriving those expressions. We also discuss the procedure followed in calculating the growth rates. In Chapter V we analyze and discuss the results obtained using the data set and the procedure presented in Chapter IV. Finally, we present a summary and conclusion together with directions for further research in Chapter VI. The Appendix presents the different ionospheric parameters that were used in calculating the growth rate, their typical expressions, and their profiles developed from the model output.

CHAPTER 2

BACKGROUND

2.1. Plasma Instabilities and their Classification

The term "plasma" refers to a collection of ionized and neutral particles. This collection is "quasi-neutral" in the sense that it has an equal number of positive and negative charges and it also exhibits "collective behavior" in the sense that its dynamics depends not only on the local distribution of charges and fields but also on that at remote regions.

The theoretical study of plasma can be divided into three domains. The first one--the most precise and idealistic--is what I call the impossible domain. We need to follow the trajectories and continuously calculate the effect of every particle's electric and magnetic fields on every other particle. With typical plasma density in the ionosphere being 10^{12} ion-electron pairs per m^3, this domain is indeed impossible, at least until our computers evolve to handle this load. The next accurate domain is the kinetic domain, where beautiful spatial and velocity distribution functions are used to follow the temporal and spatial variations of the plasma. Departures from the peaceful Maxwellian distribution are treated fairly and with due mathematical respect. The third domain is the fluid domain. Though not as accurate a treatment as the kinetic domain, about 80% [*Chen*, 1983:53] of the observed plasma phenomena can be explained in this domain. We no longer recognize the individual particles of the plasma but treat the plasma as a fluid element. We further assume that the velocity distribution is Maxwellian everywhere.

Hence the dependent variables of this fluid are now only a function of four independent variables (x, y, z, t), thankfully reducing the mathematical wizardry required for solving the problems. The starting equations used in the fluid approach are called the transport equations and are obtained by taking moments about the Boltzman equation with a suitable distribution function.

Whatever the domain, the plasma is acted upon by forces both electromagnetic and mechanical in nature. It is said to be in equilibrium when all the forces on it are balanced and a steady-state solution is possible for that equilibrium state. However, even with all the forces balancing, it may not be in Thermodynamic Equilibrium (TDE). Any statistical system in TDE will tend to occupy the lowest potential energy state, thus gaining higher stability. If a plasma is made to depart from TDE by some internal or external agent, thereby reducing its stability, free energy may be available. An instability thus ensues to bring the plasma to a lower potential energy state and hence closer to TDE. If the instability grows either spatially or temporally, then it is said to be unstable. On the other hand, if it dampens, it is said to be stable. Whether an instability grows or dampens depends on various factors like the nature of the drivers and their variations, etc. and most importantly on the state of the plasma at that moment in space and time.

Perturbation methods are usually employed to study plasma instabilities. Some particular variable may be perturbed, (i.e., its equilibrium value will be infinitesimally changed so that it may still be considered to be in a particular state but the change is big enough to affect its equilibrium) while other variables are fixed, or many variables may

be perturbed simultaneously. The resulting instability is analyzed theoretically using one of the two methods, viz., Normal Mode or Energy (Thermodynamic) method.

Normal Mode analysis uses perturbation techniques. It gives complete information about the instability including its growth rate, which is a measure of how fast the instability grows or dampens. This method requires the plasma equations to be completely solvable which may be impossible in many cases. The Energy method is adopted if the equations are totally intractable. It does not give any growth rate information. In this method the change in the potential energy of the system caused by the perturbation is used as an input to the thermodynamic equations. There is no fixed route to follow in this method. It is more of an art form and requires intuition and experience.

The selection of a particular method depends on whether the equations for the problem under consideration are manageable or not. However, by making assumptions and restricting the solution to certain domains, one can understand the underlying physics of the instability and get an estimate of its growth rate, stability domains etc. Needless to say working in the kinetic domain is much more complicated than working in the fluid domain.

Based on the specific domain of interest, plasma instabilities can be classified into two major classes.

1) Configuration Space or Macro Instabilities: Here we consider the instabilities in the fluid domain. The plasma is considered as a macroscopic entity (i.e., a fluid element) and the departures from equilibrium of its macroscopic variables are analyzed. The

Magenetohydrodynamic (MHD) equations (a hybrid of the simpler fluid equations) are used and normal mode analysis is usually successful. The Maxwellian velocity space departures are neglected.

2) Velocity Space or Micro Instabilities: Here we work in the kinetic domain and hence departures from a Maxwellian velocity distribution are considered. Their analysis is much more complicated than the Macro Instabilities. Perturbations techniques are applied on the equations of the Kinetic Theory (Vlasov's Equations) to analyze these instabilities. The Micro Instabilities offer a rich variety, many of them too complicated to solve.

Note that at any time the plasma may have both of these instabilities, and an instability can start out to be a micro instability and subsequently enter the macro domain. In essence, whether we classify an instability Macro or Micro depends on what domain or scale size we are interested.

2.2. Instabilities in the Upper Atmosphere and the Ionosphere

2.2.1. *The Upper Atmosphere and the Ionosphere*

The earth's ionosphere is the region of the earth's atmosphere from about 90 kilometers to 500 kilometers. The sun's radiation penetrates into these rarefied altitudes, ionizing the gases. The low pressure of these altitudes prevents any rapid recombination of the ionized gases, thus leaving a constant population of ions and free electrons among neutral particles--a plasma in every respect. This plasma is affected by earth's gravity, earth's magnetic field (a dipole field to a good approximation near the earth), the solar

wind, the Interplanetary Magnetic Field (IMF), the sun's radiation, recombination and disassociation chemistry, and various other processes that offer enough free energy to affect its equilibrium and lead to an instability. Hence different types of instabilities driven by various sources in all frequency domains and at all latitudes occur at all ionospheric altitudes.

Examples of the various instabilities in the ionosphere are: in the equatorial F region, the Gravitational Raleigh-Taylor instability process is one of the causes of the equatorial spread F phenomena; the Two Stream or the Farley-Buneman instability occurs in the electrojets, which flow in the ionospheric E region at both low and high latitudes; and the Gradient Drift Instability (GDI) occurs in the high-latitude F region plasma patches. GDI as it occurs on structures called patches in the high latitudes is the subject of this thesis, and hence forth we will focus on this instability.

2.2.2. *High Latitude F Region Irregularities and Instabilities*

Let us first distinguish between an irregularity and an instability. An irregularity is the physical entity that is brought into existence by a physical process called an instability. Instabilities are the means and irregularities are the end. For example, the structures on the edges of the plasma patches seen in the high latitudes are irregularities probably caused by the GDI.

Observations over the years have shown the high-latitude ionosphere extending from the auroral zone to the polar cap, to be a highly structured and irregular medium. The plasma is rich in irregularities (plasma density fluctuations) with scale sizes ranging

from hundreds of kilometers to a few meters. Several theories, for example, particle precipitation, neutral fluid dynamics, plasma transport, plasma instabilities and processes, etc., have been proposed to account for these high-latitude irregularities. Of these theories, those concerning plasma instabilities are quite useful in identifying and analyzing the physical processes that lead to these irregularities since several sources of free energy (Ex. density gradients, velocity shears, currents both parallel and perpendicular to the magnetic field) are readily available in the high latitudes to seed the instabilities.

Irregularities can be grouped into three categories based on their scale sizes. Large-scale irregularities have scale sizes above 10 kilometers, medium-scale irregularities have scale sizes between 10 kilometers and 30 meters and small-scale irregularities have scale sizes of about 10 meters (of the order of the ion gyro radius). The large scale irregularities and most of the medium scale irregularities, are caused by plasma macro instability processes while the small scale irregularities are caused by the plasma micro instability processes. As mentioned before, we will not be dealing with the velocity space or micro instabilities; henceforth the term "instability" will refer to only macro instability and the term "irregularity" will refer to either large- or medium-scale structures

2.3. High-Latitude F Region Plasma Structures

A number of experiments and observations have conclusively shown that there is a high spatial correlation between the irregularity and steep density gradients that characterize the walls of large-scale and medium-scale plasma structures in the high

latitudes. So it is only appropriate that we familiarize ourselves with some important features of the high-latitude F region large-scale plasma structures.

Four distinct large-scale plasma structures have been observed: polar cap patches, boundary blobs, sun-aligned arcs, and auroral blobs. Of these, the polar cap patches are the most relevant to this thesis. So we will study them in some detail and then briefly examine the other three structural forms.

2.3.1. *Polar Cap Patches*

These are the largest scale structures associated with kilometer-scale irregularities [*Buchau et al.*, 1983, 1985; *Weber et al.*, 1984, 1986] found in the polar cap. They are localized enhancements in F layer density observed in the polar cap with horizontal dimensions of a few hundred kilometers to 1000 kilometers. The peak plasma density in these patches (dependent on season, solar cycle and the geomagnetic activity) is about 8×10^5 el/cc (in winter with solar maximum and a moderate geomagnetic activity), which is an eight-fold increase over the background plasma. Patches can form during variations in the B_z (and B_y to some extent) component of the Interplanetary Magnetic Field (IMF), which acts to break up the TOI. They consequently get detached from the dayside auroral ionosphere and drift anti-sunward across the polar cap into the midnight auroral zone with speeds of 250-700 m/s [*Buchau et al.*, 1983, *Weber et al.*, 1984].

Figure 1 shows a classic patch event reported by *Hill* [1963]. The three f_0F_2 contour plots built from ionograms show the temporal evolution of a patch in the northern polar region. In Figure 1c we can see a strong poleward intrusion of higher valued f_0F_2

contours from the mid-latitudes. Note the penetration of dayside plasma into the nightside as indicated by the crossing of the contours past the solar terminator (dashed curve). The patches are detached when the high density plasma from the mid latitudes can no longer flow poleward due to apparent change in the convection pattern. We will discuss more about the detachment process later.

Another view of the patches is shown in Figure 2. The lower trace shows measurements of variations in Total Electron Content (TEC) using dual-frequency transmissions from the Global Positioning Satellite (GPS) seen at Thule, Greenland [*Weber et al., 1986*]. Multiple patches as indicated by jumps in TEC can be seen during the 5-hour period with considerable structure within each patch. Much work has been done to trace the source of the enhanced ionization in the patches. The large convection speeds observed during patch formation and evolution tend to rule out soft particle precipitation in the cusp/cleft region as a possible source. Modeling results [*Knudsen* 1974; *Knudsen et al.*, 1977] indicate that enhanced anti-sunward convection speeds should result in significantly smaller ionization buildup than that found in the patches since a magnetic flux tube spends less time in the cleft region. Many experiments have shown that the patch ionization is solar radiation produced and appears to originate from a region equatorward of the dayside cusp region. Figure 3 [*Buchau et al.*, 1985] shows that all the peak plasma densities measured in the winter polar cap (dots in the center panel) were consistent with the density expected from solar production (dashed curve).

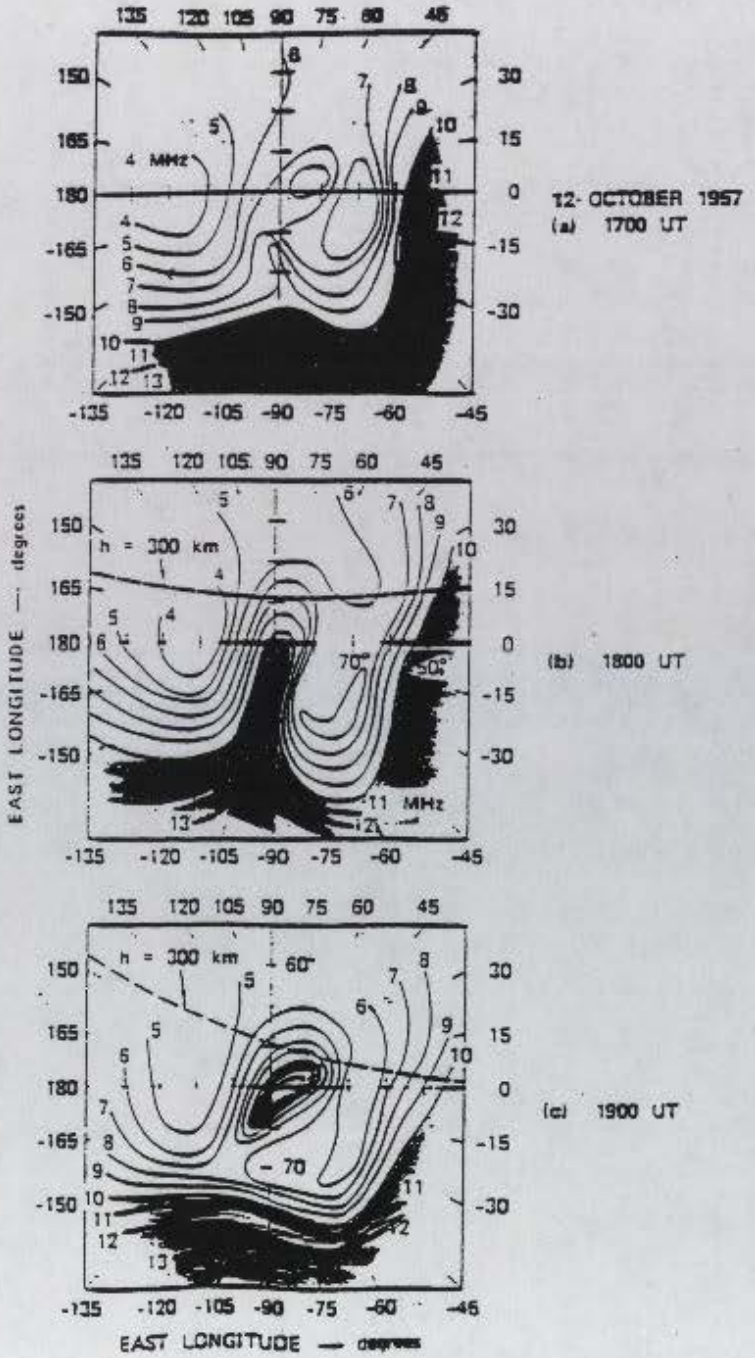

Figure 1. Sequence of contour maps of f_0F_2 values tracing the development of a polar cappatch [*Hill*, 1963].

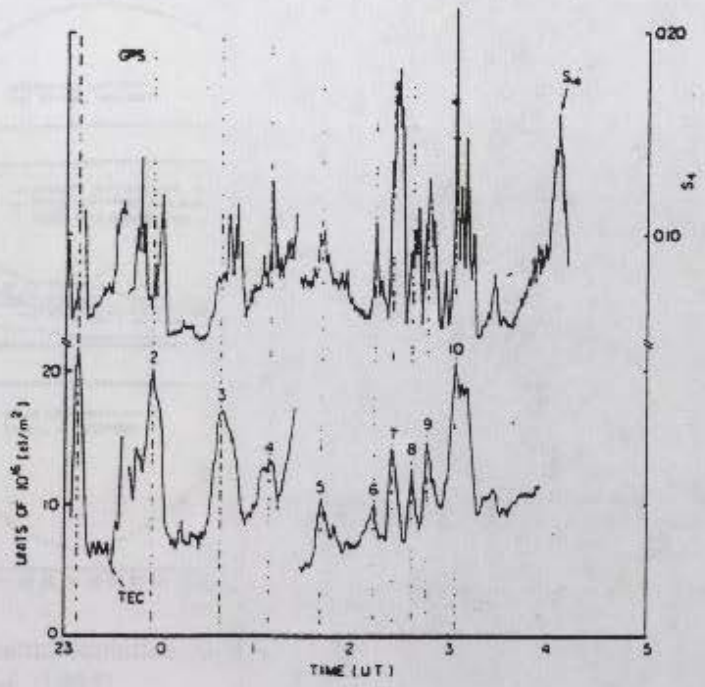

Figure 2. Total electron content variations associated with polar cap patches (lower trace) [*Weber et al., 1986*].

Though it has been widely accepted that the patches are huge parcels of solar-produced plasma (historically referred as the "Tongue Of Ionization" [TOI]) convecting from the dayside subauroral ionosphere through the cusp and across the polar cap [*Tsunoda, 1988, and references therein*], the exact mechanism of the patch formation and detachment is still under discussion and investigation. Several models of convection dynamics have been proposed to explain the patch formation. *Anderson et al.* [1988] proposed that the polar cap expansion in response to K_p changes brings high-density plasma into the cusp region. *Lockwood and Carlson* [1992] argued that Flux Transfer Event (FTE) signatures in the cusp cause short-lived enhanced flows that transport

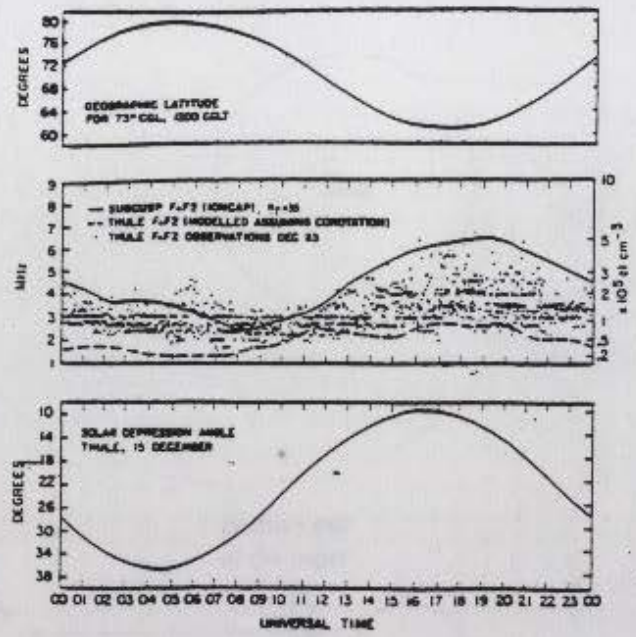

Figure 3. Peak plasma densities measured in the winter polar cap (dots in the center panel) [*Buchau et al.*, 1985].

plasma into the polar cap. *Sojka et al.* [1993] used time varying IMF B_y to alter convection patterns that led to patches forming from the TOI.

The most investigated cause is the one associated with the variations in the B_z and the B_y component of the IMF. Figure 4 shows the vector orientation of the IMF components in the geocentric solar ecliptic (GSE) coordinate system. Note that the B_z component of the IMF is north-south, parallel to earth's magnetic axis (positive northwards).

Figure 5 [*Potemra*, 1983] shows the magnetic field line connections between the IMF and the geomagnetic field for southward IMF ($B_z < 0$) and northward IMF ($B_z > 0$). *Tsunoda* [1988] has explained the patch formation process by considering changes in the IMF B_z and B_y components. When B_z turns south, the auroral oval (and associated

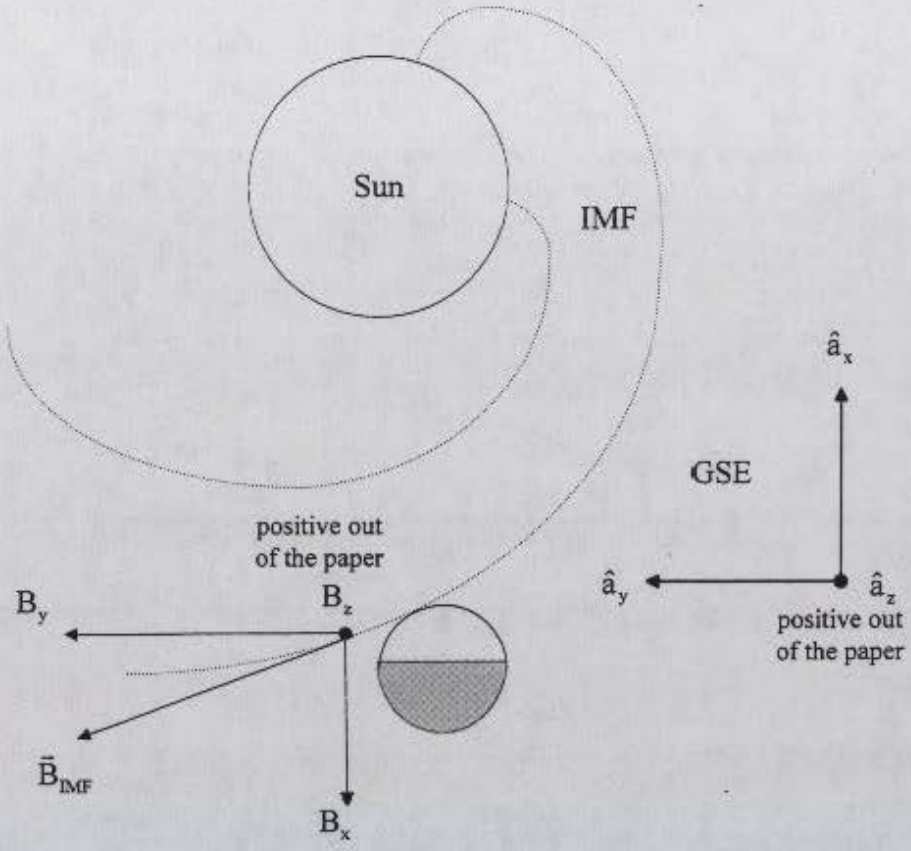

Figure 4. Orientation of the IMF components in the GSE coordinate system.

electric fields) expands to lower latitudes accompanied by a two-cell convection pattern with increased convection speeds. The solar-produced subauroral plasma is drawn into the polar cap by a resultant eastward electric field. When B_z turns northward again, it retracts the eastward electric field (a westward electric field does not develop), detaching the TOI from the following mid-latitude plasma. Thus the TOI is drawn into patches by the changing IMF B_z and B_y components, which relocate the cusp equatorward and, poleward, respectively, for B_z changes and directs flow out of the cusp towards dusk for B_y negative and dawn for B_y positive (in the northern hemisphere). The Air Force Geophysics Laboratory (AFGL) group (now the Phillips Laboratory) [*Buchau et al.*,

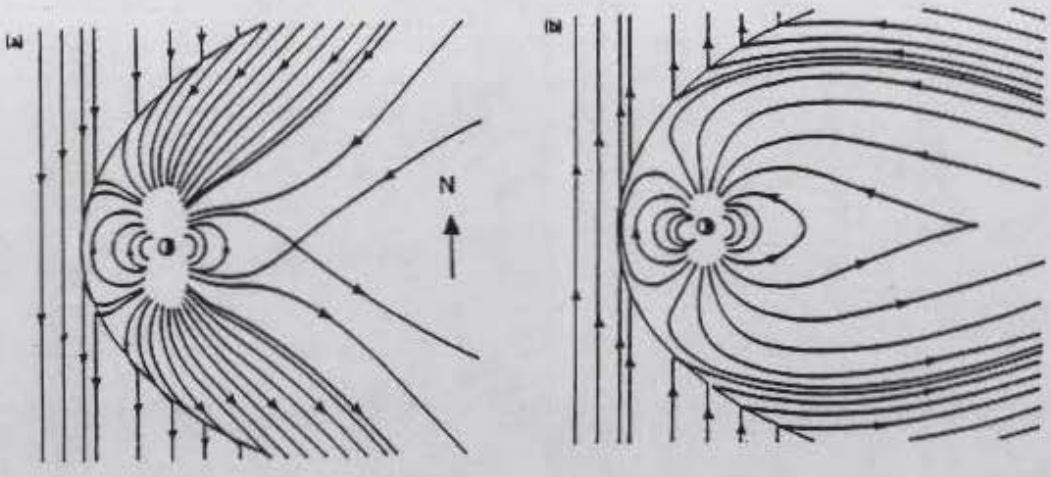

Figure 5. Magnetic field line connections between the IMF and the geomagnetic field for southward IMF when $B_z < 0$ (a) and northward IMF when $B_z > 0$ (b) [*Potemra*, 1983].

1983, 1985; *Weber et al.*, 1984, 1986] found that the patches occurred when the B_z component of the IMF is southward or when $K_p > 4$. *Sojka et al.* [1993] have simulated the patch formation using two independent physical models, viz., the Phillips Laboratory F region model and the USU TDIM [*Schunk*, 1988; *Sojka* 1989]. They temporally varied the magnetospheric electric field input to the models. This imposed convection variations comparable to changes in the convection pattern that result from changes in the B_y IMF component for southward IMF. Their results using the TDIM are shown in Figure 6. They have concluded that time-varying convection in the high latitudes under southward IMF conditions can produce the density enhancements. observed in the polar cap that are referred to as patches. Their result is of importance since their simulations will be used to study the GDI in the high latitudes.

Figure 6. Series of N_eF_2 snapshots from TDIM simulation [*Sojka et al.*, 1993].

2.3.2. *Boundary (and Subauroral) Blobs*

These are the next large-scale structures after the patches. The boundary blobs are latitudinally narrow (extreme longitudinal extent), altitude-extended slabs of enhanced F region plasma with long temporal persistence. They are so called because of their proximity to the equatorward auroral boundary. Figure 7 shows examples of boundary blobs observed during radar elevation scans in the magnetic meridian [*Rino et al.*, 1983]. The boundary blobs, shown by a shaded region with density contours greater than 8×10^5 el/cc, are situated above the equatorward edge of the auroral E layer.

Subauroral blobs resemble the boundary blobs but are found in the ionospheric trough region, equatorward of the auroral E layer. The shaded region 500 kilometers north of the radar (in the first radar scan) is the subauroral blob.

The topological similarity among the patches, boundary blobs, and subauroral blobs suggests that these two blobs result from the temporal evolution of the patches. Using the two-cell convection model [*Heelis et al.*, 1982], *Robinson et al.* [1985] modeled the reconfiguration process in which a circular patch in the polar cap convects into the nightside auroral zone and distorts into a latitudinally confined blob that extends over many degrees of longitude. Figure 8 shows the model results at hourly intervals. Many experimental results support patch reconfiguration as the dominant source of boundary and subauroral blobs [*Tsunoda*, 1988, *and references therein*]. There is also evidence that soft particle precipitation contributes to the ionization in the boundary blobs.

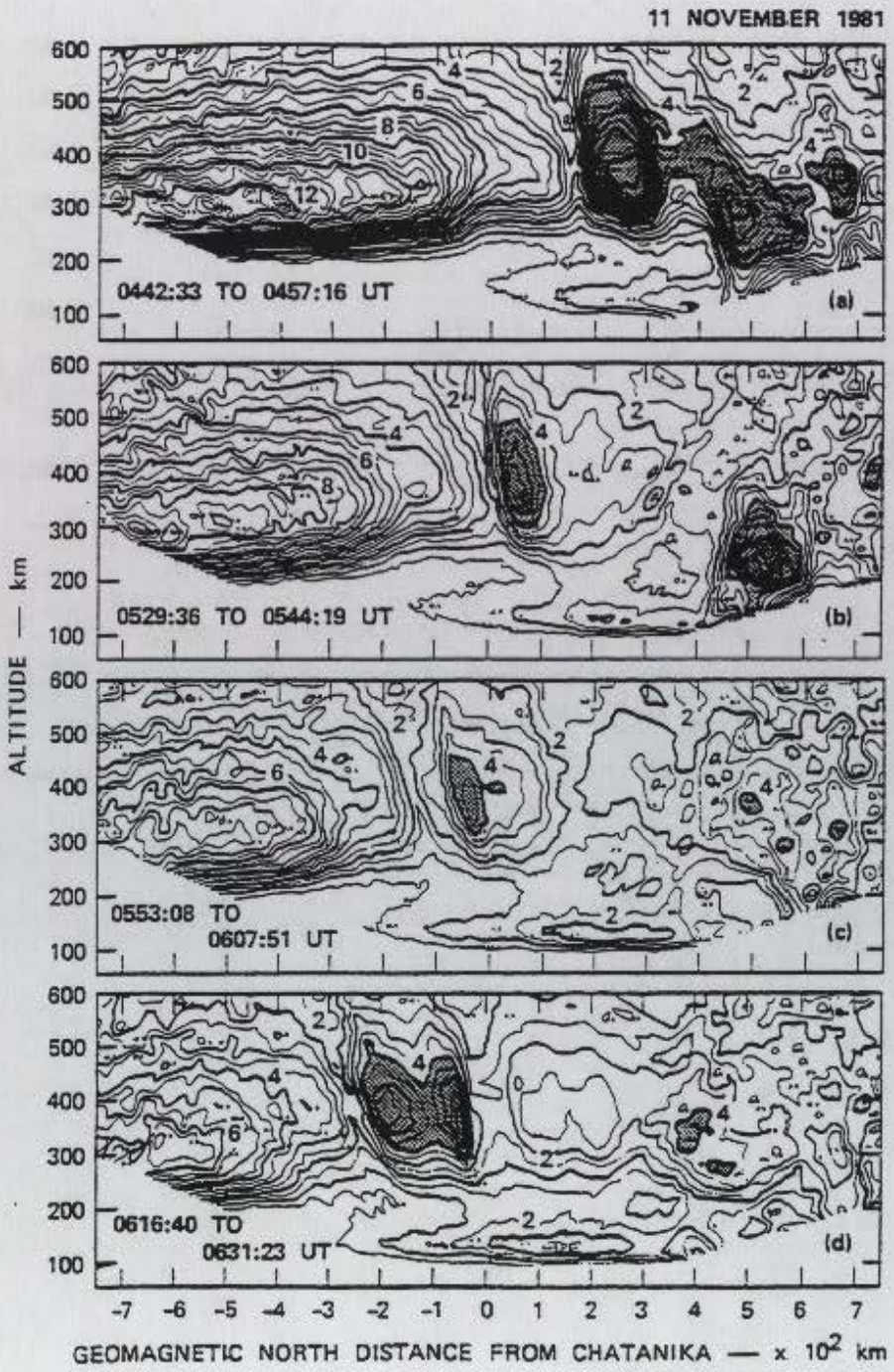

Figure 7. Plasma density contours measured during radar elevation scans in the magnetic meridian showing a boundary blob and an auroral blob [*Rino et al.*, 1983].

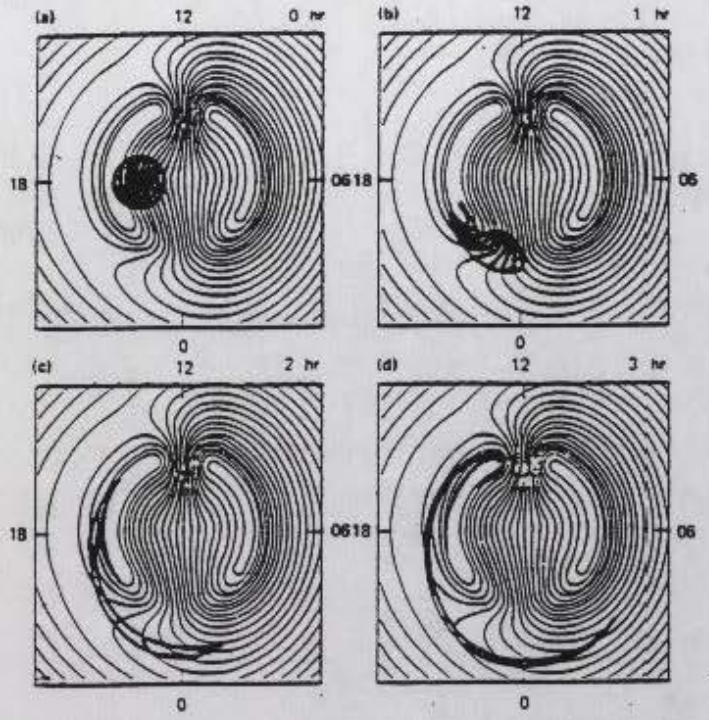

Figure 8. Model results of a patch distorting into a boundary blob [*Robinson et al.*, 1985].

2.3.3. *Sun-Aligned Arcs, Auroral Blobs, and Localized Depletions*

More research is still required to understand these structures. However, we are familiar with certain basic features. Sun-aligned arcs are usually aligned with the noon-midnight meridian. Under quiet solar conditions they are found in the polar cap. The maximum plasma density has a solar cycle dependence and is typically about 10^6 el/cc (4 times that of the background plasma). There is evidence that soft particle precipitation makes significant contribution to the plasma density in the arcs [*Buchau et al.*, 1983; *Carlson et al.*, 1984].

Auroral blobs are observed in the auroral oval (see Figure 7) restricted in longitudinal extent. They seem to favor the night-time regions. Sun-aligned arcs may be the source for the auroral blobs. Case studies show that the F region plasma density can be locally depleted near the poleward auroral boundary probably as a result of aeronomical changes produces by large electric fields [*Tsunoda,* 1988, *and references therein*].

CHAPTER 3

GRADIENT DRIFT INSTABILITY

3.1. Signatures of Gradient Drift Instability in the Polar Cap Patches

We will now look at some experimental results that show a high spatial correlation between intense small-scale irregularities and steep transverse gradients that characterize the walls of the large-scale plasma structures discussed in the previous chapter. These results logically suggest fluid interchange instabilities such as GDI as dominant players in irregularity generation.

In reference to Figure 2 [*Weber et al.*, 1986], showing patches as seen from Thule using GPS satellite transmissions at 1.2 GHz, notice variations in the scintillation intensity (S_4 --a commonly accepted measure of signal fluctuation caused by ionospheric irregularities) in the upper trace, especially in the patches numbered 3, 7, and 8. There is an increase in the amplitude of the scintillation on the trailing edge characterized by a steep density gradient. This physical situation is the most ideal for the onset of the GDI. Figure 9 [*Basu et al.*, 1994] shows the temporal variations of the S_4 scintillation index from spaced-antenna measurements using 243 MHz transmissions from a quasi-stationary polar beacon satellite. The top panel shows measurements made at Sondrestrom and the bottom panel measurements at Thule. Notice the enhanced scintillation after 1200 UT at Sondrestrom and after 1145 UT at Thule. An important observation is that the trailing edges (the edge close to midnight sector; see Figure 16) of the scintillation structures are steeper than the leading edges, leading the authors to postulate GDI as the agent for these

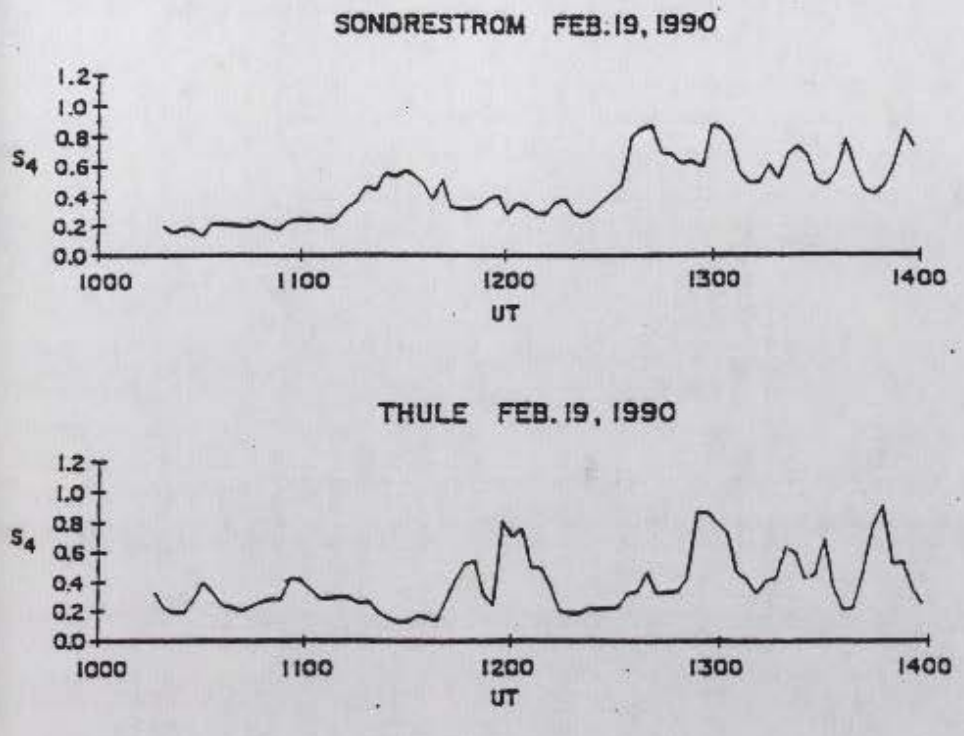

Figure 9. Temporal variation of scintillation intensity index (S_4) [*Basu et al.*, 1994].

meter-scale irregularities.

Figure 10 shows the results from measurements using the Aureol 3 spacecraft [*Cerisier and Berthelier,* 1985]. The amplitude of the density fluctuations are in the frequency range of 20 to 400 Hz (wavelength between 20 and 400 meters). The figure clearly shows density and electric field fluctuations are correlated with positive large-scale density gradients found along the trailing edge. Also notice the electron density profile (bottom panel) shows a turbulent structure along the trailing edge. These results strongly suggest GDI as the source mechanism.

Figure 11 is another set of results from the Aureol 3 spacecraft. The top panel shows rapid small-scale fluctuations along the positive (upward sloping) gradients in

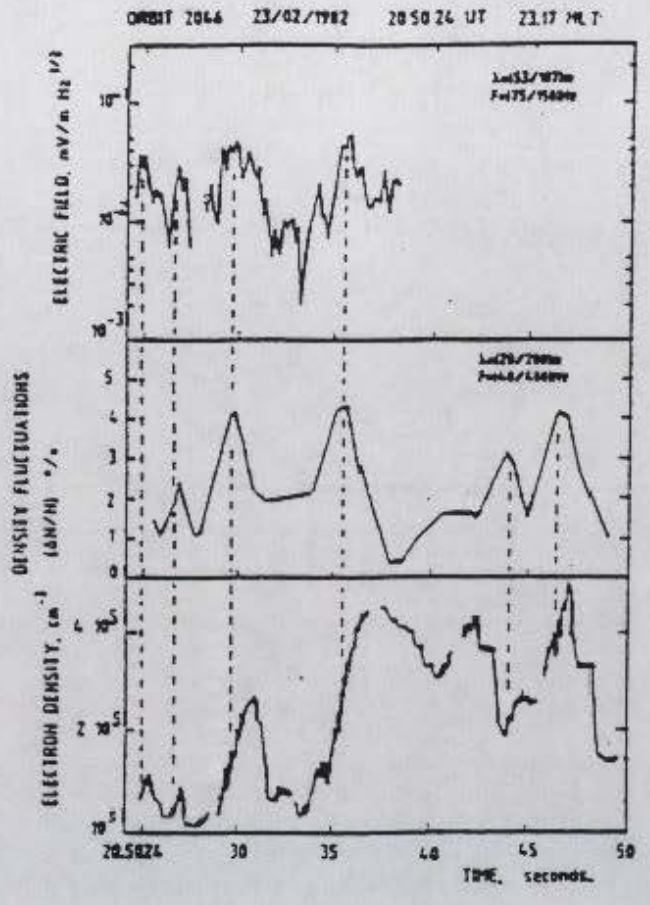

Figure 10. Electric field and electron density fluctuations and electron density profile measured by Aureol 3 spacecraft [*Cerisier and Berthelier,* 1985].

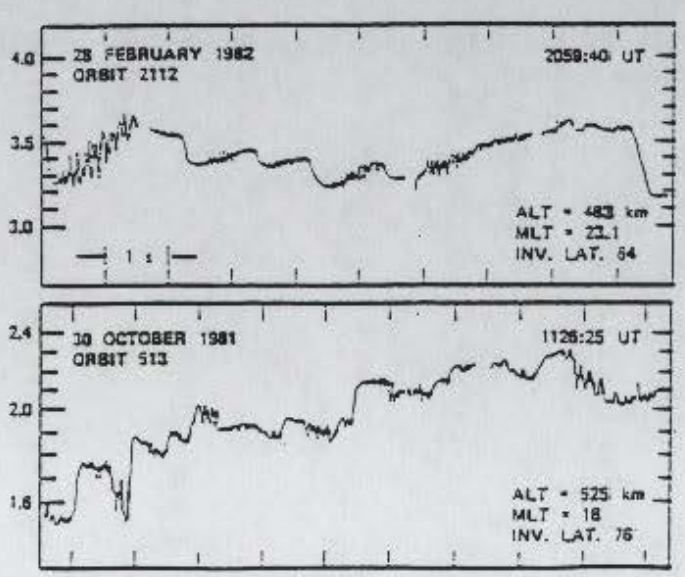

Figure 11. Electron density fluctuations measured by Aureol 3 spacecraft [*Cerisier and Berthelier,* 1985].

plasma density. There is complete absence of similar fluctuations along the negative gradients along the trailing edge. The second panel shows similar results reversed left to right.

From the above observations and also from most other measurements of this kind, we can say that kilometer-scale irregularities populate the bulk of the patch structure with a tendency for enhanced irregularities to occur along the trailing edge of the patches. The edges have a large density gradient which, together with the ambient electric field and the background magnetic field, offers a very favorable condition for the onset of the GDI.

3.2. Physics of the Gradient Drift Instability

The GDI is otherwise known as $\vec{E} \times \vec{B}$ instability. This is an interchange instability and needs an electric field, a magnetic field, and a density gradient orthogonal to each other. We will consider four different configuration of these three inputs, the first two of which belong to the $\vec{E} \times \vec{B}$ category, while the last two are mentioned for book-keeping purposes.

3.2.1. *Case 1a*

This is the case that will be the focus of this thesis. Figure 12 shows the orientation of the electric, magnetic, and the density gradient vectors. The ambient (background) electric field $\vec{E}_0$ is along the negative $\hat{x}$ direction, the ambient magnetic field $\vec{B}_0$ is along the positive $\hat{z}$ direction (up and out of the page), and the density

gradient $\vec{\nabla}n$ is along the positive $\hat{y}$ direction. $\vec{V}_d = \frac{\vec{E}_0 \times \vec{B}_0}{B^2}$ is the drift velocity and is parallel to the density gradient.

At the altitudes of interest, the electrons have higher gyro frequency than collision frequency while the ions have higher collision frequency than gyro frequency. This along with the ambient electric field $\vec{E}_0$ causes the ions to drift along $\vec{E}_0$ (the Pedersen's direction). In the high-density regions, more ions move to the left, i.e., along $\vec{E}_0$ (refer Figure 12) than in the lower density regions. Now let us impose a sinusoidal perturbation δn on the medium. The imbalance in the number of ions moving left in the high-density and in the low-density regions leads to charge accumulation on the boundaries. This charge accumulation is net positive on the boundary where more ions arrive than leave and is net negative on the boundary where more ions leave than arrive. This fact is indicated by '+' and '-' signs on Figure 12. A polarization electric field $\vec{E}_p$ develops because of this charge imbalance along the boundary. This further causes a drift of the charged particles in the $\vec{E}_p \times \vec{B}_0$ direction, driving less dense plasma into regions of more dense plasma and vice versa. Note that the direction of the plasma drift is such as to increase the amplitude of the perturbation. The above sequence repeats until the density gradients are finally smoothed out. However, since the amplitude of the perturbation grows, the plasma becomes unstable and we have a growing instability. This instability is what structures the edges of the patches and seeds the different high-latitude structures.

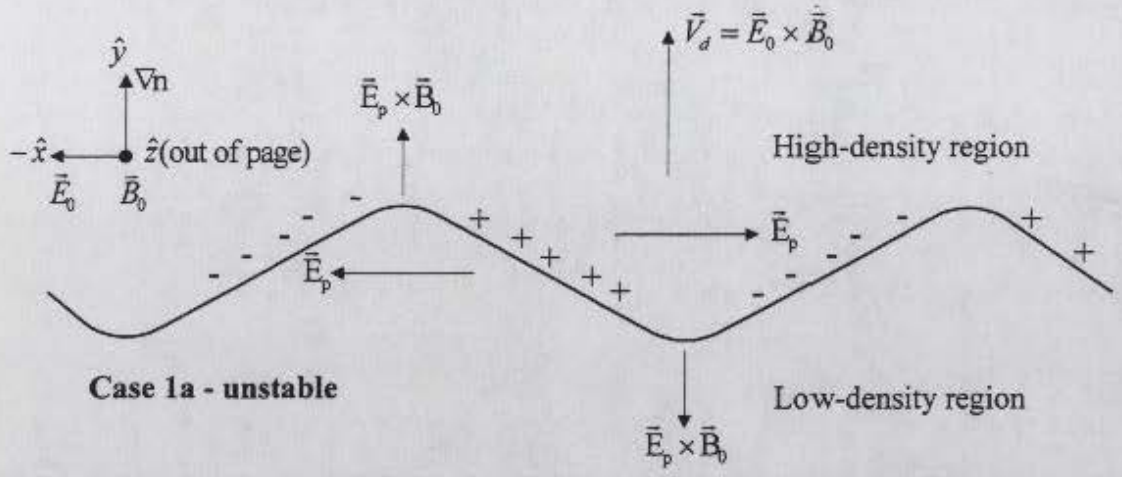

Figure 12. Schematic showing the development of the GDI or the $\vec{E} \times \vec{B}$ instability for the case 1a.

3.3.2. *Case 1b*

In this case the direction of the density gradient is opposite to that of the previous case (see Figure 13). The drift velocity $\vec{V}_d$ is now anti-parallel to the density gradient. Consequently, the charge accumulation on the boundaries is opposite to that discussed in the previous case, which in turn sets up a polarization field in the opposite direction. The resulting $\vec{E}_p \times \vec{B}_0$ drift dampens the amplitude of the perturbation by moving kinks found in the low-/high-density boundary back towards the boundary. The perturbation has no effect on the plasma. The instability dies out and the medium is stable.

3.2.3. *Case 2a*

In this case the density gradient and the electric field are parallel to each other (see Figure 14). The drift velocity $\vec{V}_d$ is perpendicular to the density gradient in the direction shown.

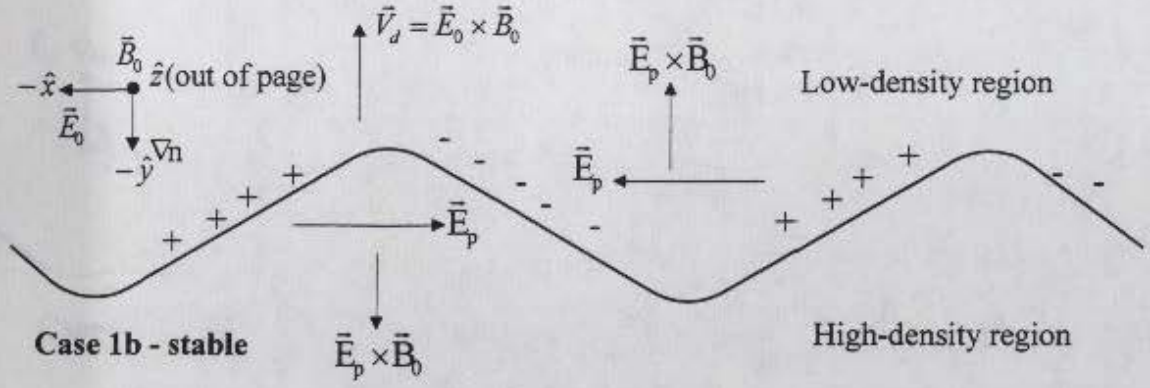

Figure 13. Schematic showing the development of the GDI or the $\vec{E} \times \vec{B}$ instability for the case 1b.

Initially $\vec{E}_0 \times \vec{B}_0$ force drives the electrons and the ions to the right. The electrons lead the ions since they have a higher gyro frequency than the ions. The number of electrons and ions drifting to the right is more in the high-density regions than in the low density regions. Consequently, when a perturbation is imposed on the medium, a particular charge accumulates along its boundary. Positive charges collect on the boundary where more ions arrive than leave, and negative charges collect along the boundary where more electrons arrive than leave (see Figure 14). A polarization electric field $\vec{E}_p$ develops due to this charge imbalance along the boundary. The resulting $\vec{E}_p \times \vec{B}_0$ drift causes less dense plasma to drift into regions of more dense plasma and vice versa. The amplitude of the perturbation increases and the medium is eventually structured due to the growth of the instability, until the density gradients are finally smoothed out.

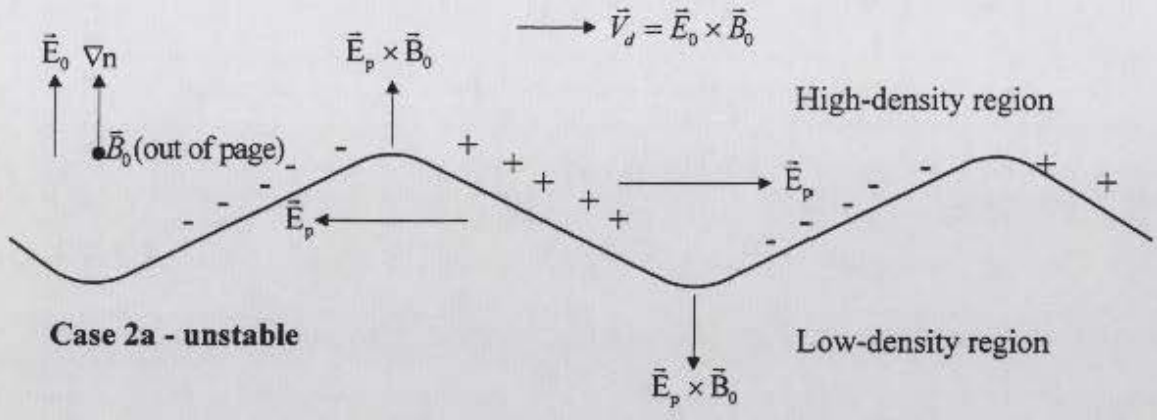

Figure 14. Schematic showing the development of the GDI or the $\vec{E} \times \vec{B}$ instability for the case 2a.

3.2.4. *Case 2b*

This is the opposite of the previous case (see Figure 15). The electric field and the density gradient are anti parallel. The charge accumulation is opposite and the resulting $\vec{E}_p \times \vec{B}_0$ drift decreases the amplitude, thereby dampening the perturbation. The medium is hence stable.

Figure 16 shows a schematic of a patch in the polar ionosphere. The arrow heads indicate that the patch is convecting anti-sunward with the drift velocity $\vec{V}_d$. The four cases discussed above occur along the edges of the patch as indicated in this schematic. Case (1a), which is the most unstable case, occurs along the trailing edge of the patch where the drift velocity is parallel to the density gradient. Case (1b), which is a stable configuration, occurs along the leading edge of the patch. Case (2a), the other unstable case, is found on the left edge of the patch. Finally, case (2b), a stable case, is found on the right edge of the patch.

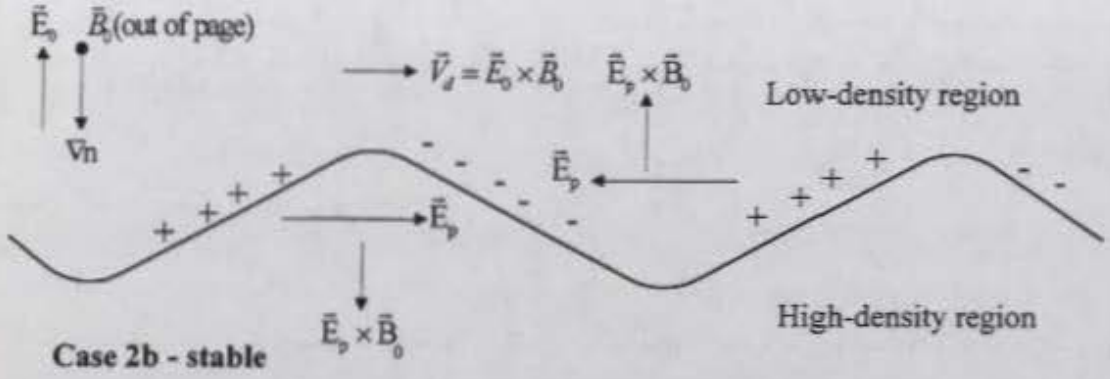

Figure 15. Schematic showing the development of the GDI or the $\bar{E} \times \bar{B}$ instability for the case 2b.

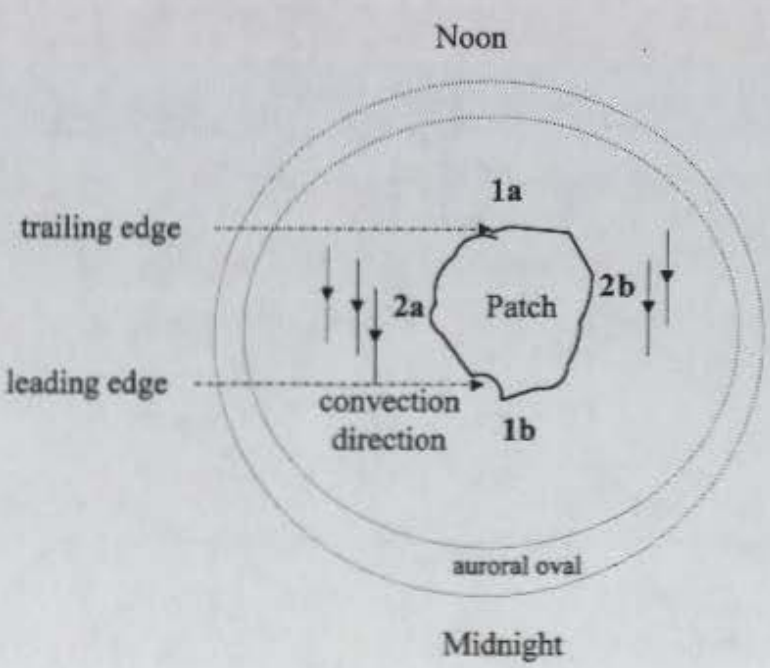

Figure 16. Cartoon showing the occurrence of the various instability cases in a patch.

Figure 17 shows the model results of *Keskinen and Ossakow* [1982]. Their work is an excellent example of the GDI caused by the unstable configuration discussed in case (1a). Recall that this case occurs along the trailing edge of the patch as it convects anti-sunward. They modeled the linear and nonlinear evolution of plasma enhancements in the diffuse auroral F region ionosphere at 350 kilometer altitude using approximate ionospheric parameters in their theoretical results. However' they used a scale length of about 20 kilometer., which corresponds to a steep density gradient. The plots show isodensity contours at four time steps. Though their purpose is not exactly what is pursued in this thesis, the figure is an excellent illustration for the growth of the instability and its structuring of the plasma.

3.3. Theoretical Framework of the Gradient Drift Instability

In order to investigate the effectiveness of the GDI in structuring the polar cap patches, we need to know the growth rate of the instability as it occurs in the patches. In the following section, we will look at the basic equations and the outline of the procedure followed to arrive at the growth rate.

Recall that the GDI is a macro instability since its scale size is much larger than the ion or electron gyro radius. This allows us to assume a Maxwellian velocity distribution and work in the fluid domain. Hence the basic equations used are the fluid equations comprising of the continuity equation, the momentum equation, the equation of state, and Maxwell's electromagnetic equations. Before we proceed, note that henceforth

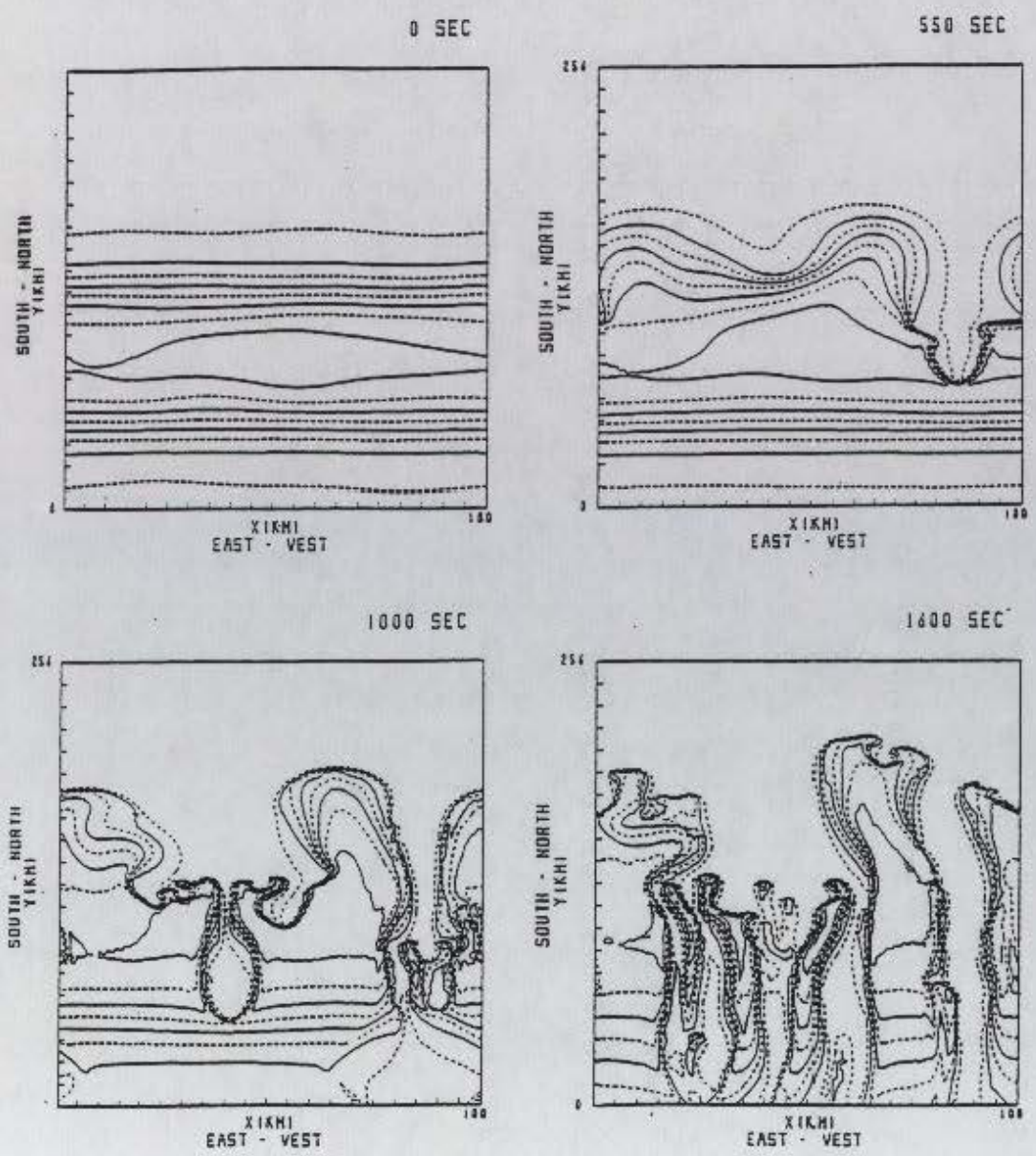

Figure 17. Isodensity contour plots from model results showing the evolution of the $\vec{E} \times \vec{B}$ instability [*Keskinen and Ossakow*, 1982].

we will be using cgs units throughout our discussion. Also refer to the list of symbols and notation for the meaning and significance of the symbols and notation that will be used henceforth. Any symbols or notations not present in this list will be explained as they occur.

3.3.1. *The Fluid Equations*

3.3.1.1. The Continuity Equation

This equation follows from the conservation of mass, which says that the change in the number of particles in a fixed volume depends on the net flux of the particles across the surface bounding that volume and also depends on any sources or sinks present inside that volume. It is given by the following equation where P_α is the production rate and L_α is the loss rate of the species α.

$$\frac{\partial}{\partial t}\left(n_\alpha\right) + \nabla.\left(n_\alpha \bar{u}_\alpha\right) = P_\alpha - n_\alpha L_\alpha \qquad (1)$$

3.3.1.2. The Momentum Equation

This equation follows from the conservation of momentum or the equation of motion. It is given by the following equation for the species α.

$$n_\alpha m_\alpha\left[\left(\frac{\partial}{\partial t}+\vec{u}_\alpha\cdot\nabla\right)\vec{u}_\alpha\right]+\nabla p_\alpha-n_\alpha m_\alpha\vec{g}+\nabla\cdot\vec{\tau}$$
$$-n_\alpha e_\alpha\left[\vec{E}+\frac{1}{c}\left(\vec{u}_\alpha\times\vec{B}\right)\right]=n_\alpha m_\alpha\sum_{\substack{\beta\\ \alpha\neq\beta}}\nu_{\alpha\beta}\left(\vec{u}_\beta-\vec{u}_\alpha\right) \quad (2)$$

The first term in the left-hand side of the above equation is the convective derivative term which represents the change in the velocity in a frame moving with the fluid element. The second term represents the pressure gradient force, the third term represents the gravitational force, the fourth term is the stress force, and the final term is the Lorenz force. The right-hand side represents the collision forces of the species α with all other species β.

3.3.1.3. Equation of State

This is from thermodynamics and is given by

$$p = C\rho^{\gamma} \quad (3)$$

But a more useful form is obtained by taking the gradient of (3), viz.,

$$\nabla p_\alpha = K\gamma_\alpha T_\alpha \nabla n_\alpha \quad (4)$$

3.3.2. *Electromagnetic Equations*

These are just the four Maxwell's equations and the Lorenz electromagnetic force.

$$\nabla\cdot\vec{E} = 4\pi e\left(n_i - n_e\right) \quad (5)$$

$$\nabla \cdot \vec{B} = 0 \tag{6}$$

$$\nabla \times \vec{E} = -\frac{1}{c}\frac{\partial \vec{B}}{\partial t} \tag{7}$$

$$\nabla \times \vec{B} = \frac{4\pi}{c}\vec{J} + \frac{1}{c}\frac{\partial \vec{E}}{\partial t} \tag{8}$$

$$\vec{E} + \frac{1}{c}\vec{u} \times \vec{B} = F_L \tag{9}$$

3.3.3. *Procedure for Deriving the Growth Rate*

The following section gives a brief outline of the various steps to be followed to arrive at an expression for the growth rate. Linear perturbation techniques are employed together with various assumptions and of course mathematical wizardry. I desist from including a detailed derivation because each expression for the growth rate is unique with a lot of intermediary steps. It is not instructive to try and derive all of them, especially since literature giving the details is available (*Ossakow et al.,* 1978; *Huba and Zalesak,* 1983; *Huba et al.,* 1983; *Keskinen and Ossakow,* 1983). However, the following steps are common in most derivations.

Step 1. Equations (1) through (9) are first simplified by adapting them to the ionospheric region of interest. For example, in our situation we will be using them in the high-latitude F region where plasma transport dominates over either production or loss processes. So in the continuity equation (1) we can neglect the production and loss terms in the right hand side.

Step 2. Assumptions are made to simplify the problem. By making assumptions we solve the problem in various domains or regions. For example, instead of using an arbitrary orientation of the electric field, which is the realistic case, we may choose to concentrate on the component of the electric field that is perpendicular to the density gradient. By doing this we now have to worry about only one component of the electric field instead of solving for all three components. This step is probably the most important step. In further sections where we will be using the different growth expressions, we will try to justify the assumptions made to arrive at that growth expression.

Step 3. The plasma parameters are perturbed about their equilibrium values (mostly fixed in the previous step). For example, the electron density n_e is replaced by $n_0 + n_1$, where n_0 is the equilibrium value of the electron density and n_1 is the small perturbation applied to the electron density.

Step 4. Linearize the perturbed equations, i.e., neglect all second-order terms. This ensures that the problem does not spill over to the nonlinear domain, which makes it so much easier to solve. Moreover it might be impossible to solve them in the nonlinear domain. For example, we can neglect terms like n_1^2, $n_1 E_1$, etc.

Step 5. Assume plane wave solutions, i.e., apply only sinusoidal perturbations. For example, the density perturbation is of the form $n_1 = \hat{n}_1 \exp[i(kx - \omega t)]$. This assumption will let us replace $\frac{\partial}{\partial t}$ with $-i\omega$ and ∇ with $i\vec{k}$.

Step 6. Solve the set of simultaneous linear equations and arrive at the dispersion relation.

Step 7. Find the roots of the dispersion relation. If any or all of the ω's have positive imaginary parts, the perturbation grows in time. Negative imaginary roots indicate damping and stability. The growth rate is the imaginary part of ω.

The procedure outlined above has been used by the respective authors in deriving the various growth rate expressions. In the next chapter we will study these expressions in detail.

CHAPTER 4

IONOSPHERIC DATASET, GRADIENT DRIFT INSTABILITY ASSUMPTIONS, AND GROWTH EXPRESSIONS

4.1. Time Dependent Ionospheric Model

The Utah State University Time Dependent Ionospheric Model (TDIM) is a (O_2^+, N_2^+, NO^+, O^+, N^+, and He^+) multi-species global model of the ionosphere that is based upon the solution of the continuity, momentum, and energy equation in the collision-dominated 13-moment transport formulation. The development of this model is described by *Schunk* [1988], while the model predictions and comparisons with observations are described by *Sojka* [1989]. The model provides the density profiles of the ions mentioned above and the electron and ion temperature profiles. It also provides the density and temperature profiles of the neutrals. The MSIS-86 [*Hedin*, 1987] model is used to represent the neutral atmosphere.

4.2. The Data set

A polar cap patch was simulated using the USU TDIM model. The model generated densities and temperature profiles for the ions and neutrals over a patch simulation region with 2035 pixels (bins), with each bin having a size of 70×70 kilometers at 100 kilometers altitude. A single trajectory was followed for each pixel; hence, 2035 trajectories were followed for over 24 hours to generate a single patch snapshot in time. For each bin the altitude ranged from 90 kilometers to 800 kilometers with more resolution in the lower altitude region. The geomagnetic activity was set at a

moderate K_p of 3.5, and the solar maximum condition with a $F_{10.7}$ index of 210 was used. The date of the simulation was the 357th day of 1981 (northern winter). All these parameters were maintained constant over the entire simulation period. The ion species data were for the major ions O_2^+, NO^+, and O^+, and the neutral species data was for O, N_2, and O_2.

As regards the inputs to the TDIM model, the MSIS-86 was used as the neutral atmosphere. The *Heppner and Maynard* [1987] unvarying "A" convection pattern was used. Figure 18a illustrates this convection pattern. The auroral oval parameters, specifically the electron energy flux and average energy, were obtained from the *Hardy et al.* [1987] model. With the above inputs a TOI was generated at 75600 seconds UT. The data set obtained from this simulation will be henceforth referred to as "data set 1."

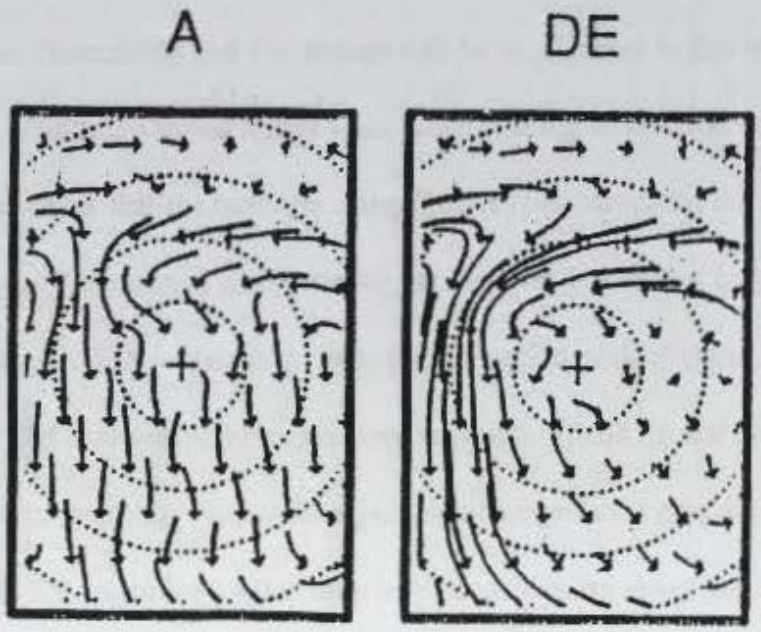

Figure 18. (a) *Heppner-Maynard* "A" convection pattern used in the TDIM simulation, (b) *Heppner-Maynard* "DE" convection pattern [*Sojka et al.*, 1993].

The data set for the second part of the growth rate ("data set 2") study, involves, following a plasma flux tube in time with change in the electric field, as described in chapter 5.

The *Heppner-Maynard* pattern was used throughout the simulation but the "A" pattern is augmented with both the "DE" (Figure 18b) and the "BC" pattern. They represent the IMF for strong B_y negative and positive, respectively. The procedure followed in generating the data set follows the one by *Sojka et al.* [1993], to simulate the patches. K_p and $F_{10.7}$ values were the same as used before and so is the simulation date. The snapshots of the patches begin at a UT of 2115 hours (76500 seconds) and end at a UT of 2200 hours (79200 seconds) with a snapshot every 5 minutes, for a total of 10 snapshots. The position of a grid point in successive snapshots was also known.

The area of interest is shown in Figure 19 superimposed on the NmF_2 pattern Henceforth all our illustrations and discussions will be in reference to this area in the polar cap region. Figure 20 shows a gray scale plot of the log of electron density at four different altitudes. Note that the numbers along the axes just stands for the index numbers of the two- dimensional grid in which the data was placed and have no spatial significance. A classic TOI is shown in panel (c) at F region peak of about 364 kilometers. The TOI is absent at lower altitudes in panels (a) and (b) and fades away at an higher altitude in panel (d). Notice the significant change in the gray scale along the edges of the TOI. This signifies a sharp drop in electron density along the edges, leading to steep density gradients. The density gradient along the left of the figure is opposite to that on the right. The associated *Heppner-Maynard* convection pattern is illustrated in

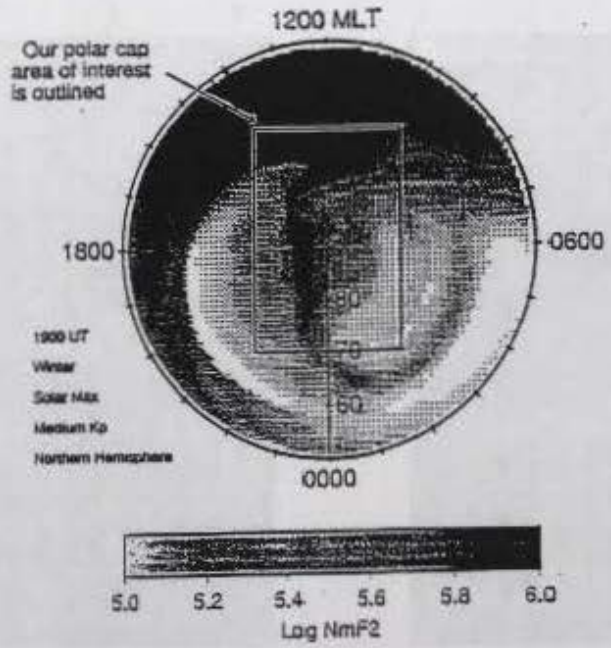

Figure 19. The rectangular box shows the patch simulation region. This is the region of interest.

Figure 21 and is superimposed on the electron density pattern, clearly showing the plasma flow into the TOI. Figures 22, 23, and 24 show the ion, electron, and neutral density, and the temperature altitude profiles at an arbitrary magnetic latitude of 69.81 and longitude of 221.82 degrees.

4.3. Growth Rates

Now that we have discussed the model data and the region of interest, let us look at some growth rates for the GDI expressions that have been derived by various researchers. We will look at the simplest case, then show how other complex growth expression can be converted to the simplest case by specializing to certain domains, thereby using the model data effectively. Before we do that, let us list the basic assumptions that are common in all the derivations for the growth rates discussed below.

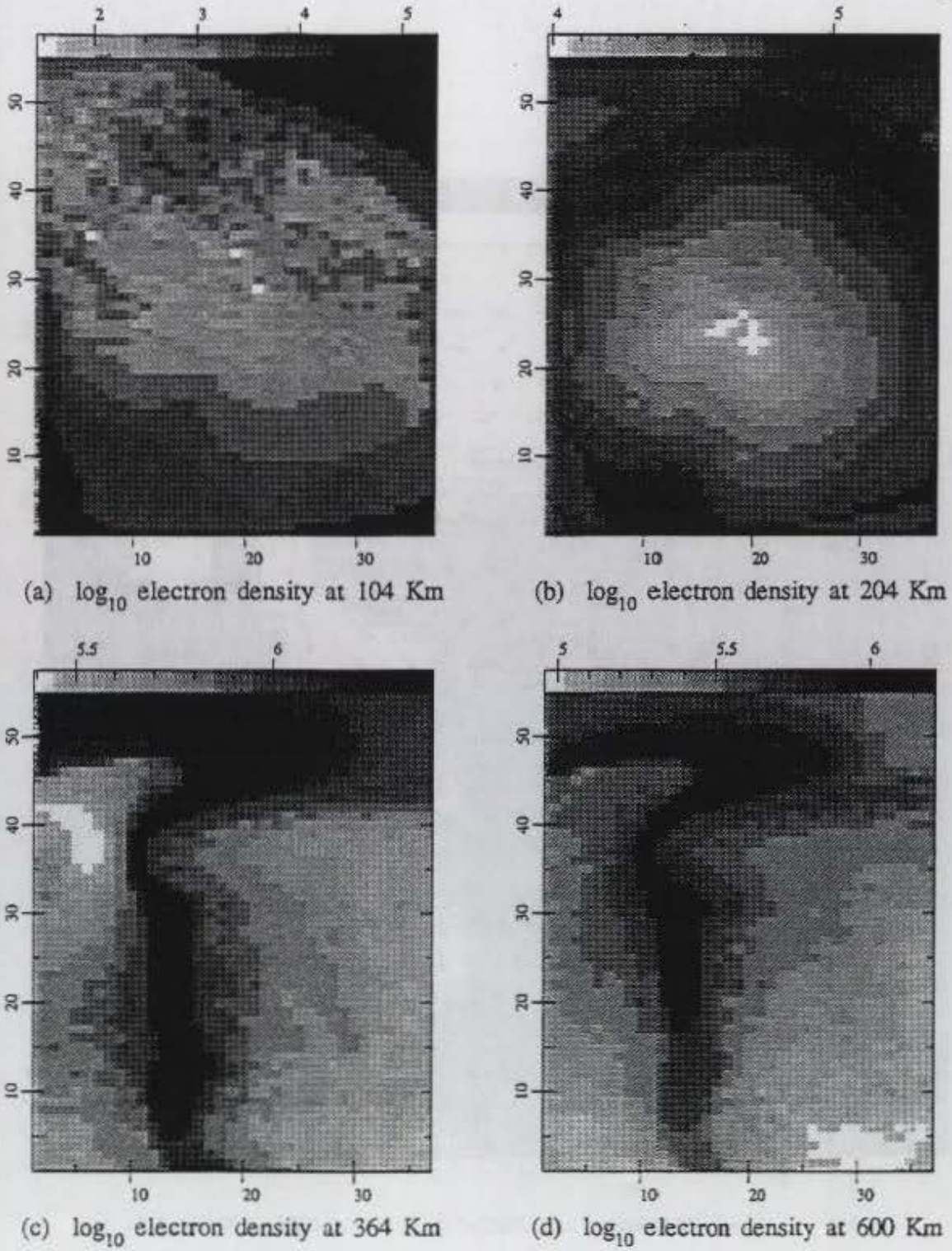

Figure 20. Gray scale plot of the electron density generated by the TDIM model at different altitudes

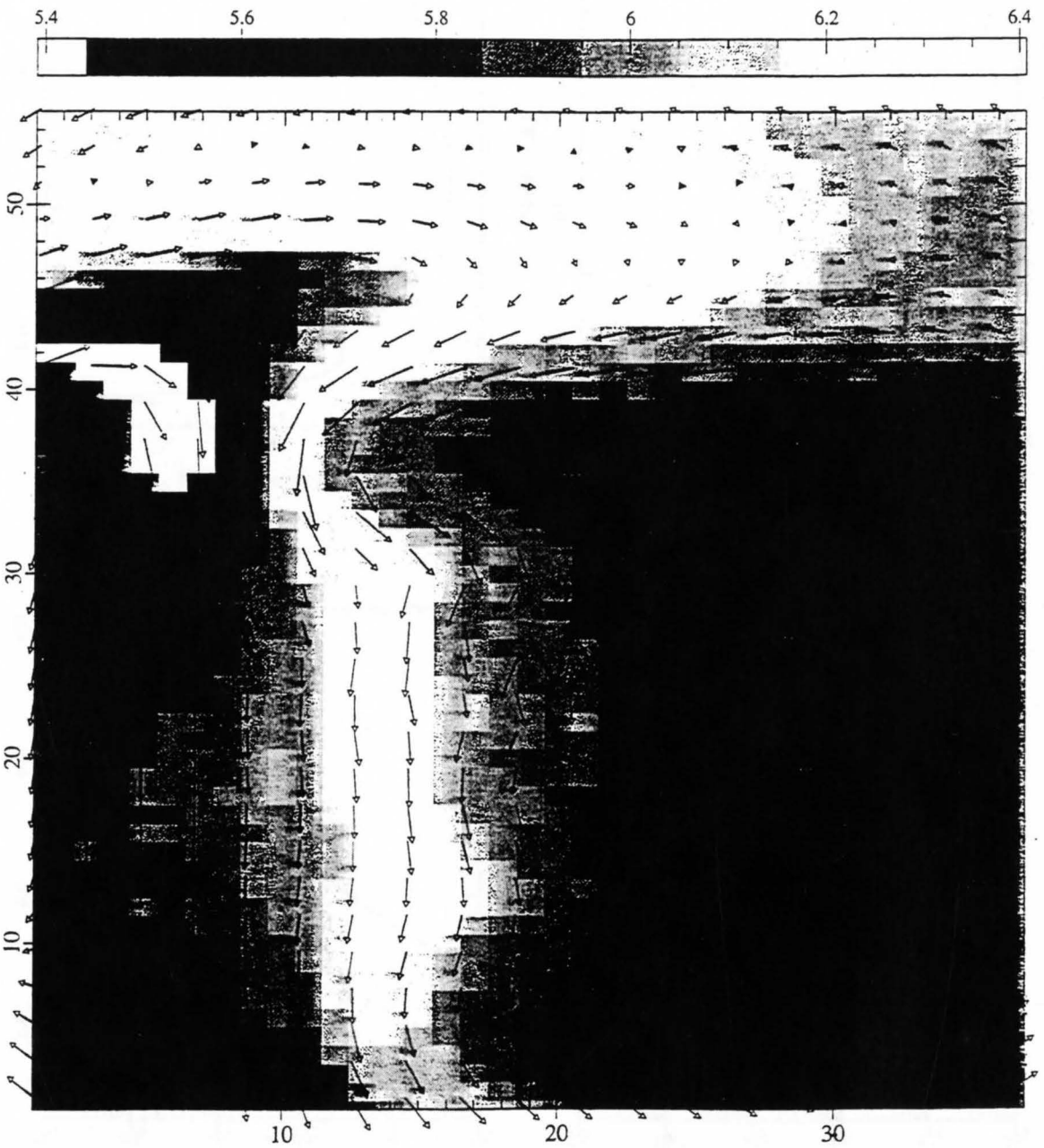

Figure 21. *Heppner-Maynard* convection pattern superimposed on the electron density gradient pattern.

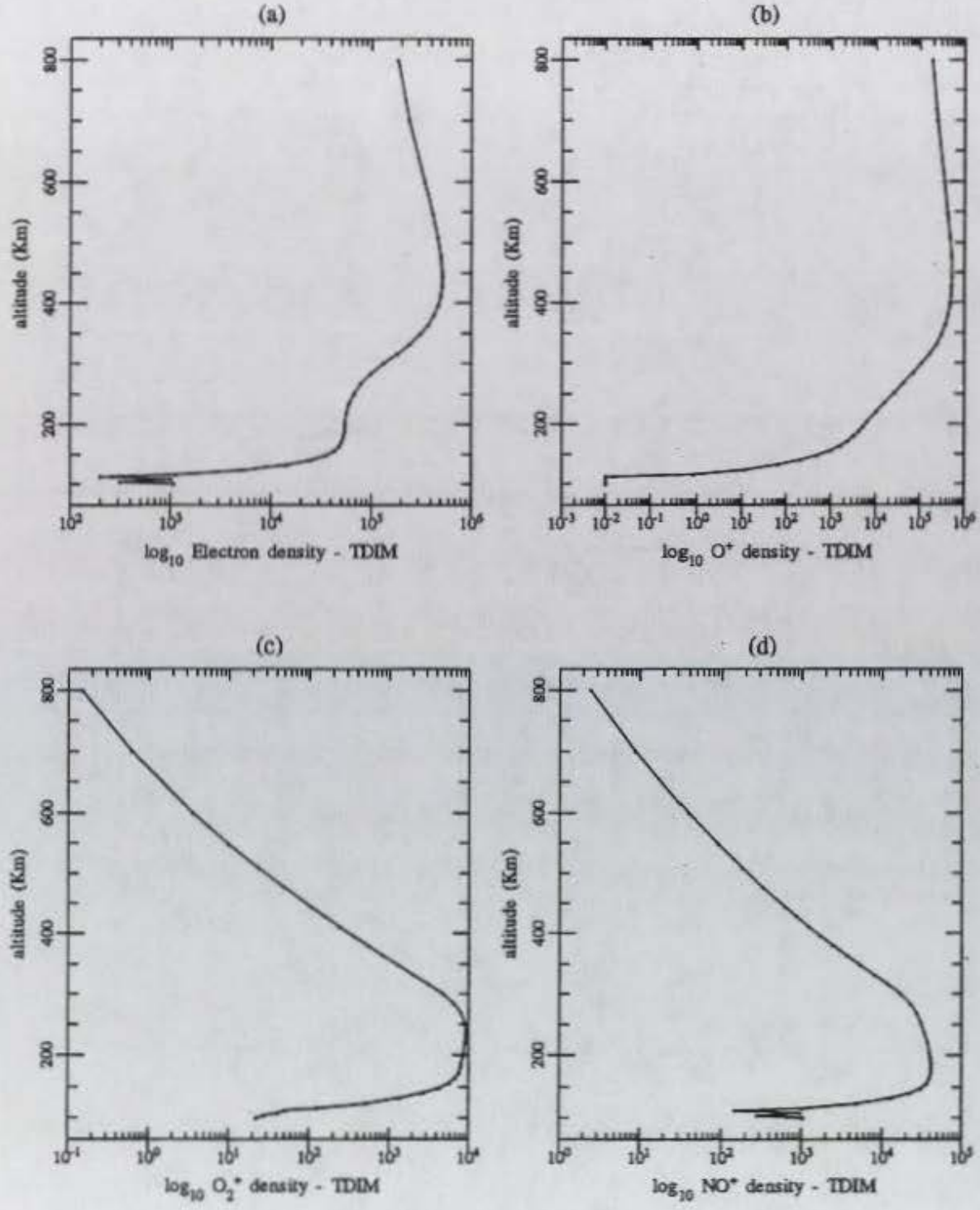

Figure 22. The altitude profile of (a) the density of the electrons and (b)-(d) the various ions generated by the TDIM.

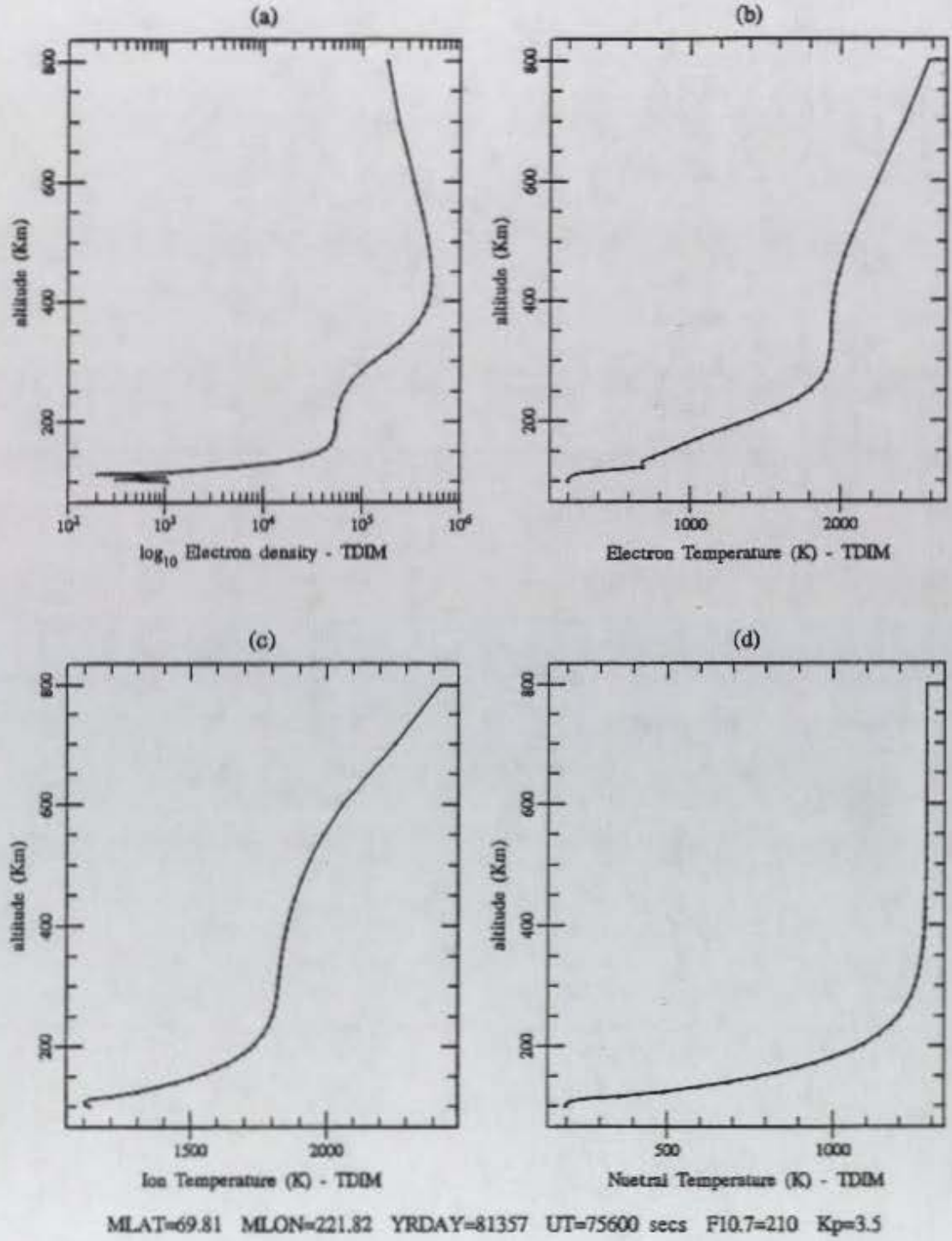

Figure 23. The altitude profile of (a) the density of the electrons and (b)-(d) the various neutrals generated by the TDIM.

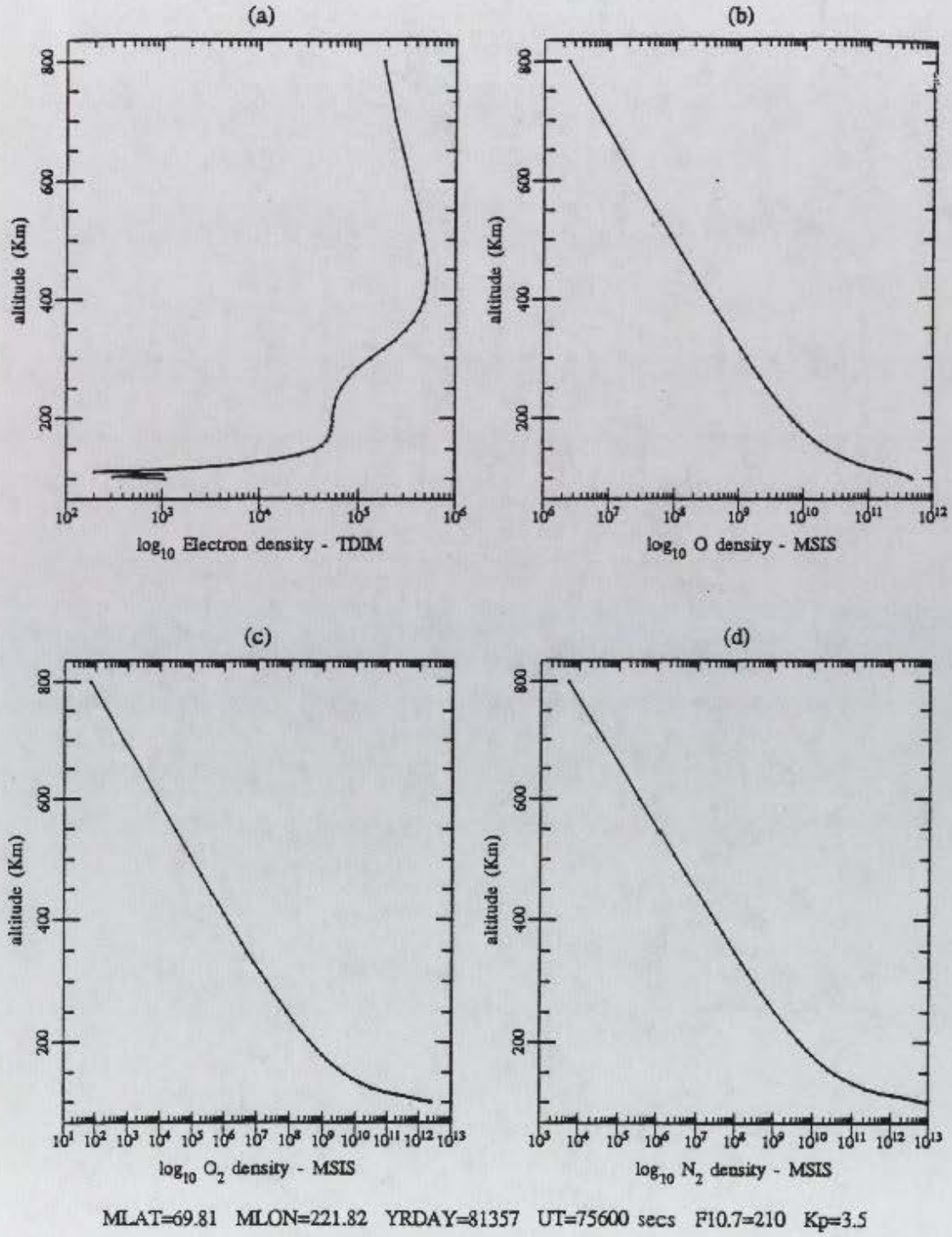

Figure 24. The altitude profile of (a) the density of the electrons and the temperature profile of the (b) electrons, (c) ions, and (d) neutrals generated by the TDIM.

4.3.1. *Basic Assumptions*

1) Quasi-neutrality which implies that electron and ion densities are nearly equal ($n_i \approx n_e$). This assumption is otherwise called the plasma approximation.

2) Electron and ion temperatures are nearly equal ($T_i \approx T_e$). In the F region ionosphere, the source of energy is from ion heating due to frictional effects. Since the TOI is in the dark, there is not much energy influx to preferentially elevate the electron temperature.

3) The gravity term in the momentum equation can be neglected since in the polar regions the magnetic field $\vec{B}$ can be assumed to be parallel to the gravitational acceleration $\vec{g}$.

4) The stress term ($\nabla \cdot \vec{\tau}$) in the momentum equation can be neglected. Stress effects are primarily due to viscosity caused by velocity shears, which are in turn brought about by non-uniform electric fields. In the TOI and the surrounding regions the electric field is mostly uniform.

5) Drop the production and loss terms in the continuity equation. The typical production rate is about 20 minutes, which is long when compared to a typical growth rate times. The loss rate is uniform through out the patch, thus preserving the density gradients.

6) Ignore the effects of the neutral wind.

7) Neglect the effects caused by the coupling of the F region with the magnetosphere and the E region through Pedersen's conductivity along the highly conducting magnetic field lines.

8) Ignore source (seed) mechanisms.

4.3.2. Some Growth Rate Expressions and their Assumptions

The following section lists two important expressions for the growth rate. The first expression is the simple one, which will be used to generate our results. The next one is for a general case. The assumption made in deriving these expressions will also be listed and ratified where possible.

4.3.2.1. Simple One Dimensional Case in the Collisional (Low Altitude) Region

Consider the simple one-dimensional case where the perturbing wave is perpendicular to the magnetic field, i.e., $\bar{k} \cdot \bar{B} = 0$. The physics of this scenario was discussed in detail in section 3.2.1. The following assumptions/simplifications are made. Wherever possible the participating parameters were calculated from the data set to validate the assumptions. Appendix A discusses the different calculated parameters and their profiles.

1. Local approximation or the short wavelength limit. We assume that $kL >> 1$, where $k \equiv \frac{2\pi}{\lambda}$ is the wave number and,

$$L^{-1} \equiv \frac{1}{n_0}\frac{\partial n}{\partial x} \tag{10}$$

The parameter L is commonly known as the gradient scale length and it is the measure of the distance in which the density changes by a factor of *e* (base of natural logarithm).

The assumption is equivalent to ignoring the influence of the conducting background plasma. The scale size is much larger than the displacement amplitude of the perturbing wave so that the medium does not notice the effects due to the wave. It is as though the background plasma were absent and hence the effects caused by the perturbing wave are not propagated through the medium within the distance bounded by the scale length.

2. The electric field is strictly one dimensional and perpendicular to the density gradient and the magnetic field.

3. $\upsilon_e << \Omega_e$. Figure 25 is the ratio ν_e/Ω_e at different altitude slices. Panel (c) shows that υ_e is about 4 orders of magnitude smaller than Ω_e. Panel (a) in Figure 26 shows the altitude profile at the fixed coordinate (69.8 N, 221.82 E). From these two plots we can conclude that this assumption is valid at all F region altitude

4. $\upsilon_{en} << \upsilon_{ei}$. We can drop terms involving the electron-neutral collision frequency in the momentum term. This can be seen in panel (d) of Figure 26.

Ignore ion-inertial effects. Drop the convective derivative term in the momentum equation since

$$\frac{\partial}{\partial t} + u_i \cdot \nabla << \upsilon_{in}$$

What this means is that the ion collision frequency is so high that the fluid element hardly moves. We can consider it to be nearly stationary and hence work in this stationary frame of reference rather than work in a moving frame of reference. This assumption is **only valid** at low altitudes where collision dominates

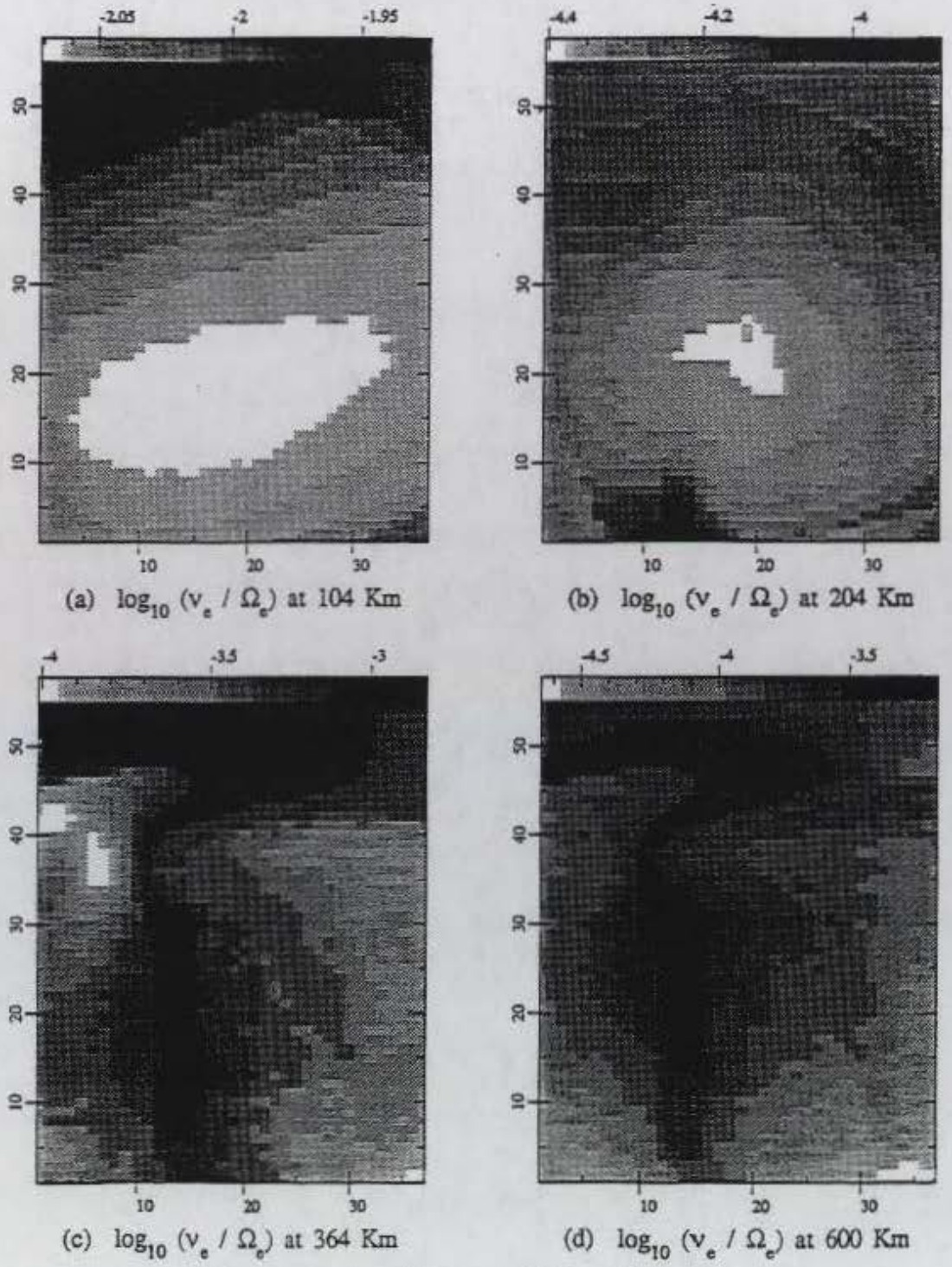

Figure 25. Ratio of electron collision to gyro frequency at different altitude slices.

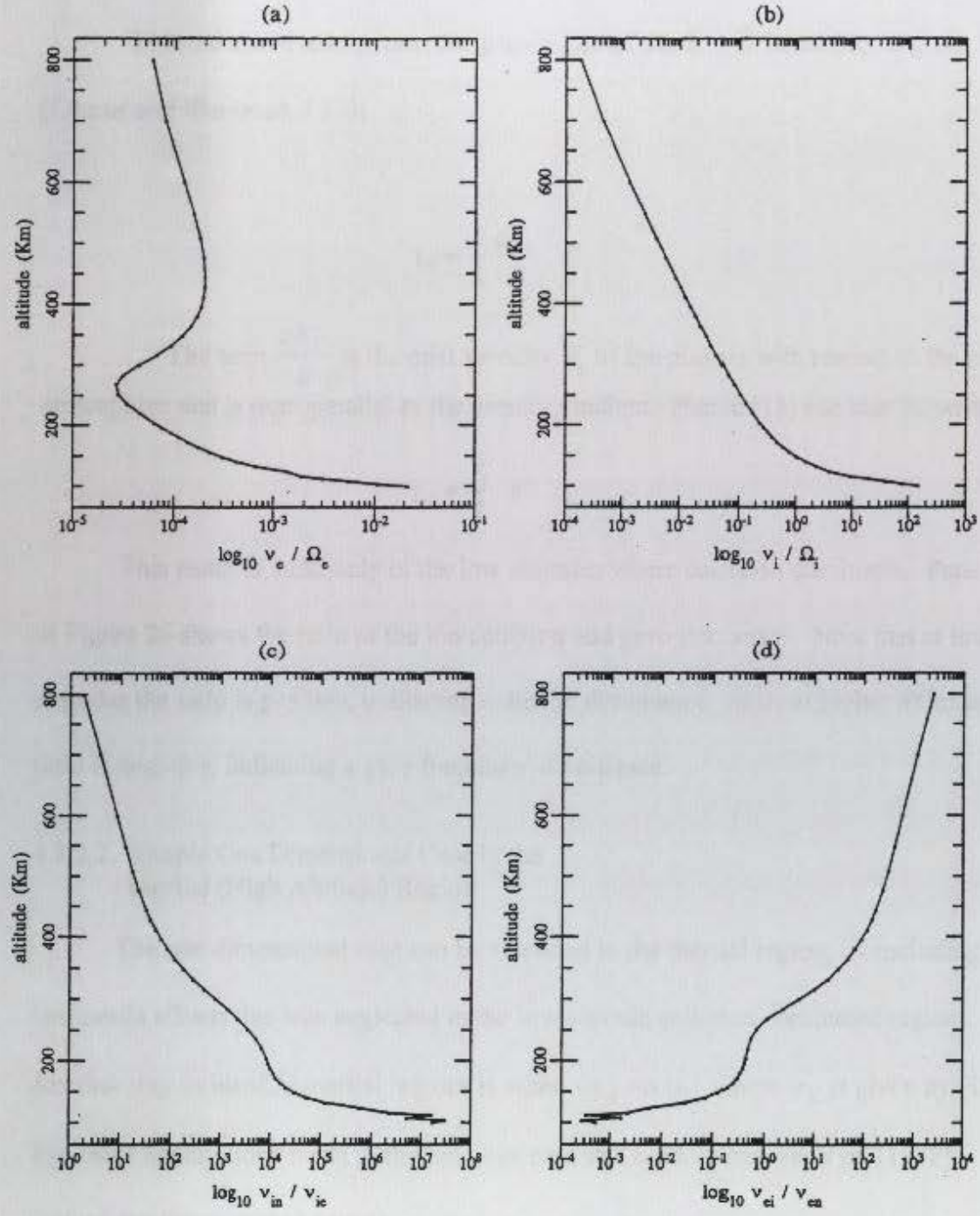

Figure 26. Altitude profiles of the ratios; (a) electron collision to gyro frequency, (b) ion collision to gyro frequency, (c) ion-neutral to ion-electron collision frequency, and (d) electron-ion to electron-neutral collision frequency.

$(\upsilon_i >> \Omega_i)$.

With the above assumption the growth rate of the $\vec{E} \times \vec{B}$ instability is given by [*Linson and Workman*, 1970]

$$\gamma_0 = \frac{1}{L}\frac{cE_\perp}{B} \quad s^{-1} \tag{11}$$

The term $\frac{cE_\perp}{B}$ is the drift velocity $V_\parallel$ of the plasma with respect to the neutral atmosphere and is (anti)parallel to the density gradient. Hence (11) can also be written as

$$\gamma_0 = \frac{V_\parallel}{L} \quad s^{-1} \tag{12}$$

This result is valid only in the low altitudes where collision dominates. Panel (b) of Figure 26 shows the ratio of the ion collision and gyro frequency. Note that at lower altitudes the ratio is positive, indicating collision dominance, while at higher altitudes the ratio is negative, indicating a gyro frequency dominance.

4.3.2.2. Simple One Dimensional Case in the Inertial (High Altitude) Region

The one dimensional case can be extended to the inertial region, by including the ion-inertia effects that was neglected in the low altitude collision dominated region. Another way to identify inertial regions is when $4\gamma_0 >> \upsilon_{in}$ where γ_0 is given by (10). The other assumptions made in the previous case still hold. *Ossakow et al.* [1978] derived the linear growth rate as

$$\gamma = \left(\frac{\upsilon_{in}}{L}\frac{cE_{\perp}}{B}\right)^{1/2} \quad s^{-1} \tag{13}$$

This can other wise be written as $\gamma = (\gamma_0 \upsilon_{in})^{1/2}$ where γ_0 is given by (10).

4.3.2.3. General Expression for the Growth Rate in Two Dimensions

Keskinen and Ossakow [1982] developed an expression for the growth rate where the electric field is homogeneous in two dimensions and the perturbing wave is three dimensional. In their geometry (Figure 27), the positive y axis was along the positive density gradient and the positive z axis was along the magnetic field. The electric field was in the x-y plane and had the form $\vec{E} = E\cos\beta\hat{x} + E\sin\beta\hat{y}$ and the perturbing wave vector had the form $\vec{k} = k_{\perp}\cos\beta\hat{x} + k_{\perp}\sin\beta\hat{y} + k_{\parallel}\hat{z}$.

Their growth rate is given by

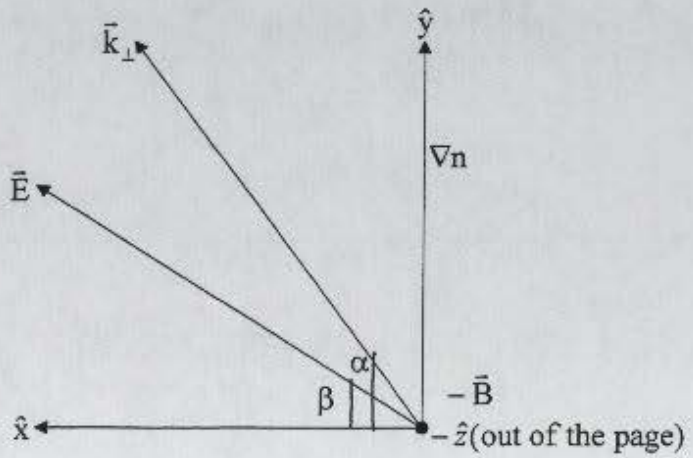

Figure 27. Geometry used in developing the growth rate equation (12).

$$\gamma = \frac{-\cos\alpha \frac{\upsilon_{ei}}{\Omega_e L}\left(\frac{\upsilon_{in}}{\Omega_i}\frac{cE}{B}\cos(\alpha-\beta)-\frac{k_\parallel}{k_\perp}U_d\right)}{\left(\frac{k_\parallel}{k_\perp}\right)^2+\frac{\upsilon_{in}}{\Omega_i}\frac{\upsilon_{ei}}{\Omega_e}} - D_\perp k_\perp^2 - D_\parallel k_\parallel^2 \ s^{-1} \qquad (14)$$

where the diffusion coefficients ($D_\perp$ and $D_\parallel$) are

$$D_\perp = \frac{c_s^2}{\Omega_i}\frac{\upsilon_{ei}}{\Omega_e}$$

$$D_\parallel = \frac{c_s^2}{\upsilon_{in}}\left[1+\left(\frac{(\upsilon_{in}\Omega_i)^2}{\frac{\upsilon_{in}}{\Omega_i}\frac{\upsilon_{ei}}{\Omega_e}+\left(\frac{k_\perp}{k_\parallel}\right)^2}\right)\right]$$

and

$$k_\perp^2 = k_x^2 + k_y^2,\ k_\perp^2 >> k_\parallel^2$$

Using (14) in the growth rate calculation would be very cumbersome though it would give more accurate values than (11) or (13). However, by aligning the vectors obtained from the TDIM model (explained in the next section) and filtering the data we can reduce (14) to the form (11) and (13).

4.3.3. *Method Followed in Calculating the Growth Rate*

As shown in Figure 4.2. the simulation region is a rectangular region draped over the polar cap. The two-dimensional grid system adopted has the x axis ranging from 0 to

37 and the y axis ranging from 0 to 55 giving a total of 2035 grid points corresponding to 2035 bins giving a total region of 37×50 km $\times$ 55×70 km. The model data were generated in the spherical polar coordinate system with θ as the longitude and φ as the latitude. These data have to now be transformed to the rectangular grid system to find the density gradient at particular point.

Figure 28 shows the grid system with the latitude rings superimposed. It also shows three density points and we want to find the density gradient at the point 0 where the density is "n_0". The expression for the gradient in the spherical coordinate system is given by (with constant radius and assuming $\sin\theta$ for large θ to be approximately 1)

$$\nabla n = \frac{1}{r}\frac{\partial n}{\partial \theta}\hat{\theta} + \frac{1}{r\sin\theta}\frac{\partial n}{\partial \varphi}\hat{\varphi} \tag{15}$$

Since it is possible to find the density difference between adjacent points in the grid, the gradient across points 0 and 1 is

$$\nabla n \cdot ds_1 \approx \Delta n_1 = \frac{\partial n}{\partial \theta}\Delta\theta_1 + \frac{\partial n}{\partial \varphi}\Delta\varphi_1 \tag{16}$$

where $\vec{ds_1} = rd\theta + r\sin\theta d\varphi$, and can be calculated from the data set using

$$n_1 - n_0 = \frac{\partial n}{\partial \theta}(\theta_1 - \theta_0) + \frac{\partial n}{\partial \varphi}(\varphi_1 - \varphi_0) \tag{17}$$

Similarly the gradient across points 0 and 2 is

$$n_2 - n_0 = \frac{\partial n}{\partial \theta}(\theta_2 - \theta_0) + \frac{\partial n}{\partial \varphi}(\varphi_2 - \varphi_0) \tag{18}$$

Solving (17) and (18) we get

$$\frac{1}{r}\frac{\partial n}{\partial \theta} = \frac{1}{r}\frac{\Delta n_1 \Delta \varphi_2 - \Delta n_2 \Delta \varphi_1}{\Delta \varphi_1 \Delta \theta_2 - \Delta \varphi_2 \Delta \theta_1} = n'_\theta \tag{19}$$

$$\frac{1}{r\sin\theta}\frac{\partial n}{\partial \varphi} = \frac{1}{r\sin\theta}\frac{\Delta n_1 \Delta \theta_2 - \Delta n_2 \Delta \theta_1}{\Delta \varphi_1 \Delta \theta_2 - \Delta \varphi_2 \Delta \theta_1} = n'_\varphi \tag{20}$$

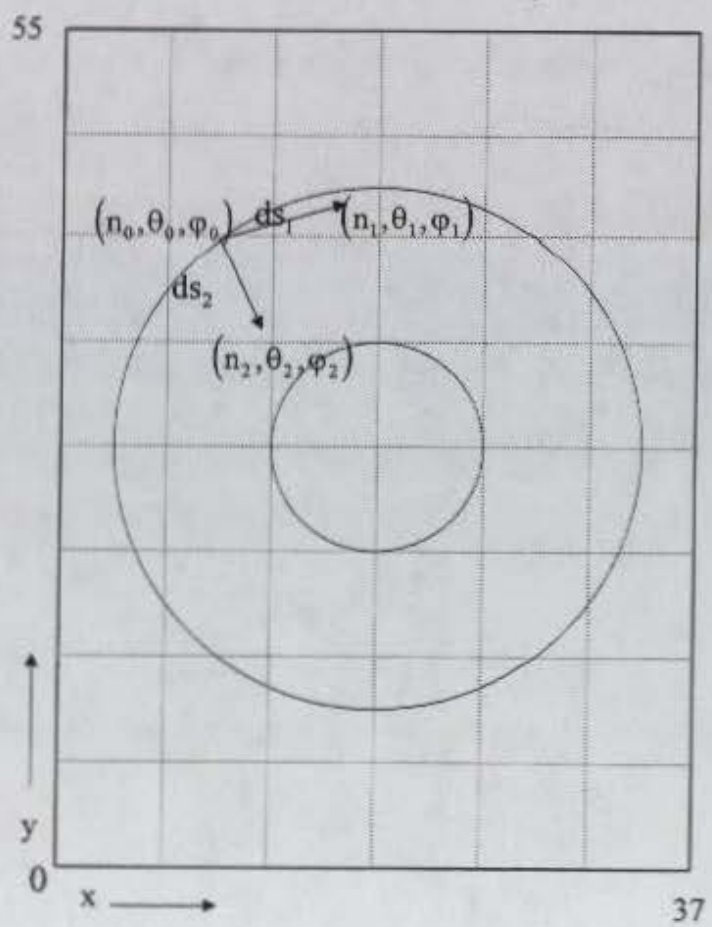

Figure 28. Grid system showing the three density points.

Using (19) and (20) in (15) we can find the density gradient at point 0. This can be repeated at each grid point to find the density gradient at that point in the spherical coordinate system.

The electric fields E_θ and E_φ can be used in the following expression

$$\vec{V} = \frac{c\vec{E} \times \vec{B}}{B^2} \tag{21}$$

to find the convection (drift) velocity at a grid point. Specifically if E_θ and E_φ are the electric field components at a grid point, then the drift velocity components in a spherical coordinate system (up to a sign) is given by $V_\theta = \frac{cE_\varphi}{B}$ and $V_\varphi = \frac{cE_\theta}{B}$.

For ease in plotting the gradient and convection vectors and to follow a consistent coordinate system, let us transform the gradient and drift velocity vector components originally in the spherical coordinate system to the rectangular grid coordinate system. We can do this by using a rotation transformation matrix. If φ is the longitude of the point where the vector field components in the spherical system are P_θ and P_φ, then the matrix operation to find the components P_x and P_y is

$$\begin{pmatrix} P_x \\ P_y \end{pmatrix} = \begin{pmatrix} \cos\varphi & \sin\varphi \\ -\sin\varphi & \cos\varphi \end{pmatrix} \begin{pmatrix} P_\varphi \\ P_\theta \end{pmatrix} \tag{22}$$

Equation (22) was used in generating the plots (Figure 21) showing the *Heppner-Maynard* convection pattern and any vector plots presented further. The next step is to

find the resultant gradient and the drift vector in our grid system using the familiar expressions

$$P = \left(P_x^2 + P_y^2\right)^{1/2}$$
$$\tan\beta = \frac{P_y}{P_x} \tag{23}$$

We now have the density gradient vector and the drift velocity vector. The magnitude of the density gradient vector can be used in equation (10) to find the scale length at a grid point. We can calculate the component of the drift velocity vector that is parallel/anti-parallel to the density gradient vector and use this in equation (12) to find the growth rate. Note that by finding the parallel component of the drift velocity (together with the assumption of the perturbing wave being one dimensional) we are reducing the two-dimensional equation (14) to a simple one-dimensional case of equation (11). Finally, we select only those points where the drift velocity component is parallel to the density gradient (leading to an unstable situation) and discard the points where it is anti-parallel to the density gradient (leading to a stable situation).

The next chapter implements this procedure to find the scale lengths and the growth rate for the data sets 1 and 2.

CHAPTER 5

RESULTS AND DISCUSSION

5.1. Results from Data Set 1

As described in section 4.2, data set 1 gives the species densities, temperature and the convection velocity, in the simulation region (see Figure 19) for the 2035 bins or data points. The TOI was simulated for moderate geomagnetic activity ($K_p = 3.5$) and solar maximum ($F_{10.7} = 210$) on the 357th day of 1981 (northern winter) at 2100 UT. The data from the TDIM model were processed along the procedure outlined in the previous chapter (see section 4.2), and the scale lengths and the growth rates were obtained. The various other parameters needed to find the growth rates, like the collision frequencies, gyro radii, etc., were calculated from expressions listed in Appendix A. Though the various parameters from the TDIM model were available for all altitudes, the parameters at an altitude of 364 kilometers, where the TOI is strong, were used to calculate the scale length and the growth time. Note that on the plots presented below the numbers on the axes are just the indices of the bins and have no significance apart from the fact that the distance between any two grid points is approximately 70 kilometers. The rectangular regions, however, correspond to our region of interest shown in Figure 19. The terminator is along the line parallel to the horizontal axes on the grid point 28 of the vertical axes.

Figure 29 shows the density gradient vectors superimposed on the electron density plot. The length of the vectors corresponds to the magnitude of the gradient--the longer a

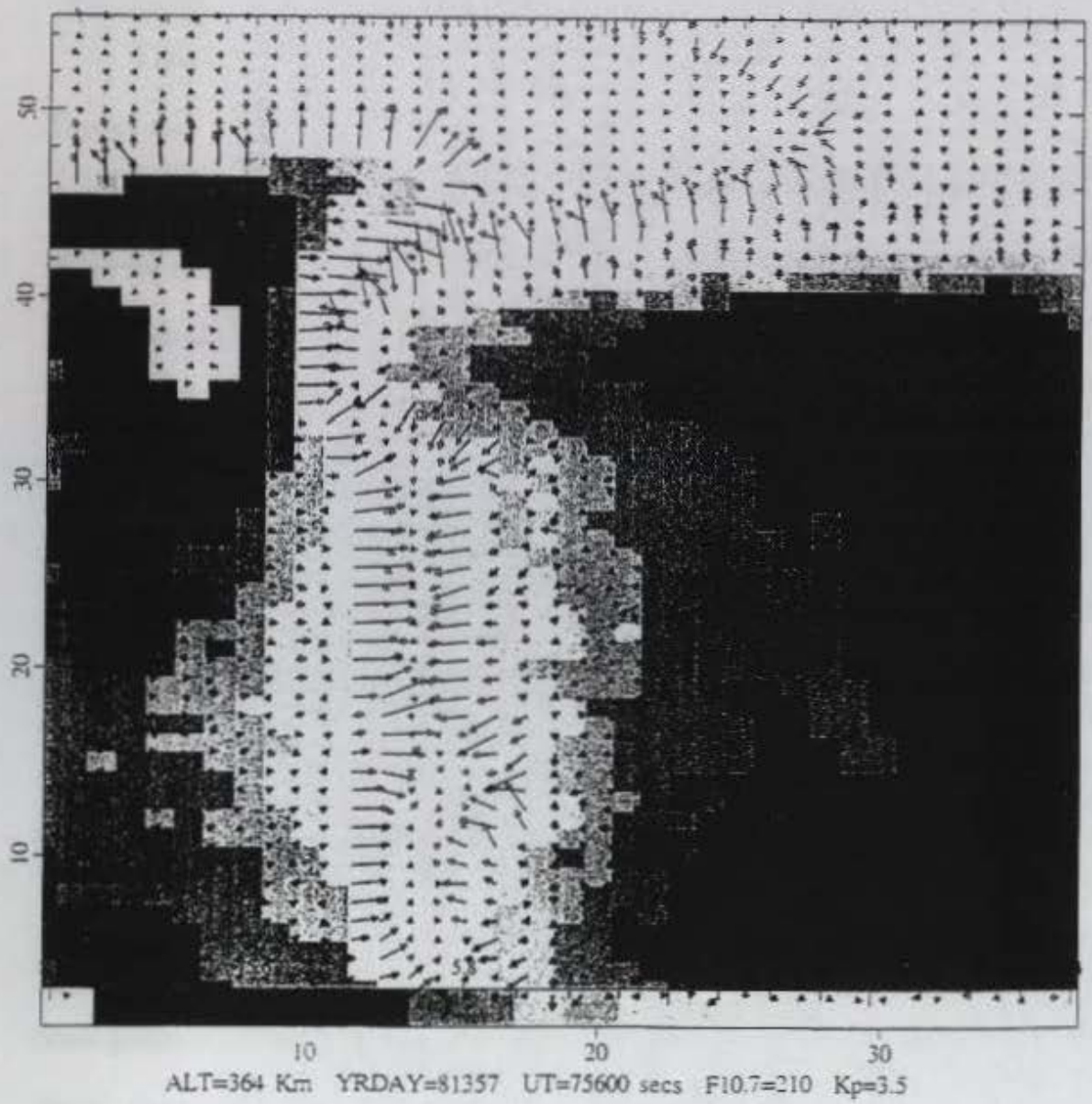

Figure 29. Density gradient vectors superimposed on the electron density pattern for data set 1.

vector, the steeper is the density gradient. We can clearly see steep density gradients along the edges of the TOI. Figure 30 shows the convection vectors (wider arrow head) along with the density gradient vectors. This figure illustrates the relative orientation of the two vectors and also enables us to identify unstable grid points. We will use this figure in an illustration later.

Figure 31 is a gray-scale plot of the density gradient scale length (in kilometers). Though each grid point has an associated scale length, the plot only shows scale lengths that fall below a certain value called the "cutoff." Grid points having a scale length value above the cutoff were omitted from the plot. For instance, panel (d) shows the scale lengths below a value of 250 kilometers. Panel (a) shows gradient scale length, with a 100-kilometers cutoff. We see scale sizes ranging from about 40 kilometers to 100 kilometers along the left edge of the TOI. The dayside is towards the top of the panel and the TOI convects towards the bottom of the panel. Note that unlike a patch the TOI is not detached and hence we cannot identify a trailing edge. We can also see about 80-kilometer scale lengths develop along the throat region around the coordinates (5, 45). Panel (b) shows scale lengths for a cutoff of 200 kilometers. We can see that more bins have developed scale lengths and most of them are below 100 kilometers or a little above. More strong gradients develop near the throat region and all along the left hand side. The next two panels, (c) and (d), are for cutoffs of 300 and 400 kilometers, respectively. More gradients are seen with the gradients around 100 kilometers on the left and near the throat. Gradients also develop along the right edge of the TOI, but steeper gradients occur mostly on the left edge of the TOI.

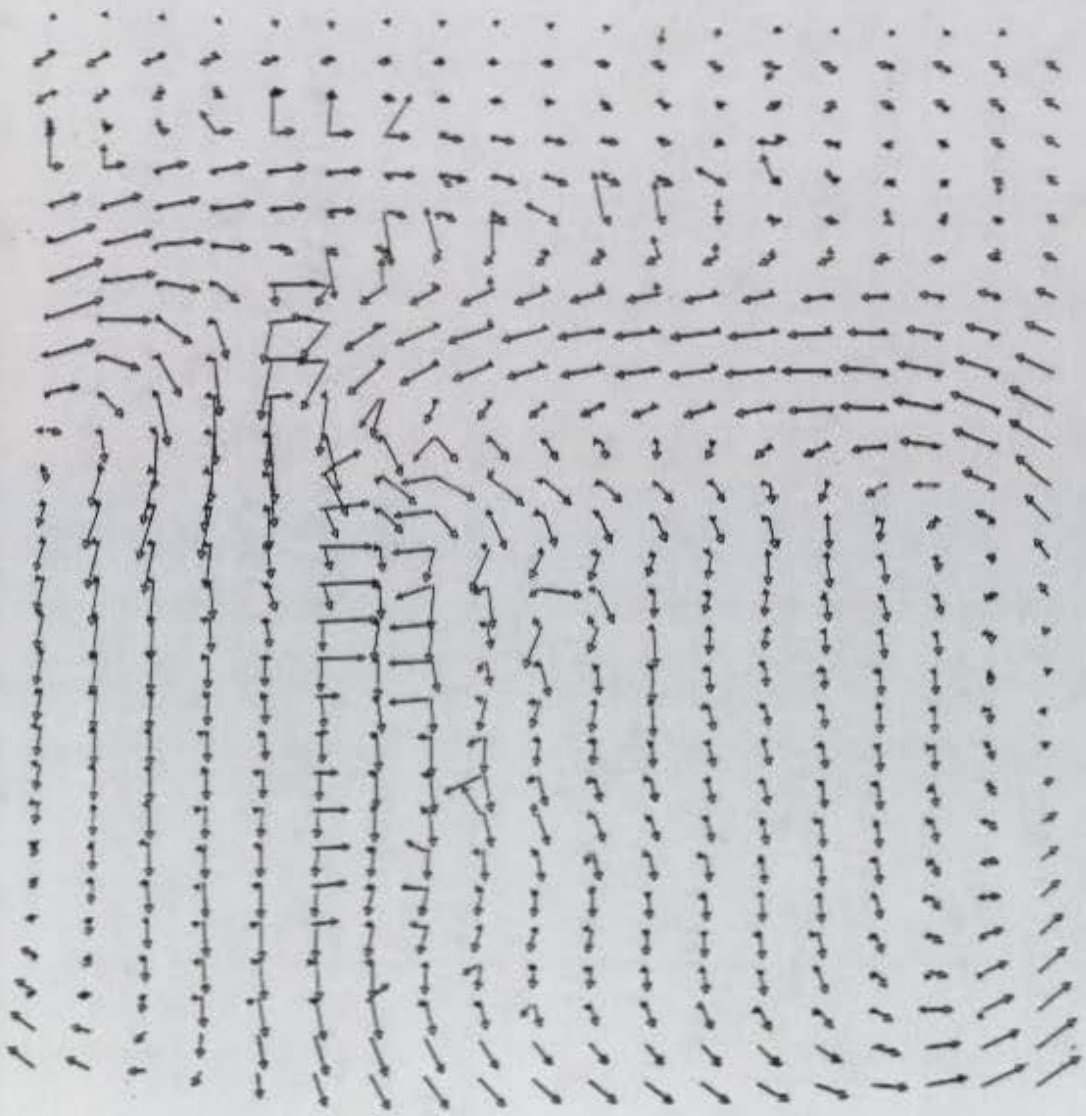

Figure 30.. Convection (wider arrow heads) and density gradient vectors for data set 1.

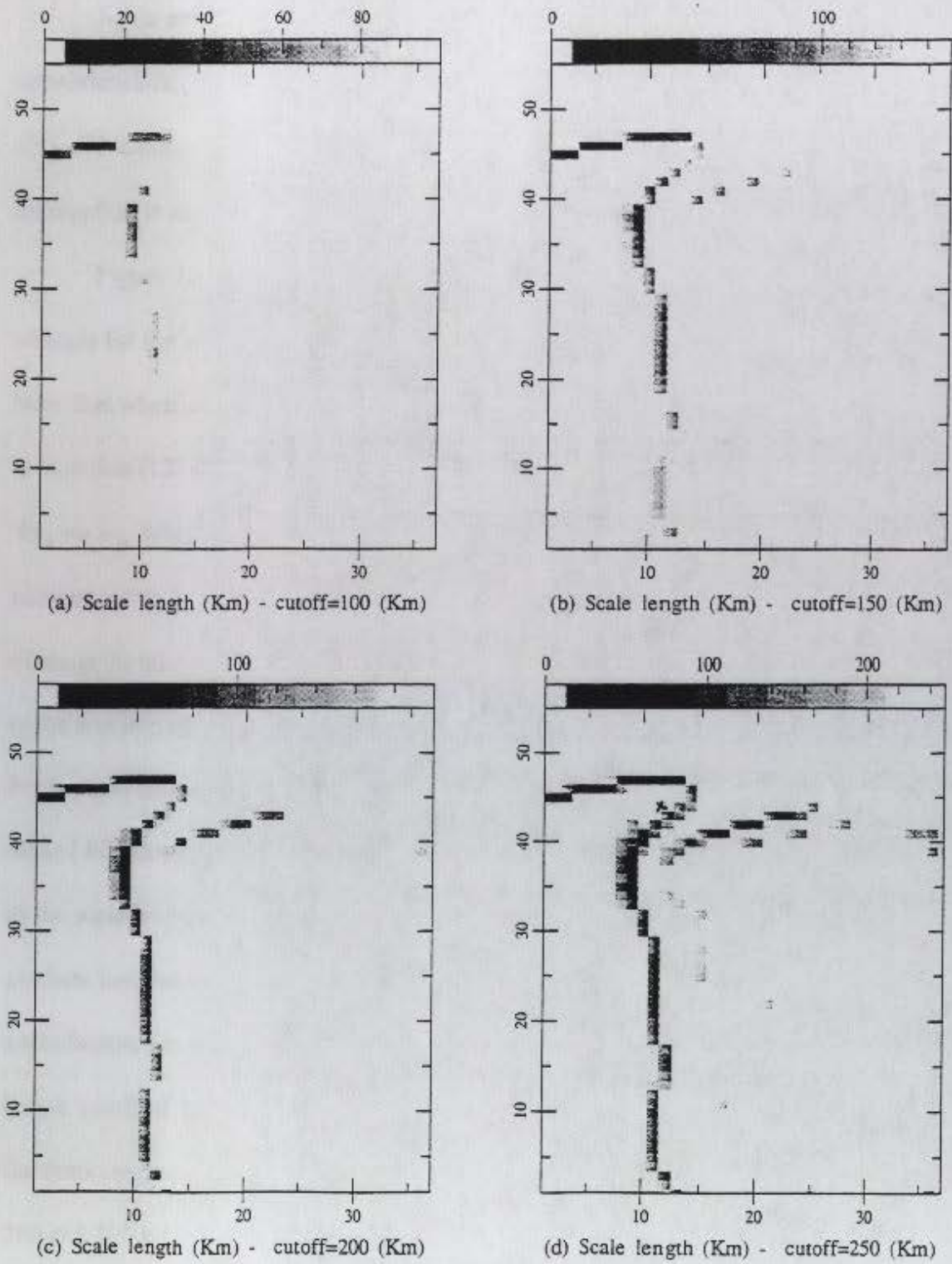

Figure 31. Gray-scale plot of the density gradient scale length in kilometers for various cutoffs.

As an aside, recall that in the previous chapter we have assumed the local approximation (kL >> 1) in choosing our growth rate expressions. For a scale length, L about 70 kilometers and a perturbing wave in the order of meters to kilometers, this assumption is satisfied.

Figure 32 shows a gray scale plot of the growth time (inverse of growth rate) in seconds for the scale lengths of Figure 31. The cutoffs are the same as in Figure 31. Note that when calculating the growth rate we initially use equation (11) and then switch to equation (13) on reaching the inertial domain in the high altitudes, when the condition $4\gamma_0 >> \upsilon_{in}$ where γ_0 is given by (10), is met within two orders of magnitude. A ballpark estimate with typical convection speeds of about 700 m/s and with a scale length of about 70 kilometers gives us a growth time (using Equation (11)) of about 100 seconds in the noninertial regime. Let us see how our actual results compare with this value. From panel (a) we see a growth time of about 60 to 90 seconds for scale lengths between 60 and 80 kilometers, which agrees with our estimate. Note that some bins which occur in the scale length plot are missing in the growth time plot. This is because the density gradient and the convection vectors are oriented in such a way so as to damp the perturbation, i.e. the missing bins are stable. Panel (b) shows the growth time for a scale length cutoff of 150 kilometers. More unstable regions develop along the left edge and the throat region of the TOI. Panels (c) and (d) show more unstable regions at cutoffs of 200 and 250 kilometers, respectively. Notice that as we go to higher cutoffs, we get more unstable regions develop, mostly along the edges of the TOI. The growth time is predominantly below 3 minutes.

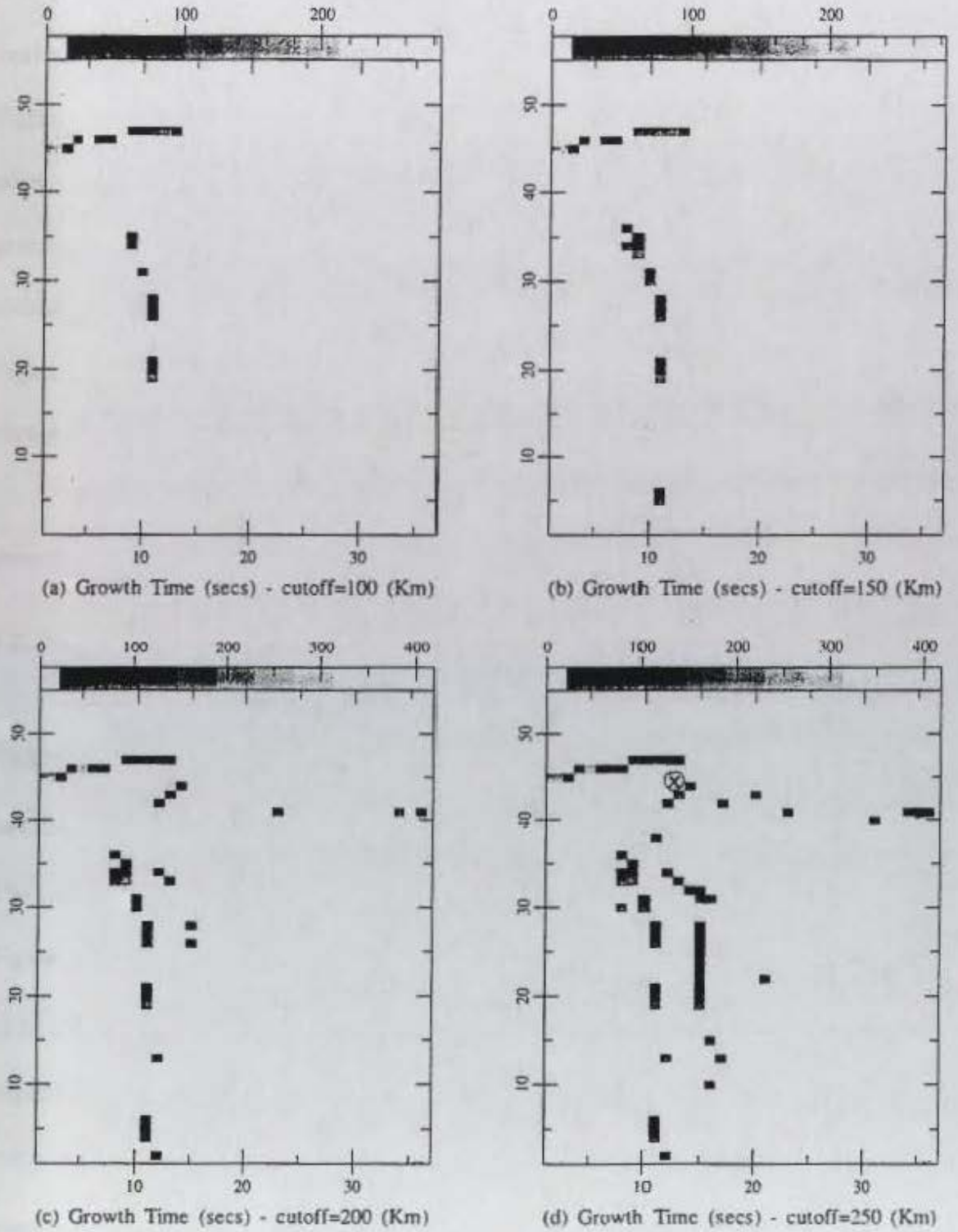

Figure 32. Growth time in seconds for the scale lengths of Figure 31.

Let us now follow an illustration to identify an unstable bin. Consider the bin marked by an "X" (near bin [14,45]) in Figure 29. It has a steep density gradient. In Figure 30 the point marked by "X" shows the gradient and the convection vectors at this point. We can see that the convection vector has a parallel component to the density gradient and hence should be unstable. In Figure 32 (d), the "X" identifies this point as indeed unstable. The corresponding scale length is marked in Figure 33. So any point in Figure 30 here the convection vector has a parallel component to the density gradient vector will be unstable.

Results from data set 1, serve as an illustration of the procedure to calculate the growth time and also to understand the various plots presented to visualize our results.

5.2. Results from Data Set 2

Data set 2 consists of a sequence of snapshots of the TOI, starting from 2115 UT (76500 secs) for every 5 minutes (300 secs) until 2200 UT (79200 secs). Every snapshot had the same K_p, $F_{10.7}$ and date as data set 1. However the IMF B_y pattern was varied. The variations used by the USU TDIM model to generate the snapshots are shown in Figure 33. From the figure we see that B_y was maintained weakly negative till about 2120 UT (76800 secs). It is then made strongly negative and is finally reversed from negative to positive value at about 2140 UT (78000 secs). Figure 34 shows the convection velocity pattern (*Heppner-Maynard* "A") at 2115 UT where B_y is weakly negative, Figure 35 shows the pattern (*Heppner-Maynard* "DE") when B_y is strongly negative at 2140 UT, and Figure 36 shows the convection pattern (*Heppner-Maynard*

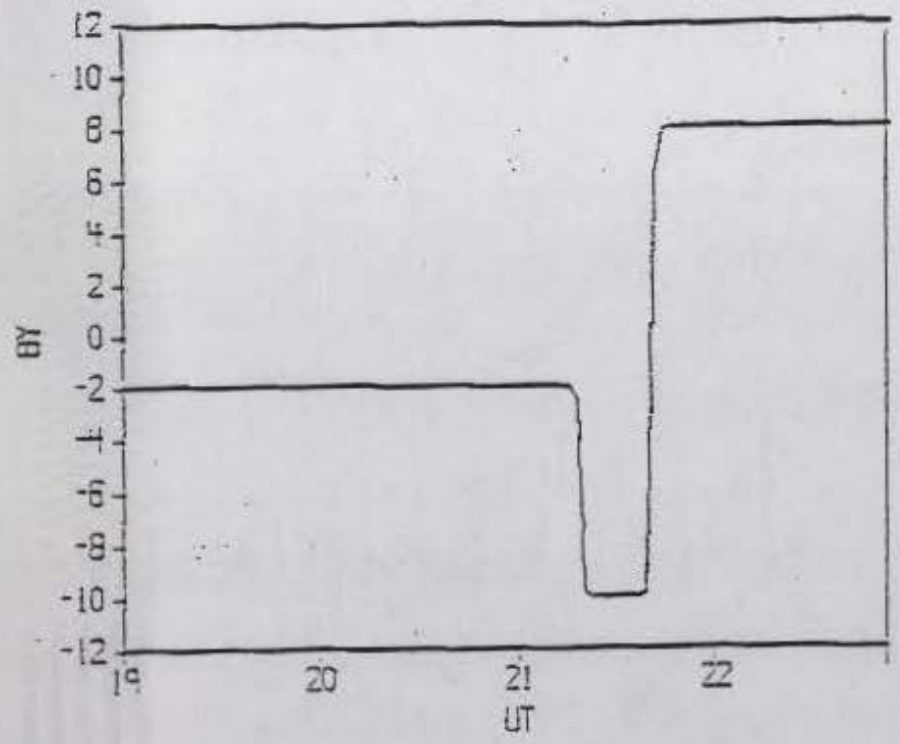

Figure 33. B_y variations used by the USU TDIM model to generate data set 2.

"BC") after it is reversed from a negative to a positive value at 2145 UT. The panels in Figures 37, 38, and 39 show the electron density snapshots at different times. As the UT advances, we see the TOI slowly distorts in response to the changing convection pattern. We will henceforth refer to the UT in seconds, to maintain consistency in our discussion.

The data of each snapshot were processed as described in the previous section. The various parameters were calculated, the unstable bins identified, and the growth time for the unstable bins was calculated. In addition, the change in growth rate for each bin as it moves in time was also found. Note that to do this we needed the successive grid positions of a particular bin as it convects across the polar cap from 76500 UT to 79200 UT. Only the grid points that stayed within the region of interest over the period of the

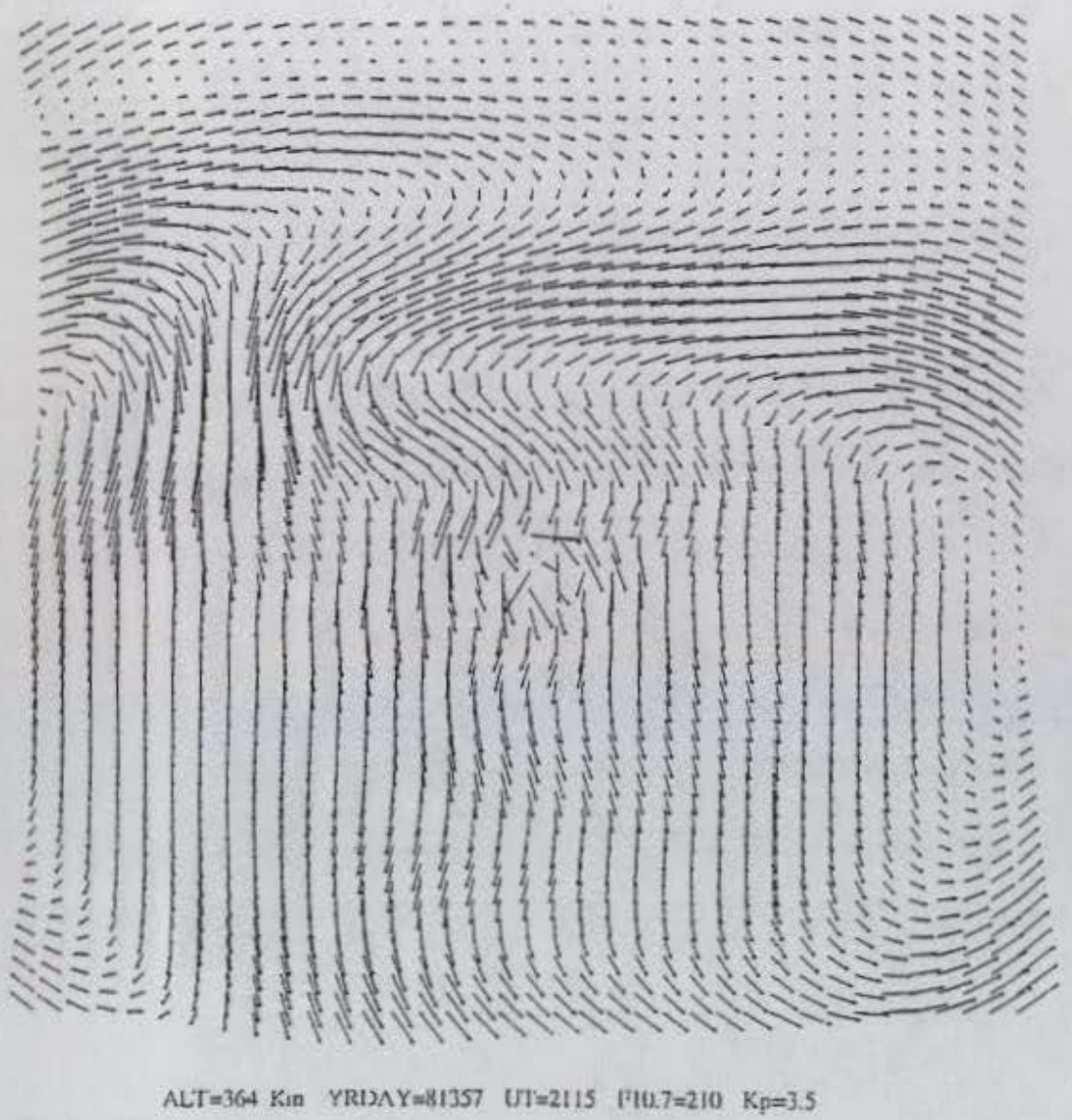

Figure 34. *Heppner-Maynard* "A" convection pattern.

simulation were retained for further analysis. Furthermore, only those grid points that were unstable at 79200 UT were retained. This filtration was essential to focus our analysis and to keep the amount of data manageable. We finally ended up with 88 bin locations spread throughout the TOI. We then selected five characteristic bins that

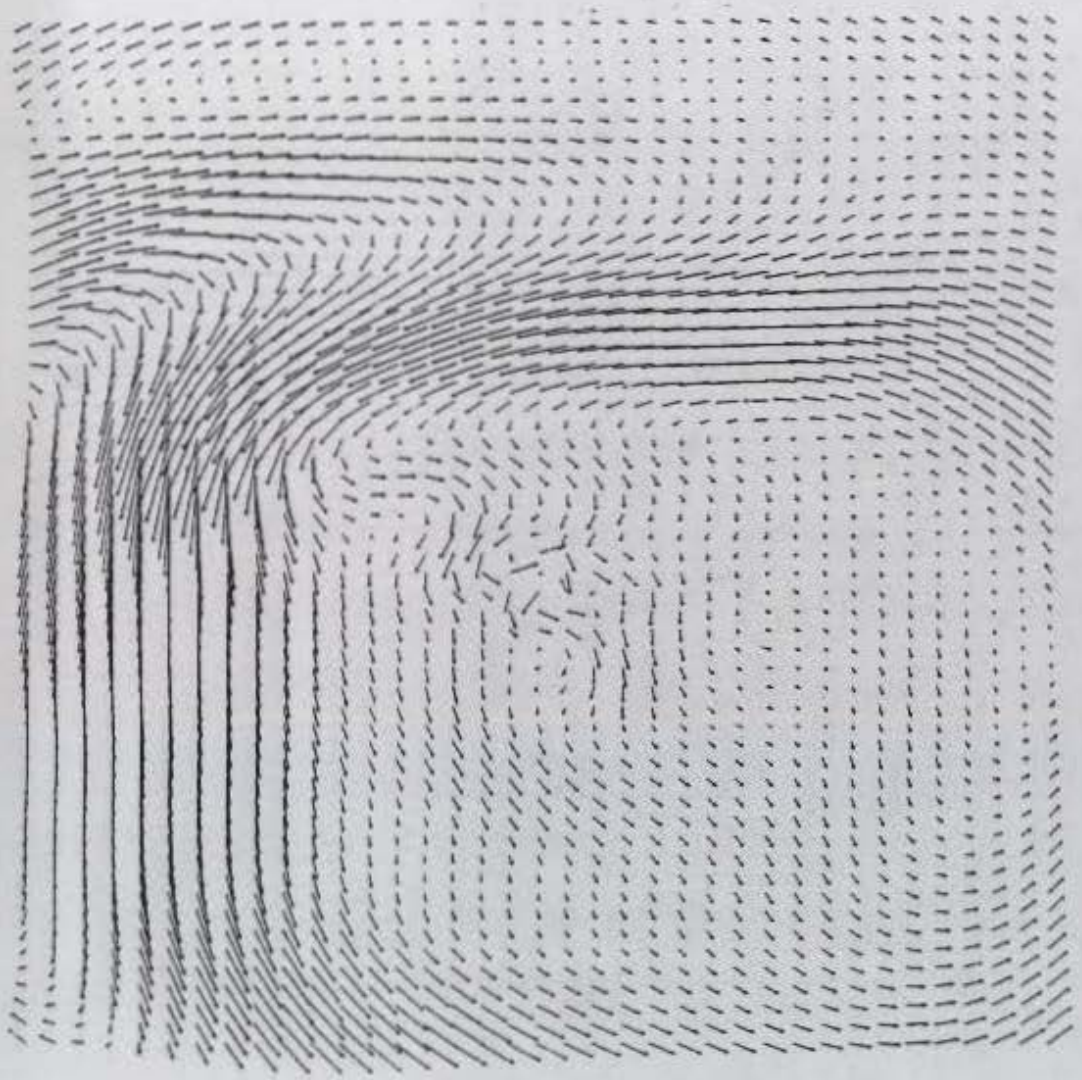

Figure 35. *Heppner-Maynard* "DE" convection pattern.

illustrated, though not exhaustively, the different scenarios traced by the growth time of a bin with UT. The position of the grid point in the TOI was also a consideration in choosing the example bins. The results and analysis of these bins follow.

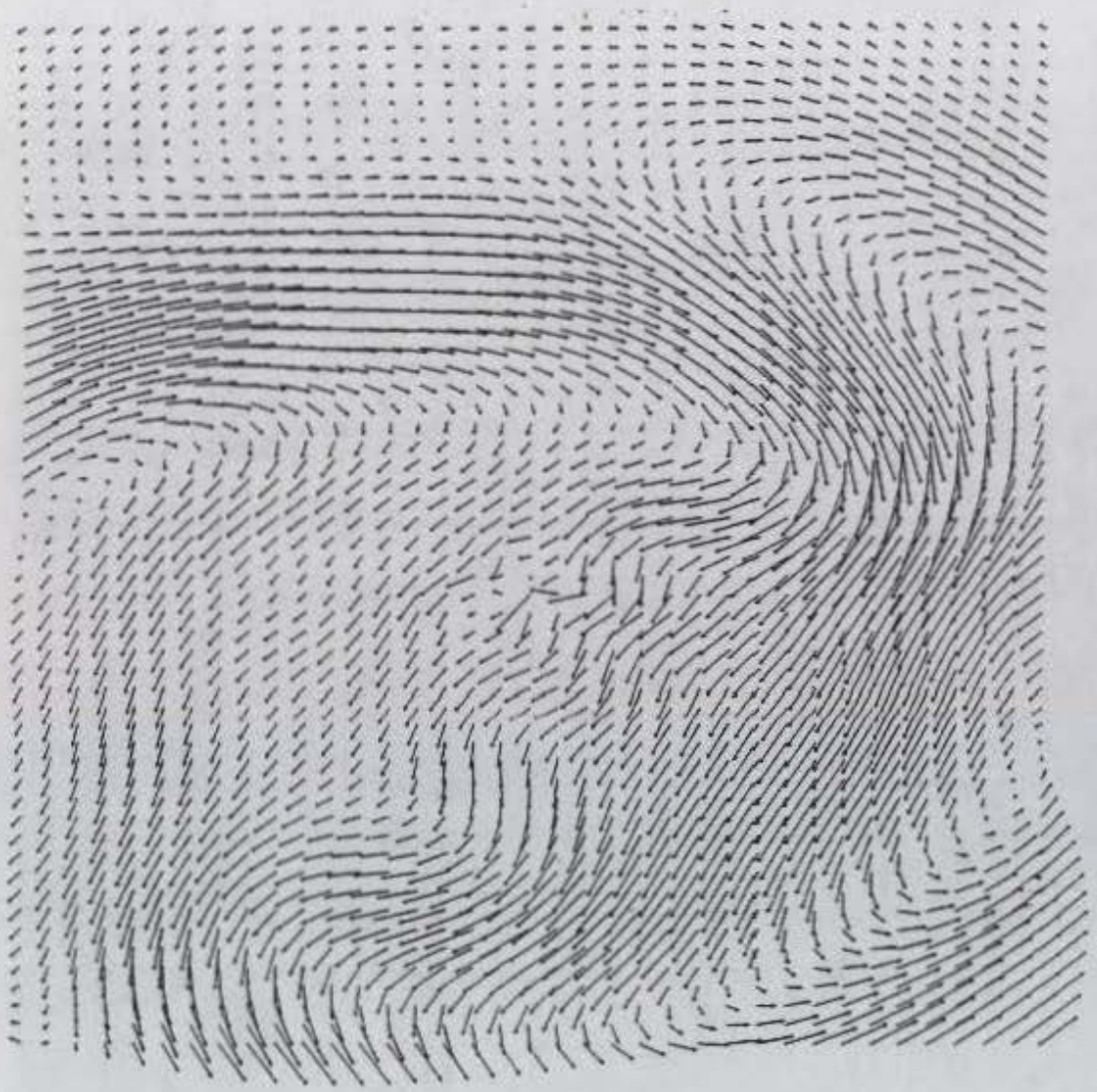

Figure 36. *Heppner-Maynard* "BC" convection pattern.

5.2.1. Case A

We select a magnetic flux tube which convects along the auroral boundary area or the cusp which is around the throat region of the TOI. It starts at 76500 UT at a (latitude, longitude) of (71, 206) degrees and convects up to (75, 174) until 79200 UT. Figure

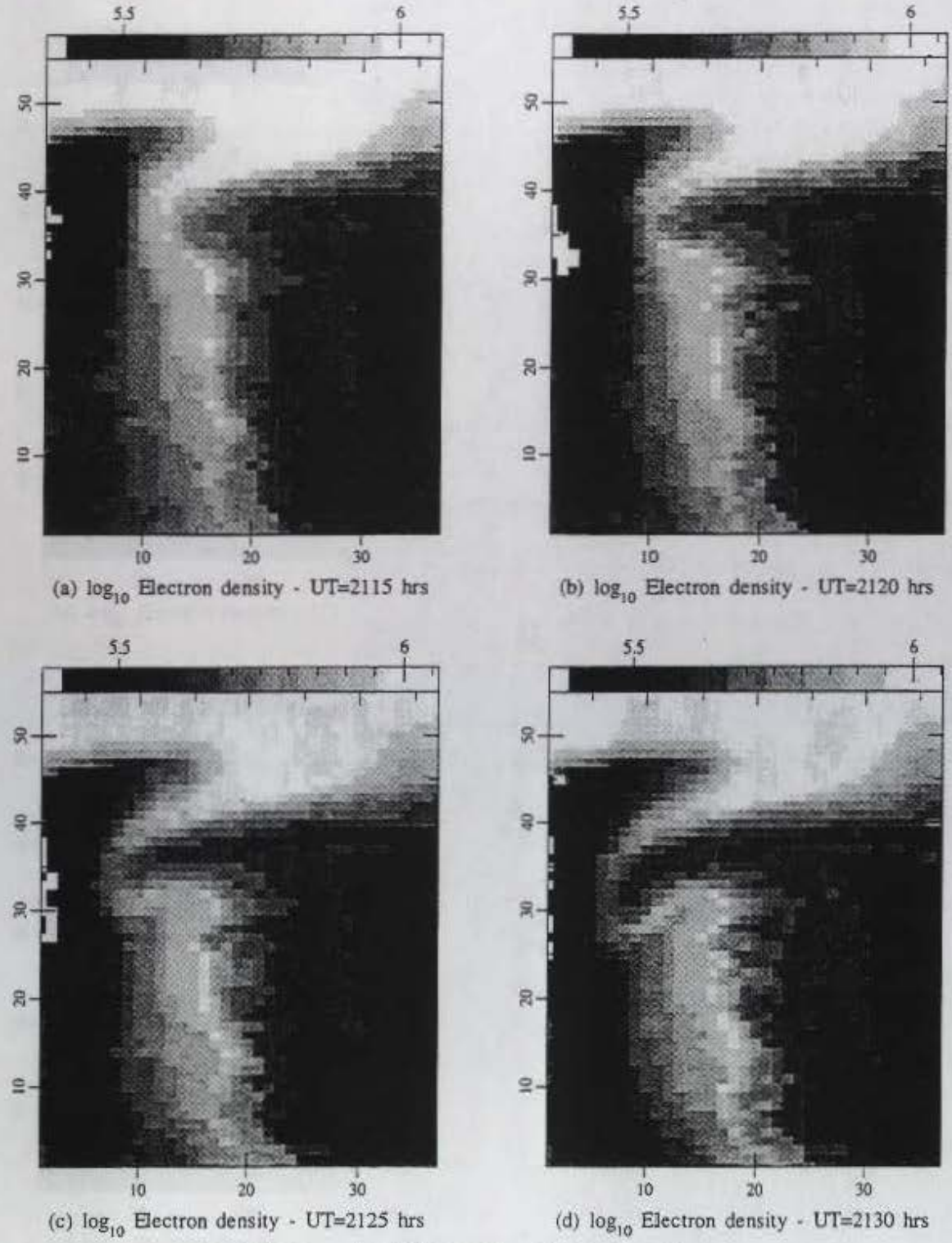

Figure 37. Electron density snapshots for (a) 2115 UT, (b) .2120 UT, (c) 2125 UT, and (d) 2130 UT.

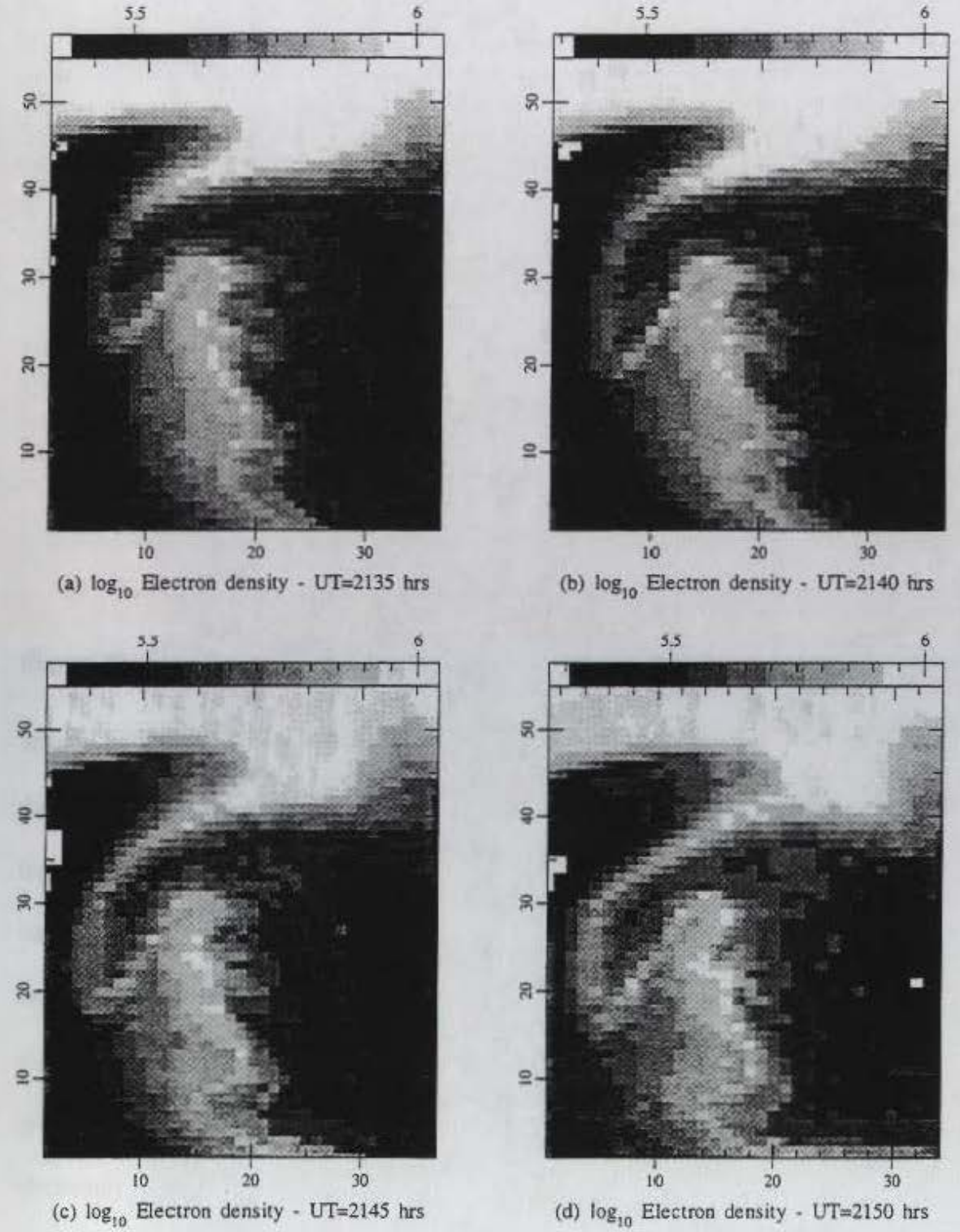

(a) $\log_{10}$ Electron density - UT=2135 hrs

(b) $\log_{10}$ Electron density - UT=2140 hrs

(c) $\log_{10}$ Electron density - UT=2145 hrs

(d) $\log_{10}$ Electron density - UT=2150 hrs

Figure 38. Electron density snapshots for (a) 2135 UT, (b) .2140 UT, (c) 2145 UT, and (d) 2150 UT.

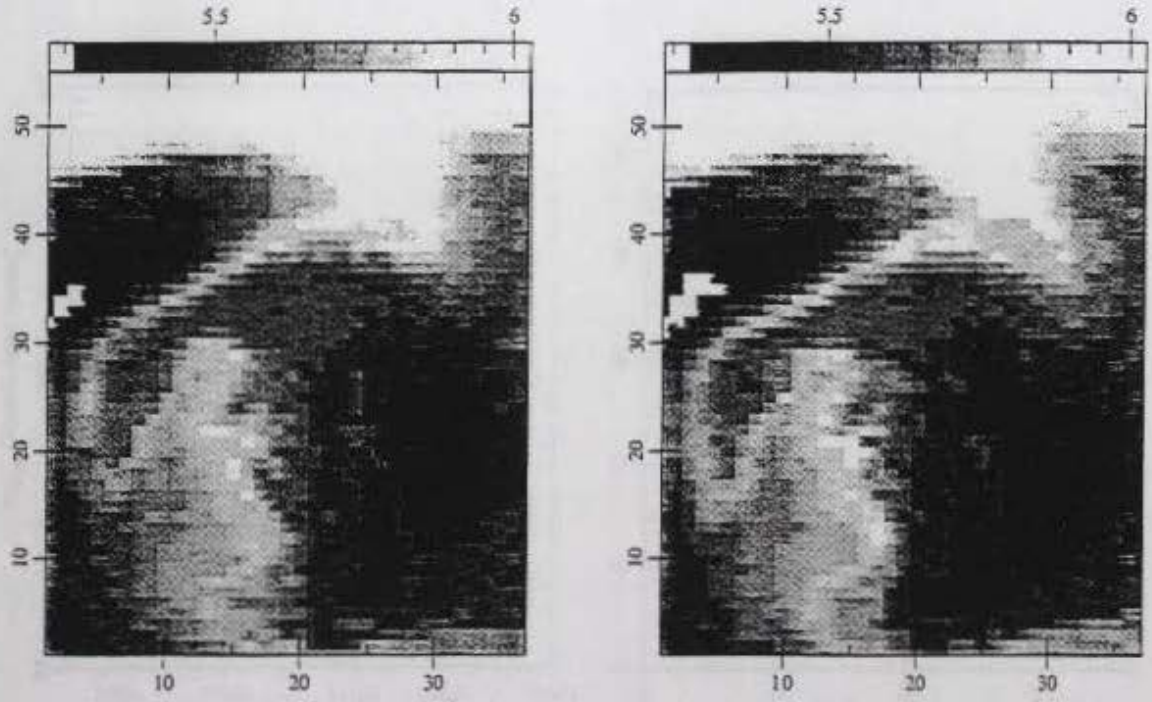

Figure 39. Electron density snapshots for (a) 2155 UT and (b) 2220 UT.

40(a) is the plot of the log of the growth time with UT in seconds. Figure 40(b) shows the successive points of the flux tube with UT. Table 1 lists the grid position, the scale length and the growth time of this flux tube at various times. The flux tube remains unstable through out the simulation period. Its growth rate varies between 44 and 108 seconds. Recall that the growth time is the time taken by a perturbation parameter of the plasma, say the perturbation in density or the perturbation in the electric potential, to grow by a factor of "e" (base of natural logarithms). The growth by the factor of "e" is commonly referred to as the "growth by an e-folding." For example if we say that the growth time is 44 seconds, the initial density perturbation has increased by a factor of "e" in 44 seconds or has undergone one e-folding. So for 300 seconds (5 minutes) from

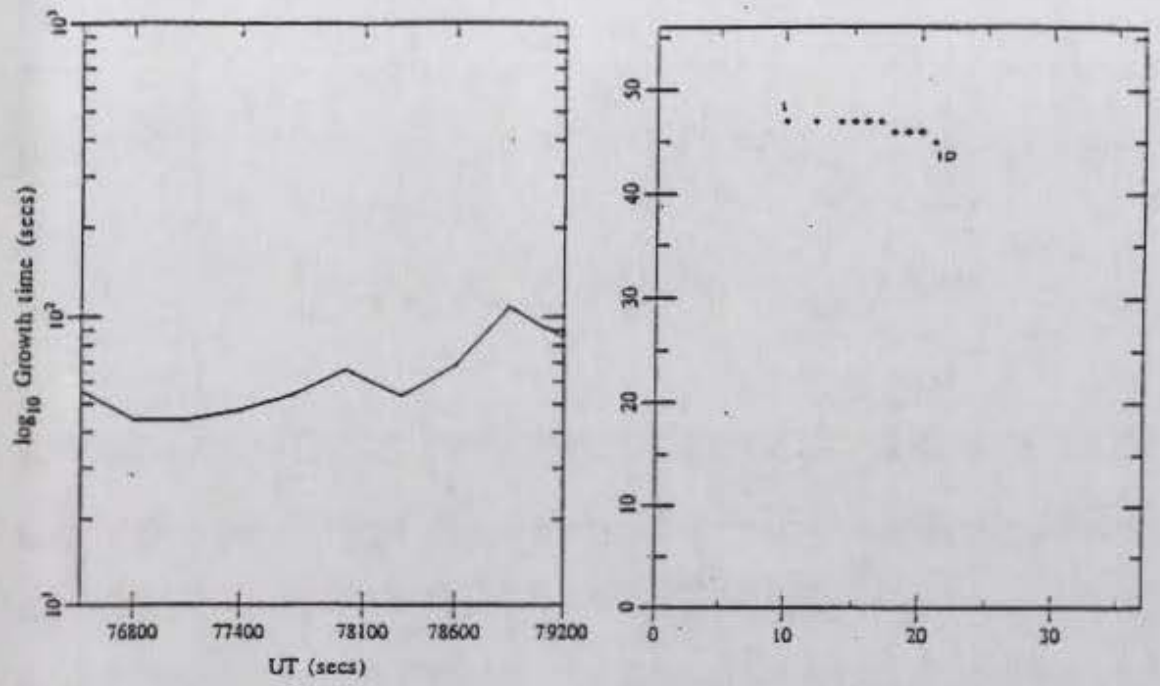

Figure 40. (a) Log plot of the growth time and (b) convection of the flux tube discussed in case A.

Table 1. Grid positions, scale lengths, and growth time for case A.

UT	X	Y	L (Km)	γ^{-1} (secs)
76500	8	47	203	60
76800	12	47	329	44
77100	14	47	397	44
77400	15	47	407	47
77700	16	47	456	53
78000	17	47	552	65
78300	18	46	526	53
78600	19	46	522	68
78900	20	46	592	108
79200	21	45	396	84

76500 UT to 76800 UT, the perturbation parameters of the flux tube at (8, 47), which has a growth time of 60 seconds (see Table 1), have undergone five e-foldings. When this flux tube moves to its next grid position where its growth time is 44 seconds, the parameters undergo about seven e-foldings in the 300 seconds until 77100 UT. From Figure 40 and Table 1 it is clear that this flux tube is never stable for the entire simulation period.

Of the 88 cases studied, only three cases had the flux tubes unstable through out the simulation period and all of them were along the edges of the cusp. A note is in order here. As far as I know, there seems to be no clear quantization as to how many e-foldings are needed before the plasma becomes irretrievably unstable and we get a permanent irregularity. Similarly, there is no definition of how many e-foldings are necessary before the perturbation enters the nonlinear domain. In the absence of theses definitions in the literature, let us **define** that as far as this thesis is considered, whenever we have five or more e-foldings the plasma is permanently irregular or unstable convectively and also goes into the nonlinear regime. Our definition may be off by a couple or more e-foldings but serves our purpose in this thesis. So with this definition we see that the flux tube under discussion is irretrievably unstable right from its first location at 76500 UT.

Another point to note is that the TDIM model does not use this information about the growth times to calculate the next snapshot, i.e., the snapshot at 76800 UT does not know about the GDI and its growth time at 76500 UT. This is because the transport equation formulation is based on the assumption that the waves occurring in the plasma

are not important and consequently cannot appear in the formulation. So each snapshot has to be necessarily treated independent of the previous one.

5.2.2. Case B

We choose a flux tube that starts at the edge of the throat with grid position (16,45) and convects down to (33, 9). This tube begins in an unstable region, moves into a stable region, and finally ends up in unstable regions. Figure 41(a) shows the growth time and (b) shows the grid position of the flux tube with UT. Table 2 lists the grid position, scale length and the growth time. At 76500 UT this flux tube has a growth time of 186 seconds, so it suffers about 1.6 e-foldings in 300 seconds. This is not enough to drive it into a permanent irregularity based on our definition. So this flux tube still has a chance to recover from the instability and become stable. However, it moves into a regions with lesser growth times until 77700 UT. At 77700 UT it has a growth time of 60 seconds, which gives it five e-foldings, hence driving it into a permanent irregularity. At 77700 UT when B_y is strongly negative and we have a *Heppner-Maynard* "DE" convection pattern, it enters a region of stability. But it is too late since it has already reached the "no return" zone at 77400 UT. After 77700 UT when the convection pattern is switched to "BC," it moves into regions of low growth rates where it suffers more than five e-foldings. We can say that even though this flux tube is momentarily stable, its initial growth rates are low enough to drive it completely irregular.

As a contrast to the case discussed above, consider the results shown in Figure 42 for a flux tube convecting from (14, 32) to (13, 24) along the left edge of the TOI. Its

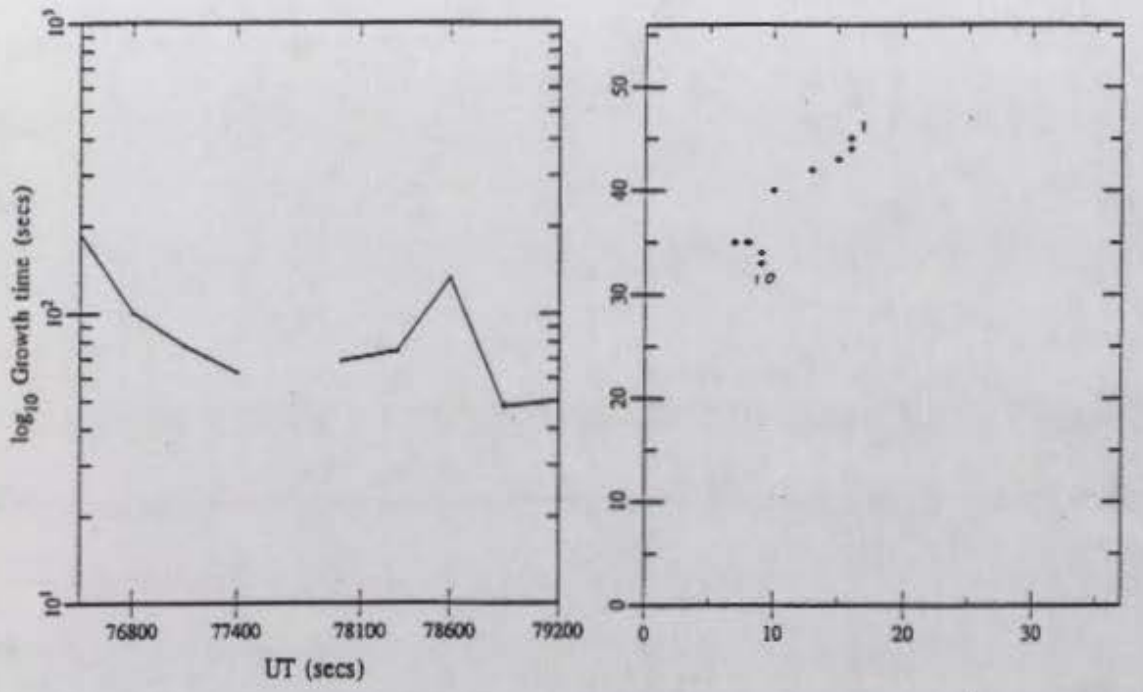

Figure 41. (a) Log plot of the growth time and (b) convection of the flux tube discussed in case B.

Table 2. Grid positions, scale lengths, and growth time for case B.

UT	X	Y	L (Km)	γ^{-1} (secs)
76500	16	45	1291	186
76800	16	44	1212	100
77100	15	43	829	76
77400	13	42	454	62
77700	10	40	388	stable
78000	7	35	1096	68
78300	8	35	389	74
78600	9	34	310	132
78900	9	34	220	47
79200	9	33	275	50

growth time at 76500 UT is about 80 seconds, which takes it through less than five e-foldings. So it may or may not go completely unstable. At 76800 UT it has a growth time of about 180 seconds, which definitely does not drive it total instability. At 77100 UT when the convection pattern switches to "BC," it moves into a stable region. So this flux tube recovers from its previous instability and becomes stable. Starting from 77400 UT, it again goes into unstable regions with high growth times until, at 78900, its growth time drops to about 50 seconds, driving it into a complete irregularity.

5.2.3. Case C

We now choose a case nearly similar to Case B. This flux tube starts at (16, 45) and reaches (10, 33), from the throat down along the left edge of the TOI. Figure 43 (a) shows the growth time and (b) shows the grid position of the flux tube with UT. Table 3 lists the grid position, scale length and the growth time. At 76500 UT this tube suffers an e-folding of about 1.6 and still can recover from the instability. In the next two UT steps it has such very low growth rates that it is driven completely irregular. At 77400 UT it is in a stable region. But it may be too late to recover from the earlier instability. At 77700 UT and 78000 UT when the convection pattern switches to "BC," it has very high growth times where it does not even go through one e-fold and again enters a stable region at 78300 UT. After 78300 UT it enters regions of low growth times, finally going completely unstable at 79200 UT. So though the flux tube is completely unstable at the beginning of 77100 UT, its subsequent passage into stable or high growth time regions may give it more time until it goes completely irregular. As an aside, we can also see

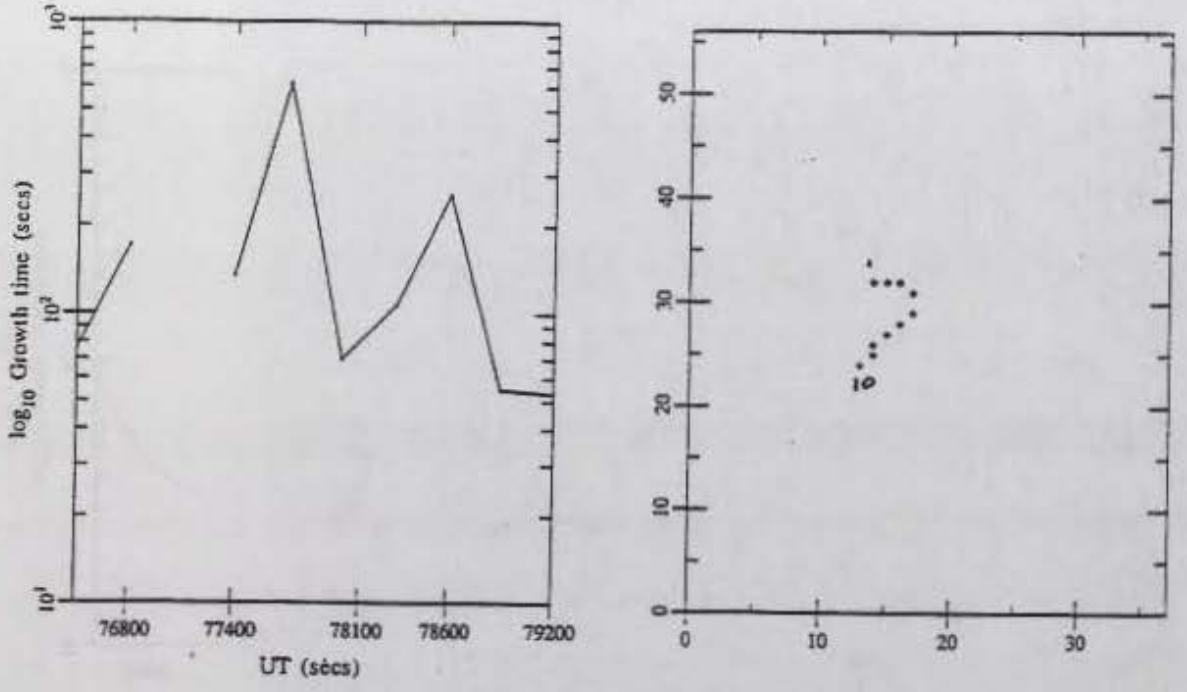

Figure 42. (a) Log plot of the growth time and (b) convection of the flux tube discussed in case B2.

from Figure 43(b) that it has very high convection speeds until 78300 UT. This high convection speed offsets the huge density gradients, hence giving relatively low growth times.

Of the 88 cases studied, most of them belonged either to case B or C and they were mostly concentrated on the throat region and the upper edges of the TOI. They are sometime in unstable regions with high or low growth times and sometimes in stable regions. There is no definite dependence on the applied B_y variation and hence the convection pattern, based on these limited 88 cases. Perhaps if we broaden our study to

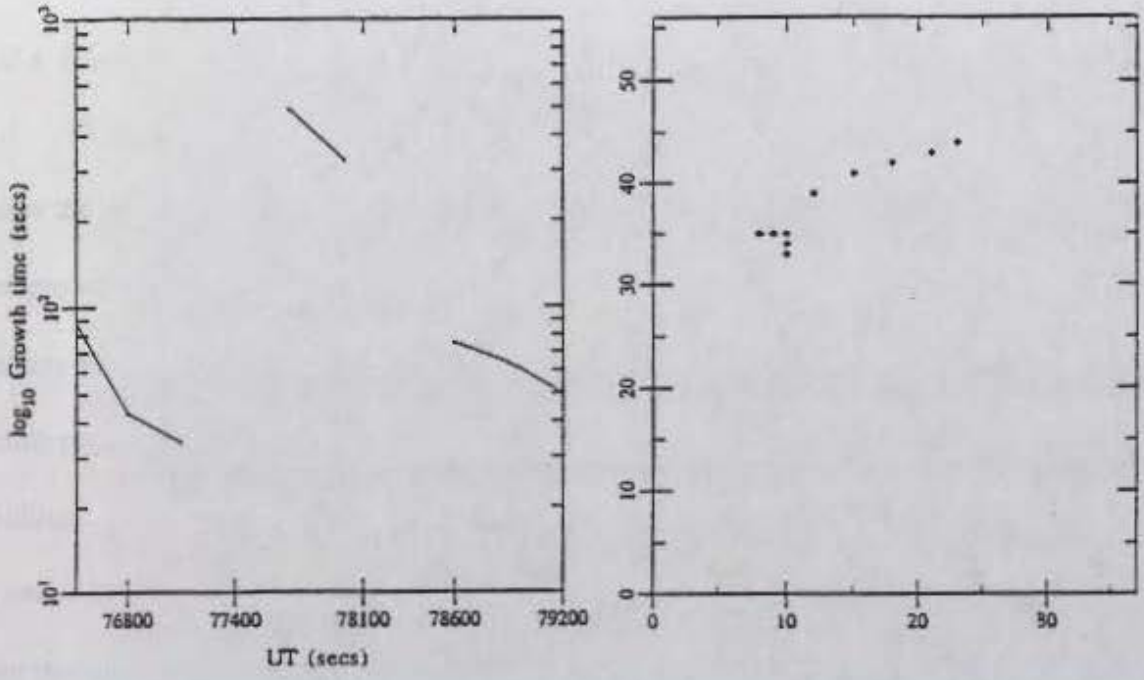

Figure 43. (a) Log plot of the growth time and (b) convection of the flux tube discussed in case C.

Table 3. Grid positions, scale lengths, and growth time for case C.

UT	X	Y	L (Km)	γ^{-1} (secs)
76500	16	45	1291	186
76800	21	43	716	43
77100	18	42	642	34
77400	15	41	633	stable
77700	12	39	463	492
78000	8	35	368	326
78300	9	35	585	stable
78600	10	35	339	75
78900	10	34	336	63
79200	10	33	283	49

cover more cases, we might deduce a dependence between the growth time variations and the change in the convection pattern.

5.2.4. Case D

We now choose a point that is stable except for two UT's. Figure 44(a) and (b) show the growth time and the convection of this point. Table 4 lists the grid position and the growth times. At 76500 UT this flux tube has a growth time of 80 seconds, and suffers an e-folding of 3.7, not enough to drive it completely irregular. It then stays in stable regions except at 78000 UT, where it is unstable. But it goes through about two e-foldings. So this point is driven toward stability though out the simulation period, though it strays into an unstable region for 300 seconds. There were not more than four points like this one among the 88 cases studied.

5.2.5. Case E

Finally we consider a flux tube that never ventures into an unstable region. Figure 45 shows the grid positions of this flux tube. It starts at (19, 55) and convects to (15, 55) along the edge of our region of interest on the sunlit side. It is in a stable region throughout the simulation period. This is expected because there are no sharp density gradients developing along the sunlit side. The uniform plasma production along these regions prevents steep density gradients and hence the GDI. Of the 88 cases studied, all the cases, which had flux tubes convect along the sunlit side had no unstable regions.

This chapter started with an illustration of the method of convective instability analysis of the GDI using data set 1. Results and their analysis from data set 2 trace the

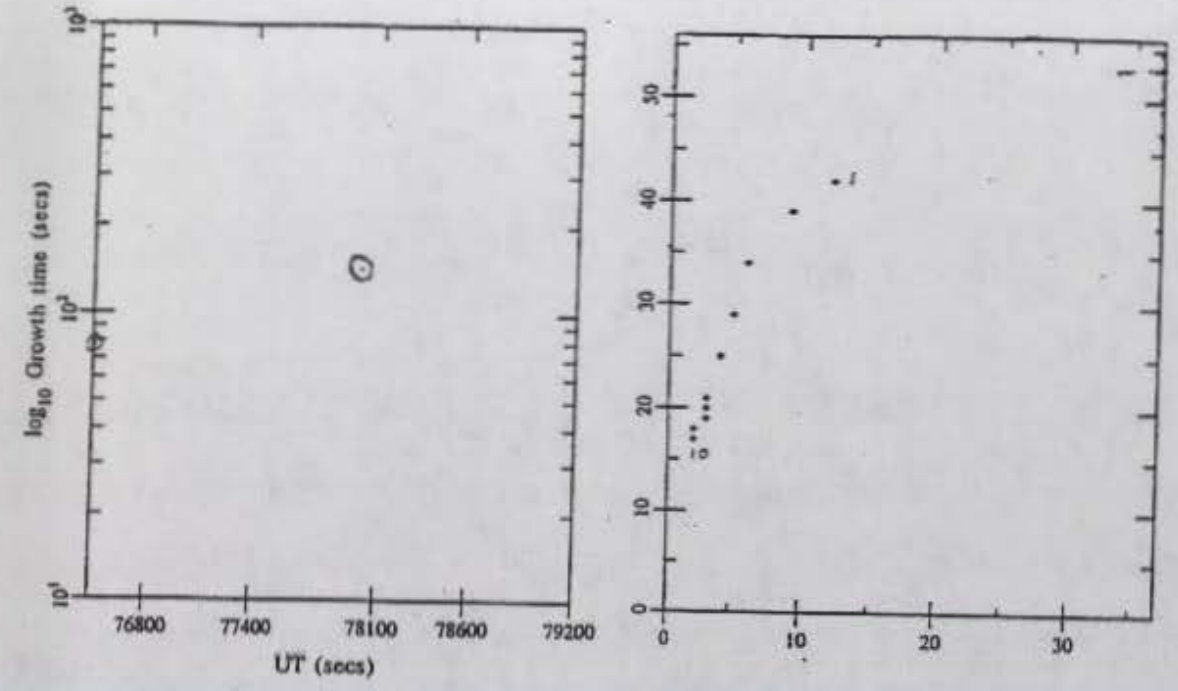

Figure 44. (a) Log plot of the growth time and (b) convection of the flux tube discussed in case D.

Table 4. Grid positions, scale lengths, and growth time for case D.

UT	X	Y	L (Km)	γ^{-1} (secs)
76500	12	42	659	79
76800	9	39	482	stable
77100	6	34	422	stable
77400	5	29	584	stable
77700	4	25	405	stable
78000	3	21	916	142
78300	3	20	280	stable
78600	3	19	267	stable
78900	2	18	418	stable
79200	2	17	259	stable

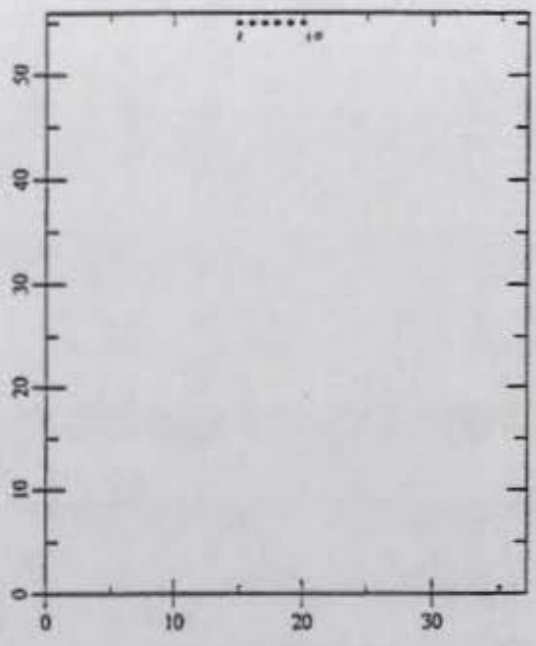

Figure 45. Convection of the flux tube discussed in case E.

growth rate variations of selected flux tubes. We have presented five characteristic cases and discussed the change in the growth times during the entire simulation period, identifying when a flux tube is driven towards complete irregularity and when it is not. In the next chapter we will present a summary and the results along with the directions for further research.

CHAPTER 6

SUMMARY AND CONCLUSION

6.1. Summary

The high-latitude ionosphere consists of large scale density structures. Chief among them are the polar cap patches with horizontal dimensions of about 1000 kilometers, which convect antisunward across the polar cap. The edges of these patches are characterized by steep density gradients, which, along with the ambient electric field present an excellent source region for the initiation of the Gradient Drift Instability (GDI). The GDI is a macro scale instability with scale sizes greater than about a kilometers. If a perturbation is introduced in the gradient region, GDI is initiated and it may either grow or damp depending on the orientation of the density gradient with respect to the ambient electric field. The growth rate of the instability is the parameter, which controls its growth or decay and the amount of growth or decay. The higher the growth rate the more rapidly will the medium become irregular as the result of the GDI.

Over the years many researchers have developed various theoretical expressions for the growth rates with varying degrees of complexity. We took the very simple growth equation and calculated the growth rate of the GDI in the polar ionosphere. We used the USU TDIM model, which is a global scale climatology model, to simulate the patches in the polar region. This model gives us the density, temperature, and convection velocity (based on the *Heppner-Maynard* convection model) profiles of polar cap patches in the macro scale domain of about 70 kilometers. Using this information with the growth rate equations enabled us to calculate the growth rate profile over the entire patch structure,

which was then analyzed for stability or instability. We also generated snapshots of the patches at different UT's and performed a convective instability analysis to ascertain the behavior of the flux tubes to the GDI in the time period of the snapshot.

Though many researchers have developed many equations for the GDI and analyzed them with ball park numbers, this is the **first time** that real ionospheric values have been used in a global analysis using model data to generate **two-dimensional maps of the growth rate** distribution in the polar cap region. These maps show regions of instability and the growth time of these regions. The conclusion of our analysis is presented below.

6.2. Conclusions

Our conclusion are as follows:

1. The plasma in the polar ionosphere exhibits GDI structure even when examined in the macro scale ionospheric structures like the polar cap patches, using global-scale climatological models like the TDIM and using the simple growth equations.
2. Regions of strong instability occur along the edges of the TOI and the throat region. The growth of the instability is quite rapid along the borders of the cusp region.
3. As the structure of the TOI changes with UT due to the variations in the convection pattern, the magnetic flux tubes can either be driven towards stability or instability. There are periods when they can be completely stable and there are some where they are quickly driven to a permanent irregularity when the perturbation parameters change by five e-foldings. There can also be situations when the flux tube is unstable but not strong enough to go through five e-foldings and may subsequently move into

a stable region, which wipes out the initial instability.

6.3. Suggestions for Further Research

This research has laid a procedural framework for convective instability analysis of the GDI. There may be numerous future research projects that can build on top of this framework. I could think of the following:

1. The time resolution of the UT snapshots and the spatial resolution within each snapshot can be reduced to obtain better estimates of the variation in the growth rates at lower scales. Statistical analysis can also be performed on the results to better understand the role of the convection pattern and UT on the evolution of the growth rates and hence better understand the factors that decide the stability or the instability of the flux tube.
2. The growth times and the consequent change in the perturbation parameters can be used as feedback to the USU TDIM model. So starting from a 'seed' pattern of the TOI, the TDIM can use the feedback information as another input to generate the subsequent time snapshots. In a way, we can make the TDIM "aware of the GDI." I intuitively feel that it can be done, though I am not sure of how to do this.
3. More detailed growth equations, which are multidimensional and take into effect the various factors (for example, the coupling effects of the F region with the magnetosphere and the E region, background plasma effects, precise role of the neutral winds, etc.) affecting the growth of the GDI, can be used to obtain more realistic growth times.

4. Generate maps of irregularity formation where the flux tubes of the TOI are marked with the degree of irregularity, i.e., how many e-foldings has it gone through and whether it has been driven completely irregular. Amongst other uses such a map can be used with experimental data to identify irregularity regions throughout the polar ionosphere.

REFERENCES

Anderson, D. N., J. Buchau, and R. A. Heelis, Origin of density enhancements in the winter polar cap ionosphere, *Radio Sci., 23,* 513, 1988.

Basu, S., Su. Basu, P. K. Chaturvedi, and C. M. Bryant, Jr., Irregularity structures in the cusp/cleft and the polar cap regions, *Radio Sci., 29,* 195, 1994.

Buchau, J., B. W. Reinisch, E. J. Weber, and J. G. Moore, Structure and dynamics of winter polar cap F region, *Radio Sci., 18,* 995, 1983.

Buchau, J., B. W. Reinisch, E. J. Weber, and J. G. Moore, D. N. Anderson, H. C. Carlson, Jr., and R. C. Livingstone, ionospheric structure in the polar cap: Their origin and relation to 250-MHz scintillation, *Radio Sci., 20,* 325, 1985.

Carlson, H. C., Jr., V. B. Wickwar, E. J. Weber, J. Buchau, J. G. Moore, and W. Whiting, Plasma characteristics of polar cap F layer arcs, *Geophys. Res. Lett., 11* , 895, 1984.

Cerisier, J. C., and J. J. Berthelier, Unstable density gradients in the high latitude ionosphere, *Radio Sci., 20,* 755, 1985.

Chen, F. F., *Introduction to Plasma Physics and Controlled Fusion*, Second Edition, Volume 1, Plenum Press, New York, 1983.

Hardy, D. A., M. S. Gussenhoven, R. Raistrick, and W. J. McNeil, Statistical and functional representations of the pattern of auroral energy flux, number flux, and conductivity, *J. Geophys. Res., 92,* 12275, 1987.

Hargreaves, J. K., *The Solar-Terrestrial Environment*, Cambridge Atmospheric and Space Sciences Series, Cambridge, Massachusetts, 1992.

Hedin, A. E., MSIS-86 thermospheric model, *J. Geophys. Res., 92,* 4649, 1987.

Heelis, R. A., J. K. Lowell, and R. W. Spiro, A model of the high latitude ionosphere convection pattern, *J. Geophys. Res., 87,* 6339, 1982.

Heppner, J. P., and N. C. Maynard, Empirical high latitude electric field models, *J. Geophys. Res., 92,* 4467, 1987.

Huba, J. D., S. L. Ossakow, P. Satyanarayana, and P. N. Guzdar, Linear theory of the $E \times B$ instability with an inhomogeneous electric field, *J. Geophys. Res., 88,* 425, 1983.

Huba, J. D., and S. T. Zalesak, Long wavelength limit of the $E \times B$ instability, *J. Geophys. Res., 88,* 10263, 1983

Kelly, M. C., *The Earth's Ionosphere*, Academic Press, Inc., New York, 1992.

Keskinen, M. J., and S. L. Ossakow, Nonlinear evolution of plasma enhancements in the auroral ionosphere, Long wavelength irregularities, *J. Geophys. Res., 87*, 144, 1982.

Keskinen, M. J., and S. L. Ossakow, Theories of high latitude ionospheric irregularities: A review, *Radio Sci., 18*, 1077, 1983.

Knudsen, W. C., Magnetospheric convection and the high latitude F2 ionosphere, *J. Geophys. Res., 79*, 1046, 1974.

Knudsen, W. C., P. M. Banks, J. D. Winningham, and D. M. Klumpar, Numerical model of the convection F2 ionosphere at high latitudes, *J. Geophys. Res., 82*, 4784, 1977.

Lockwood, M., and H. C. Carlson, Jr., Production of polar cap electron density patches by transient magnetopause reconnection, *Geophys. Res. Lett., 19*, 1731, 1992.

Linson L. M., and J. B. Workman, Formation of striations in ionospheric plasma clouds, *J. Geophys. Res., 75*, 3211, 1970.

Ossakow, S. L., P. K. Chaturvedi, and J. B. Workman, High altitude limit of the gradient drift instability, *J. Geophys. Res., 83*, 2691, 1978.

Potemra, T. A., Magnetospheric currents, *John Hopkins APL Tech. Digest, 4*, 276, 1983.

Rino, C. L., R. C. Livingston, R. T. Tsunoda, R. M. Robinson, J. F. Vickery, C. Senior, M. D. Cousins, J. Owen, and J. A. Klobuchar, Recent studies of the structure and morphology of auroral zone F region irregularities, *Radio Sci., 18*, 1167, 1983.

Robinson, R. M., R. T. Tsunoda, J. F. Vickery,. and L. Guerin, Sources of F region ionization enhancements in the nighttime auroral zone, *J. Geophys. Res., 90*, 7533, 1985.

Schunk, R. W., *The Terrestrial Ionosphere, Solar Terrestrial Physics, 609*, Reidel Publishing Company, New York, 1983.

Schunk, R. W., A mathematical model of the middle and high latitude ionosphere, *Pure Appl. Geophys., 127*, 255, 1988.

Sojka, J. J., Global scale, physical models of the F region ionosphere, *Rev. Geophy., 27*, 371, 1989.

Sojka, J. J., M. D. Bowline, R. W. Schunk, D. T. Decker, C. E. Valladares, R. Sheehan, N. Anderson, and R. A. Heelis, Modeling polar cap F region patches using time varying convection, *Geophys. Res. Lett, 20*, 1783, 1993.

Tsunoda, R. T., High latitude F region irregularities: A review and synthesis, *Rev. Geophys., 26*, 719, 1988.

Weber , E. J., J. Buchau., J. G. Moore, J. R. Sharber, R. C. Livingston, J. D. Winningham, and B. W. Reinisch, F layer ionization patches in the polar cap, *J. Geophys. Res., 89*, 1683, 1984.

Weber E. J., J. A. Klobuchar, J. Buchau, H. C. Carlson, Jr., R. C. Livingston, O. de la Beaujardiere, M. McCready, J. G. Moore, G. J. Bishop, Polar cap F layer patches: Structures and dynamics, *J. Geophys. Res., 91*, 12,121, 1986.

APPENDIX

IONOSPHERIC PARAMETERS, THEIR EXPRESSIONS AND THEIR PROFILES

1. Geomagnetic field

The earth's magnetic field is to a good approximation that of a centered dipole. The expression for the magnetic field strength is easily derived from electro-magnetic theory as

$$B(r,\phi) = \frac{M}{r^3}\left(1+3\sin^2\phi\right)^{1/2} \text{ gauss}$$

where M is the magnetic moment at the surface of the earth (8.05×10^{19} Gm^3), r is the distance of the field point from the center of the earth ($r = R_e + h$, $R_e = 6371$ Km) and ϕ is the magnetic latitude of the field point.

2. Gyro Radius

When charged particles are placed in a magnetic field they experience a magnetic force, In the absence of any other force the particles gyrate about the magnetic field lines. The direction of gyration is given by Lenz's law, according to which the particles gyrate in such a direction so that the magnetic field generated by them is opposite to the external field. A plasma is hence diamagnetic in the sense that it always tries to reduce the externally applied magnetic field. Gyro radius can be calculated using

$$r_e = 0.0223\frac{\left(T_e\right)^{1/2}}{B} \text{ cm.},$$

and

$$r_i = 0.9485\frac{(T_i A_i)^{1/2}}{B} \text{ cm}$$

Figure 46 shows the gyro radius calculated using data set 1. As expected it follows the temperature profile of the species.

3. Gyro Frequency

This the number of gyrations per second made by the charged particles placed in the magnetic field. This is an important parameter used to identify inertia dominated regions in the ionosphere. Gyro frequency for the electrons and ions is given by

$$\Omega_e = (2.7993 \times 10^6)B \text{ Hz}$$

and,

$$\Omega_i = (1.5246 \times 10^3)B \text{ Hz}$$

Figure 47 shows the gyro frequency for the different species calculated from data set 1. Note that gyro frequency decreases with altitude since it is directly proportional to the magnetic field intensity.

4. Collision Frequencies

Collision frequency as it occurs in the momentum equation is a rate of transfer of momentum between the colliding particles. It is a very important parameter of partly ionized plasmas.

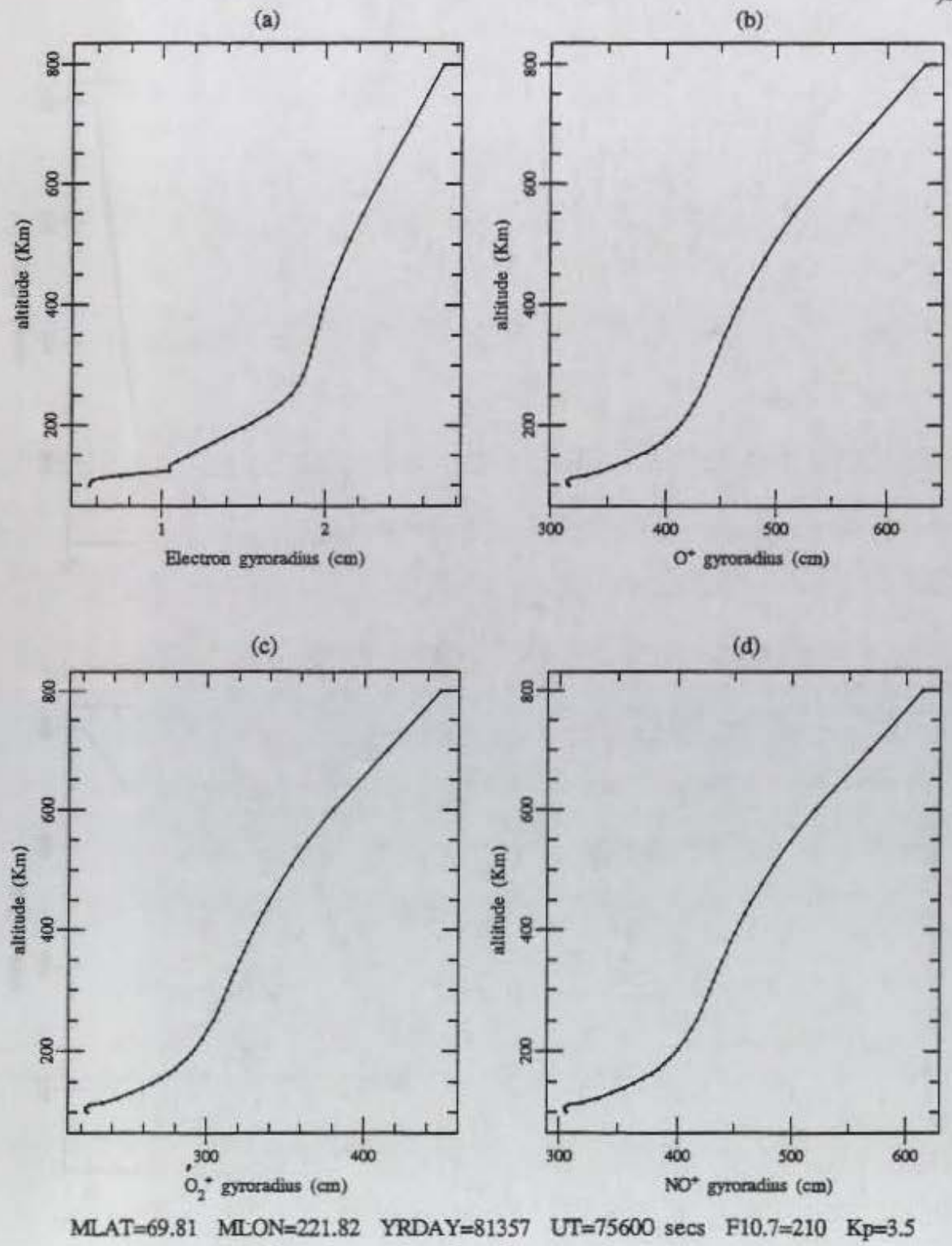

Figure 46. Altitude profile of the gyro radius of charged particles.

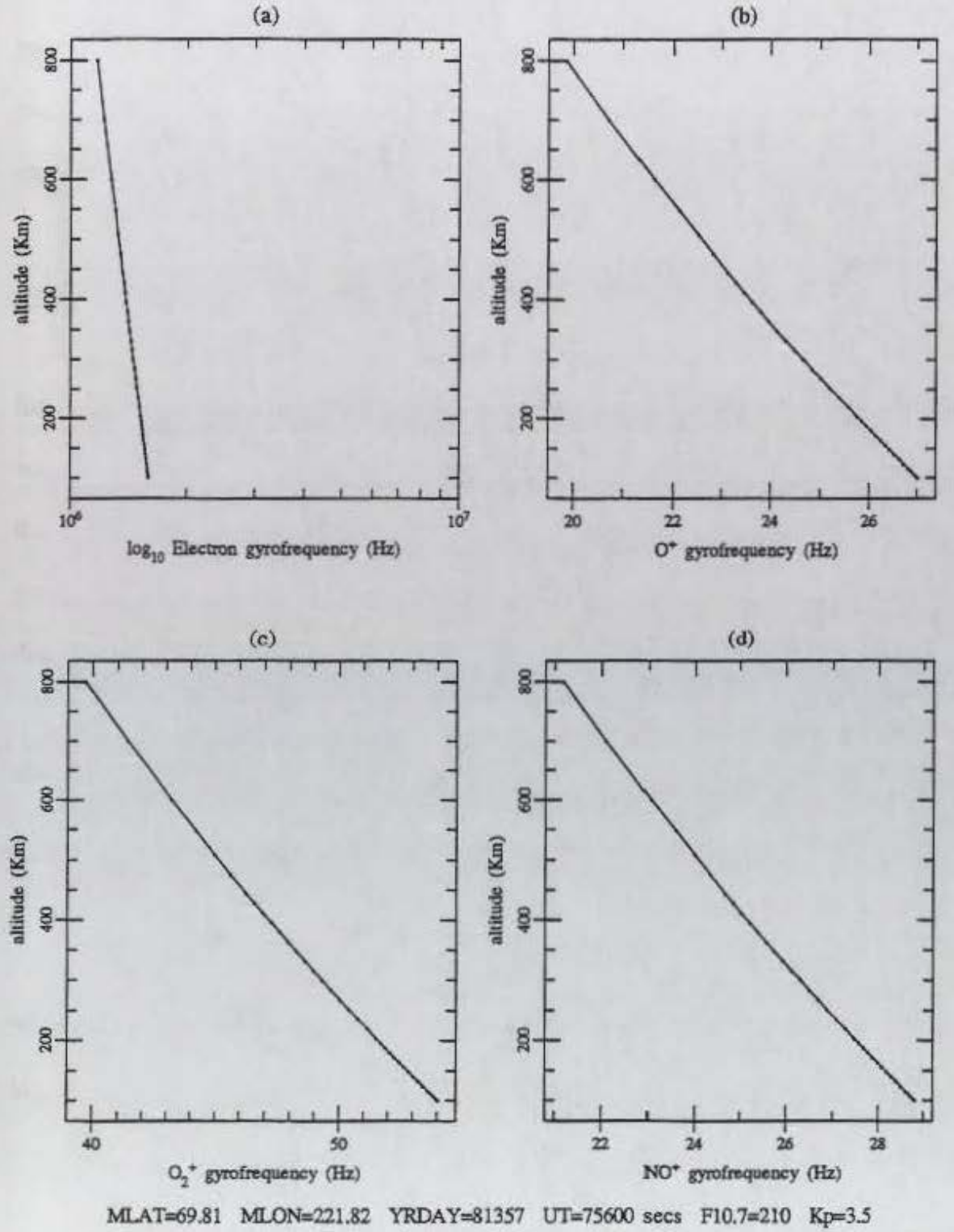

Figure 47. Altitude profile of the gyro frequency of charged particles.

There are many different types of collisions in plasma. We will discuss the relevant collision frequencies in the following sections. Note that we will only consider two-body collisions, which may be between like or unlike charges and between the charges and the neutrals.

4.1. Coulomb collisions

This is the frequency of interaction between charged particles due to the Coulomb force. The collision may be between like or unlike charges. In the fluid approach we do not take into account the ion-ion and the electron-electron collisions. This is because these collisions affect the velocity distribution of the plasma, and in the fluid approach we assume a uniform Maxwellian distribution i.e., we neglect deviations in the velocity distribution. They do need to be considered in the kinetic approach.

The general equation for the collision frequency of coulomb collisions for singly charged species is

$$\upsilon_{\alpha\beta} = \frac{16\sqrt{\pi}}{3}\left(\frac{\mu_{\alpha\beta}}{2KT_{\alpha\beta}}\right)^{3/2}\left(\frac{e_\alpha e_\beta}{\mu_{\alpha\beta}}\right)^2 \frac{n_\beta m_\beta}{\left(m_\alpha + m_\beta\right)} \ln\Lambda$$

where $\mu_{\alpha\beta}$ is the reduced mass, $T_{\alpha\beta}$ is the reduced temperature and $\ln\Lambda$ is the coulomb logarithm (≈ 15 for the ionosphere).

For electron-ion collisions this equation reduces to

$$\upsilon_{ei} = 3.64 \frac{n_i}{T_e^{3/2}} \ln \Lambda$$

A similar expression can be calculated for ion-electron collisions, but we can always use the principle of conservation of momentum and calculate it from the equality

$$n_\alpha m_\alpha \upsilon_{\alpha\beta} = n_\beta m_\beta \upsilon_{\beta\alpha}$$

The coulomb logarithm can be rigorously calculated from the expression

$$\ln \Lambda = \ln\left(\frac{4KT_e}{\gamma^2 e^2 k_e}\right) - \frac{k_e^2 + k_i^2}{k_i^2} \ln\left(\sqrt{\frac{k_e^2 + k_i^2}{k_e^2}}\right)$$

with

$$k_e^2 = \frac{4\pi n_e e^2}{KT_e}; \quad k_i^2 = \frac{4\pi n_i e^2}{KT_i}; \quad \ln\gamma = 0.577 \text{ (Euler's log)}$$

Figure 48 shows the collision frequency of the electron with the various ions. Panel (a) shows the average electron-ion collision frequency (weighted with the density of the ions). Figure 49. shows the collision frequency of the various ions with the electrons. Panel (a) shows the average ion collision frequency (weighted with the density of the ions). The results obtained using the data set are consistent with other similar results.

4.2. Ion-neutral collisions

The ion-neutral collisions can be either resonant or non-resonant. Resonant charge exchange occurs when an ion collides with its parent neutral. The reaction is of the form $P + p^+ \leftrightarrow P^+ + p$, where P is the parent neutral and p is the corresponding ion. Charge exchange also occurs accidentally as in the reaction $H^+ + O \leftrightarrow H + O^+$. The following table (Table 5) gives important ion-neutral resonant momentum transfer frequencies in different temperature domains.

Non-resonant ion-neutral collisions occur between unlike ions and neutrals. The interaction is due to the polarization of the neutral when the ion passes nearby. This makes the neutrals behave like an electric dipole. Consequently the ion and the neutral attract electro- statically. At higher temperatures as the ion gets closer to the neutral the long range dipole attraction is replaced by a short range quantum mechanical repulsion. The expression for ion-neutral non-resonant momentum transfer collision frequency is,

Table 5. Ion-neutral resonant collision frequencies.

Species	$T = \frac{T_i + T_n}{2}$	υ_{in}
$H^+ - H$	$T > 50$	$2.65 \times 10^{-10} n_H \sqrt{T}(1 - 0.083 \log T)^2$
$He^+ - He$	$T > 50$	$8.73 \times 10^{-11} n_{He} \sqrt{T}(1 - 0.093 \log T)^2$
$N^+ - N$	$T > 275$	$3.83 \times 10^{-11} n_N \sqrt{T}(1 - 0.063 \log T)^2$
$O^+ - O$	$T > 235$	$3.67 \times 10^{-11} n_O \sqrt{T}(1 - 0.064 \log T)^2$
$O_2^+ - O_2$	$T > 800$	$2.59 \times 10^{-11} n_{O_2} \sqrt{T}(1 - 0.073 \log T)^2$
$H^+ - O$	$T > 300$	$6.61 \times 10^{-11} n_O \sqrt{T}(1 - 0.047 \log T_i)^2$

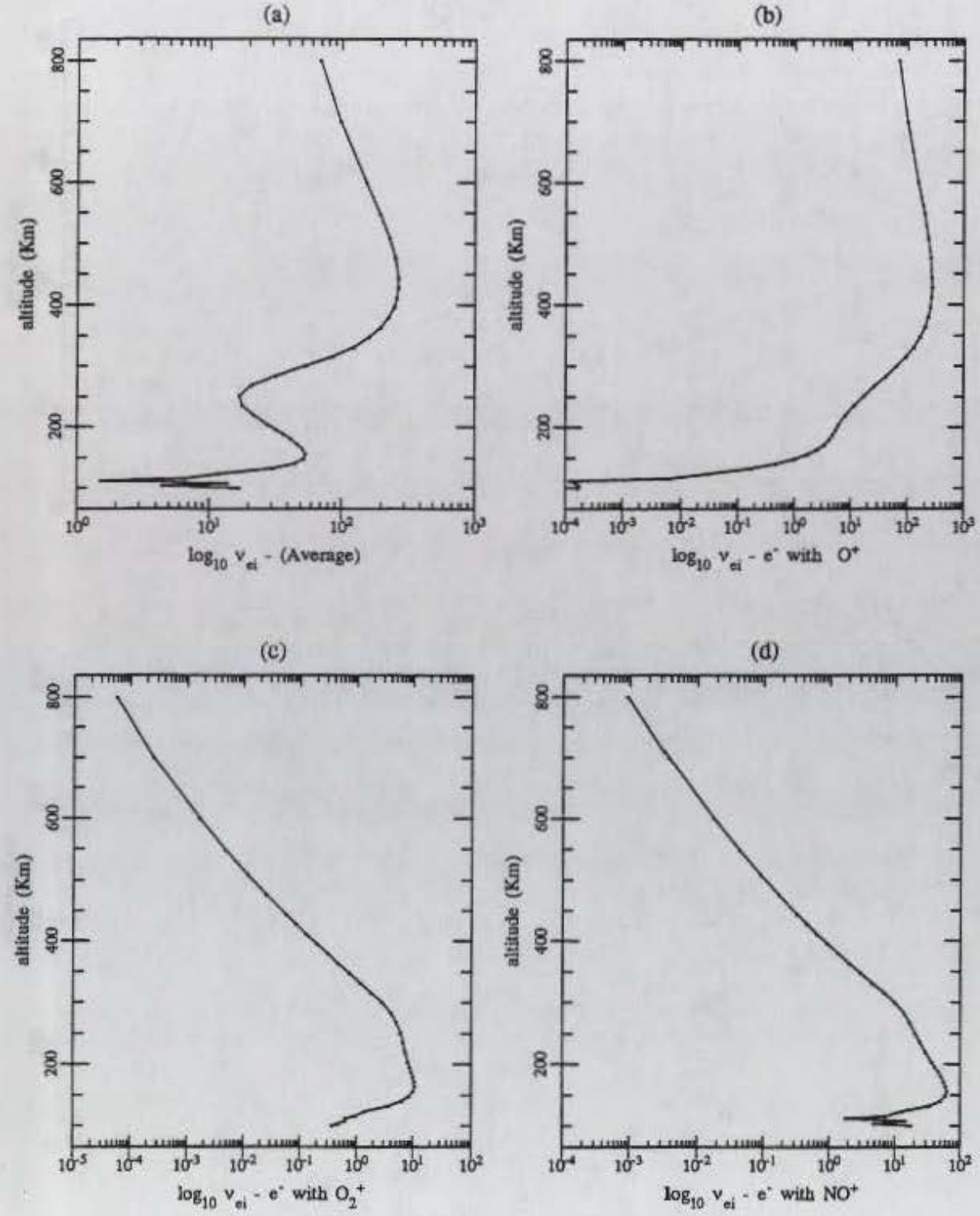

Figure 48. Altitude profile of (a) the average electron-ion collision frequency and (b)-(d) electron with the individual ions.

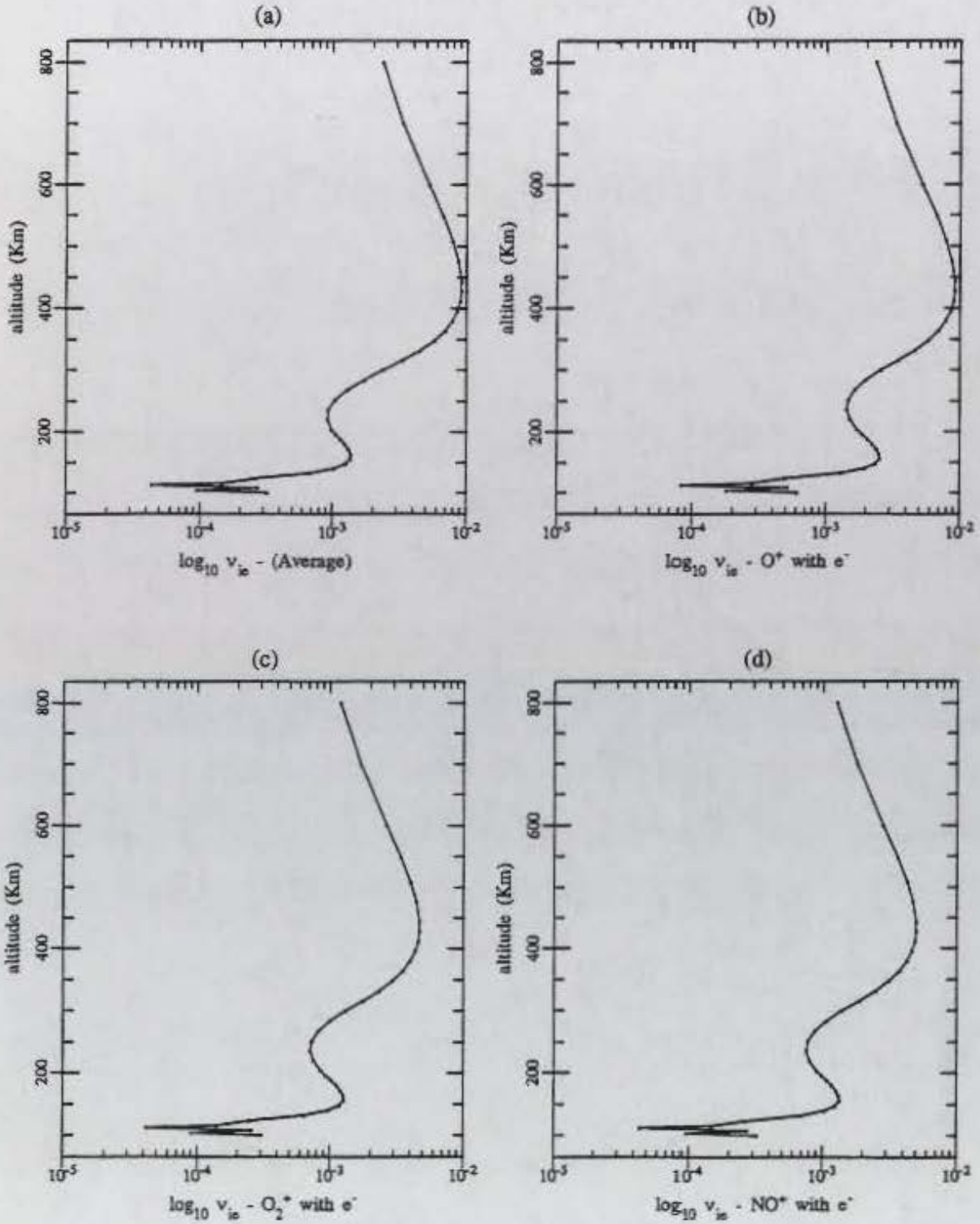

Figure 49. Altitude profile of (a) the average ion-electron collision frequency and (b)-(d) individual ions with the electron.

$$\upsilon_{in} = 2.21\pi\left(\frac{\gamma_n e^2}{\mu_{in}}\right)^{1/2} \frac{n_n m_n}{m_i + m_n}$$

where γ_n is the neutral atom polarizability. For a given ion-neutral pair this equation can be written simply as $\upsilon_{in} = C_{in} n_n$. The constant C_{in} is given in Table 6 for different ion-neutral pairs (in multiple of 10^{10}). Note that the letter 'r' means that the interaction is resonant.

Figure 50 shows the average ion-neutral collision frequency including both the resonant and non-resonant collisions. Panel (a) shows the average of all the ions together and the other panel shows the average for each individual ion.

4.3. Electron-neutral collisions

The electron-neutral collision frequencies used today are mostly from experimental data. Table 7 gives the collision frequency for the neutral species in our data set. Figure 51 gives the electron-neutral collision frequency profiles. Panel (a) is a weighted average collision frequency.

Table 6. Value of the constant C_{in} for various ion-neutral pairs (in multiples of 10^{10}).

Neutrals Ions	H	He	N	O	N_2	O_2
H^+	r	10.6	26.1	r	r	32.0
He^+	4.71	r	11.9	10.1	33.6	15.3
N^+	1.45	1.49	r	4.42	16.0	7.25
O^+	r	1.32	4.62	r	7.47	6.64
N_2^+	0.74	0.79	2.95	2.58	6.82	4.49
NO^+	0.69	0.74	2.79	2.44	r	4.27
O_2^+	0.65	0.70	2064	2031	4034	r

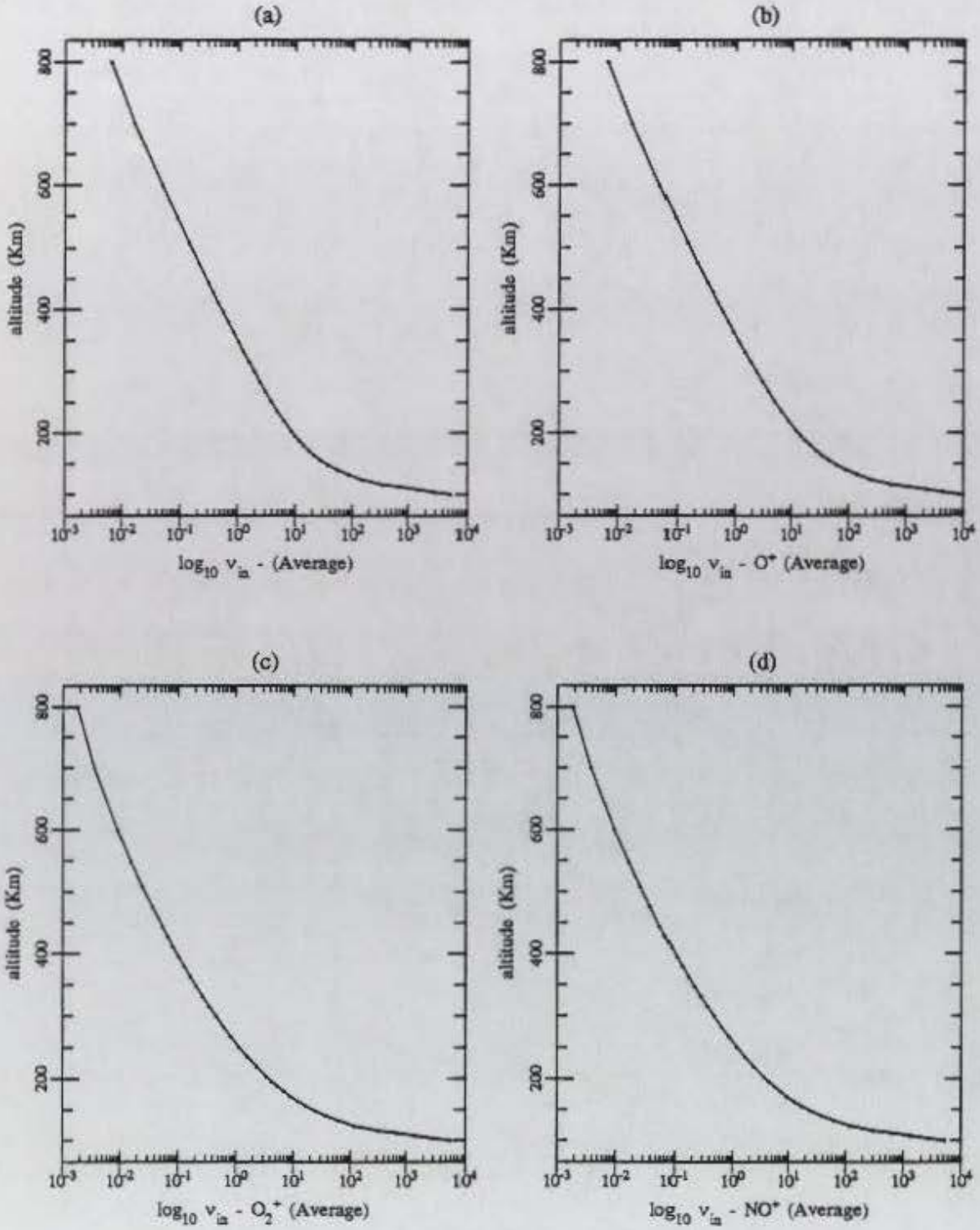

Figure 50. Altitude profile of (a) the average ion-neutral collision frequency and (b)-(d) individual ions with all the neutrals.

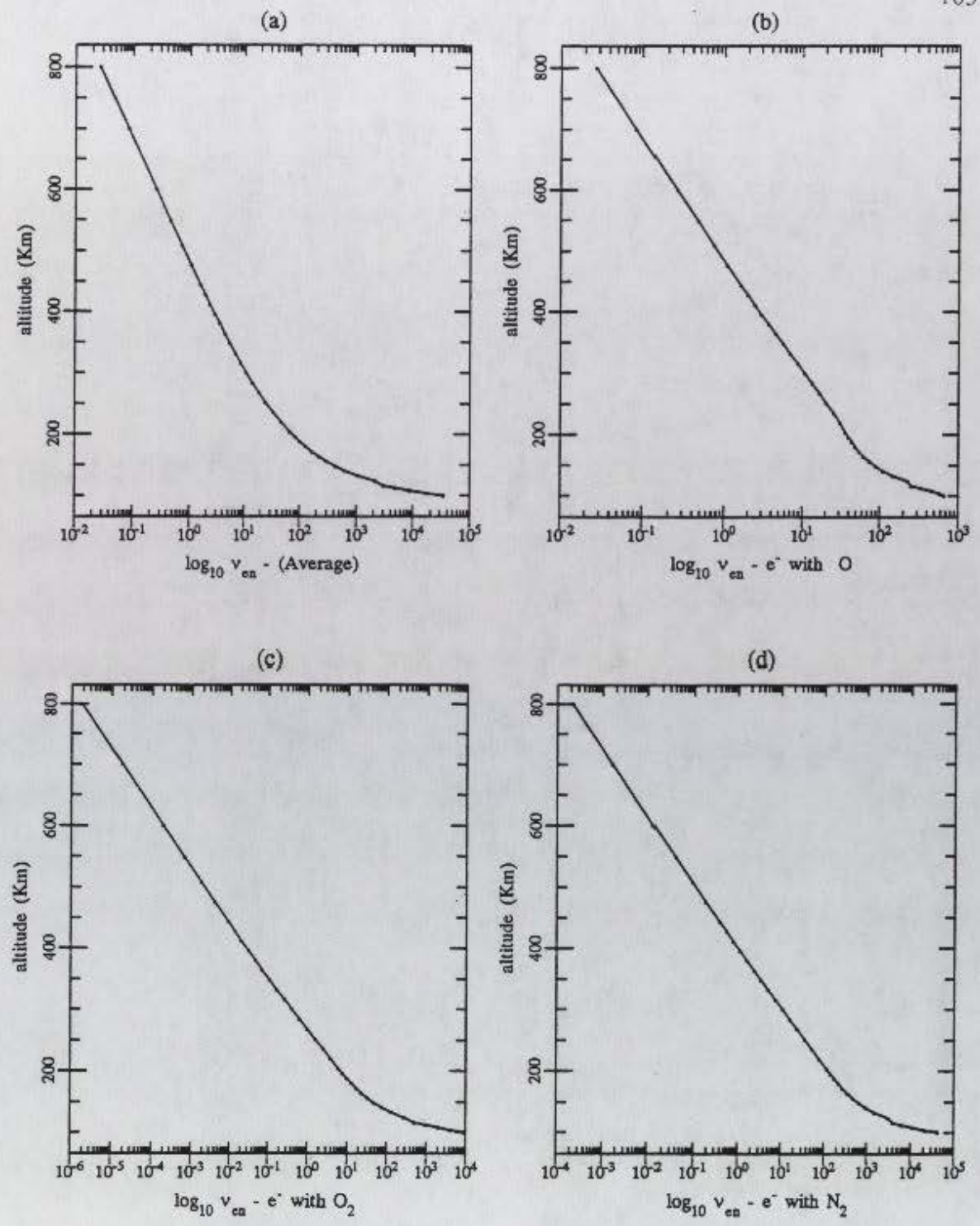

Figure 51. Altitude profile of (a) the average electron-neutral collision frequency and (b)-(d) electrons with the individual neutrals.

We have covered all the relevant collision frequencies. The total electron collision frequency is $\upsilon_e = \upsilon_{en} + \upsilon_{ei}$ and the total ion collision frequency is $\upsilon_i = \upsilon_{ie} + \upsilon_{in(resonant)} + \upsilon_{in(non-resonant)}$.

Figure 52 shows the different ratios of the collision frequencies which can be used to find their area of dominance. From panel (c) we see that ion-neutral collisions are important only at lower altitudes. At higher altitudes they can be neglected since the ion collision frequency is only dominated by the ion-electron coulomb collision. Panel (d) shows that the electron-neutral collisions are important only at the lower altitudes and can be safely neglected at higher altitudes compared with the electron-ion coulomb collision. Panel (a) plots the ratio of the electron collision to gyro frequency. Note that at all altitudes the gyro frequency dominates. Panel (b) shows the same ratio for the ions. We can see two domains here. In the low altitudes collision dominates and is called the non-inertial or the collisional. In the higher altitudes gyro frequency dominates and is called as the inertial domain.

Table 7. Electron-neutral collision frequencies.

Species	υ_{en}
$e-O$	$8.9\times10^{-11} n_O\left(1+1.57\times10^{-4} T_e\right)T_e$
$e-O_2$	$1.82\times10^{-10} n_{O_2}\left(1+3.6\times10^{-2}\sqrt{T_e}\right)\sqrt{T_e}$
$e-N_2$	$2.33\times10^{-11} n_{N_2}\left(1-1.21\times10^{-4} T_e\right)\sqrt{T_e}$

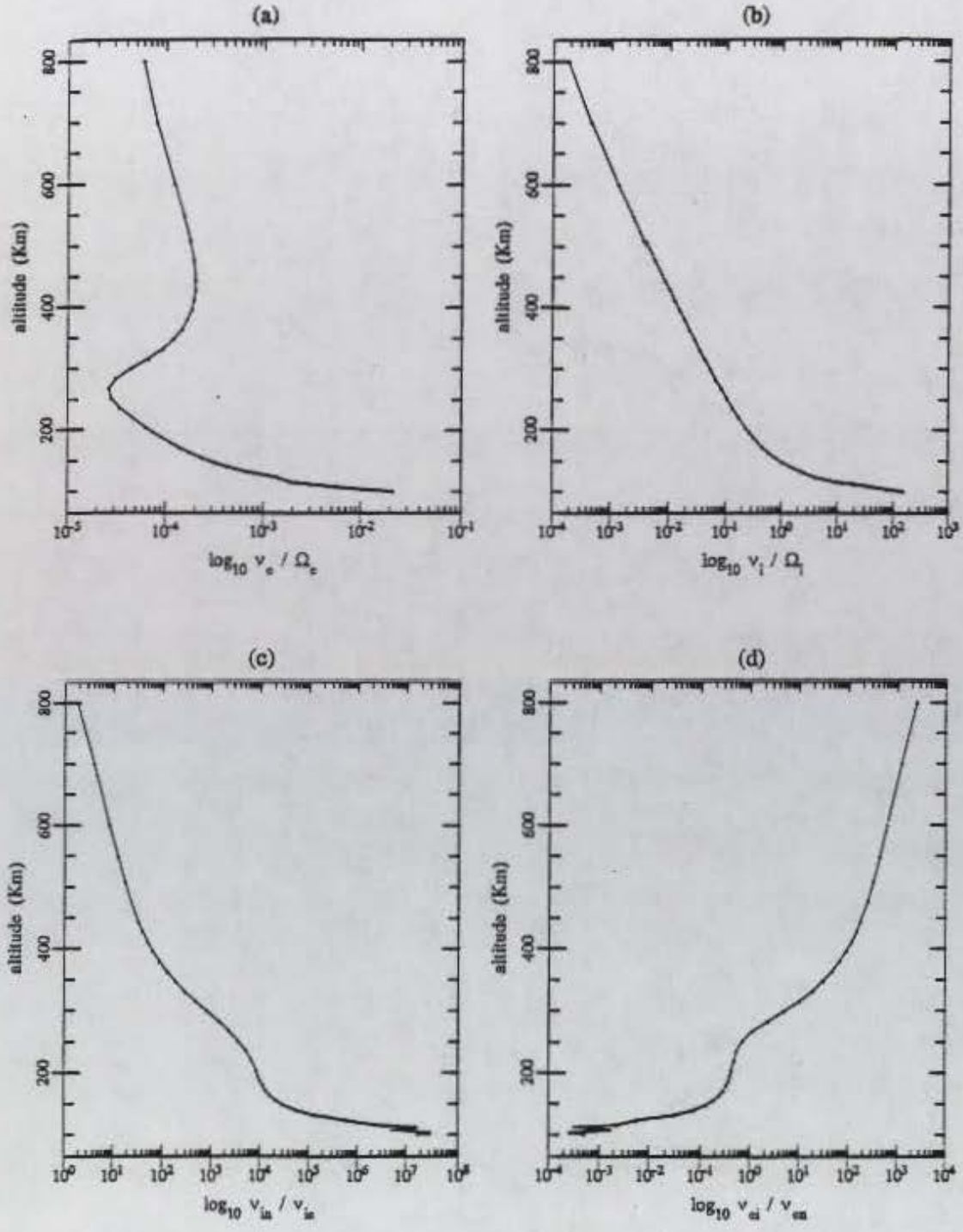

Figure 52. Altitude profiles of the ratios: (a) electron collision to gyro frequency, (b) ion collision to gyro frequency, (c) ion-neutral to ion-electron collision frequency, and (d) electron-ion to electron-neutral collision frequency.